INVESTIGATION OF TECHNIQUES FOR THE SURFACE ROUGHNESS CHARACTERISATION OF BOVINE ARTICULAR CARTILAGE

by

Siddharth Ghosh

UNIVERSITY OF BIRMINGHAM

A thesis submitted to the University of Birmingham
for the degree of
MASTER OF PHILOSOPHY

Bio-medical and Microengineering Research Centre
School of Mechanical Engineering
College of Engineering and Physical Sciences
University of Birmingham
June, 2012

ABSTRACT

This thesis investigates the surface roughness of healthy bovine humeral lateral condyle articular cartilage using a nontrivial technique of three-dimensional electron-topography with stereoscopic approach. It is a non-contact roughness characterisation with high resolution using elementary particle electron. Eucentric scanning electron microscopic (SEM) images of different magnifications (500×, 800×, 1200× and 2000×) were used for topographic reconstruction. After reconstruction, roughness has been extracted from the 3D topography. The technique was verified with a commercial standard surface of nanoscale roughness to determine its reliability by repeating with six samples. The roughness values obtained in different magnifications for six samples were compared and calibrated with atomic force microscopy (AFM). Then the method of 3D-ET was employed on four articular cartilage surfaces. The results for both the surfaces showed that surface roughness increased with magnification and thumb-rule relation has been derived. The obtained roughness values for articular cartilage range from 165 nm to 418 nm for magnification of 500× to 2000×. The cartilage samples were also calibrated with AFM and a constitutive relation between them has been derived. The thesis aims to provide a breakthrough of non-contact surface roughness analysis for mimicking articular cartilage to artificial materials for replacement therapy.

Dedicated to

My Family

ACKNOWLEDGEMENT

An engineering or scientific thesis may sound too technical, if they try to read it completely. This is the only part, probably where we talk non-technical and nice words, and they say this is the only page worth reading. I am glad; at least there are couple of pages, if anybody does not understand my thesis (which is very unlikely). Now, when I am writing this part and looking behind, I found so many people were involved starting from my preparation to join the university.

At the very first, I would like to thank whole-heartedly my supervisor, Dr. Duncan Shepherd for his patience and support throughout the project. I will be thankful to him as long as I will do research. Being supervised by him, provide me the confidence to pursue research further. I have performed lot of mistakes, which might have genuinely caused him unhappy. My poor English consistently annoyed him. When I look around, I feel finding such a supervisor is extremely rare.

I acknowledge Prof. Kyle Jiang for his precious technical facilities.

I must thank Dr. Daniel Espino, for his invaluable guidance and advices through-out, starting from very first day of specimen handling.

Dr. James Bowen, without whom a major part of my thesis would not be possible i.e Atomic Force Microscopy; his technical guidance has enlightened my research in several means. Also his different philosophies have broadened my thinking. A big bunch of thanks would be very little for him.

I also thank, Mrs. Theresa Moris and Mr. Paul Stanley for their consistent assistance with electron microscopy of Centre for Electron Microscopy.

I would like to thank Ms. Michelle Holder from the school of dentistry for x-ray micro-CT, although it is not included in the thesis due to resolution and magnification issues. Dr Joshua Rappoport from Bioscience also deserves to be thanked for his support with confocal microscopy, even though our research had taken a different direction.

Dr. Hossein Ostadi from the Biomedical and Microengineering Research Centre holds a big thank for different reasons.

Mr. Jay Naik, Dr. Majid Malboubi, Mr. Ali Mohammadakani and Mr. Hua Xin were the cool bunch of people I have ever come across. Their opinions, technical advices along with dozens of good times, made me learned and understanding. Also, I thank Dr. Aziza Mohammed and all other lab-met for their warm welcome, supports and for many fun times.

Another great friend of mine, Mr. Jian Liu meeting him is a great honor of mine. I have nettled him in days and night without keeping any barrier of time. Without him I can't even think of surviving. He was extremely a great support.

The last but not at all least, my family - which includes my fiancée (an intelligent researcher in profession), my grand-parents (Bapidadu and Dida),

Masi (aunt), my mother, my father and my little brother without them this mission would not have accomplished. Their sacrifices, tolerance and patience for me are indescribable.

I owe a massive apology, if I miss anybody in particular. I thank to all whoever was involved with this project with as little contribution as it is.

Siddharth Ghosh
University of Birmingham
June, 2012

LIST OF ACRONYMS

2D	Two-dimensions(-al)
3D	Three-dimensions(-al)
3D-ET	Three-dimensional electron-topography
AFM	Atomic force Microscope
BHLC	Bovine humeral lateral condyle
BHLC-$1_{500\times}$	Sample BHLC -1 scanned at 500× with SEM
BHLC -$2_{800\times}$	Sample BHLC -2 scanned at 800× with SEM
BHLC -$3_{1200\times}$	Sample BHLC -3 scanned at 1200× with SEM
BHLC -$4_{2000\times}$	Sample BHLC -4 scanned at 2000× with SEM
e-beam	Electron beam
ESEM	Environmental Scanning Electron Microscope
ET	Electron-topography
FEG	Field Emission Gun
g	Gram
keV	Kilo electron Volts
μm	Micrometer
M	Molar
mbar	Millibar
mg	Milligram
ml	Milliliter
nm	Nanometer
PDMS	Polydimethylsiloxane
PDMS-$1_{500\times}$	Sample PDMS-1 scanned at 500× with SEM
PDMS-$2_{800\times}$	Sample PDMS-2 scanned at 800× with SEM
PDMS-$3_{1200\times}$	Sample PDMS-3 scanned at 1200× with SEM
PDMS-$4_{2000\times}$	Sample PDMS-4 scanned at 2000× with SEM
pH	Measure of acidity or basicity
PM-AFM	Phase-modulation AFM
SEM	Scanning Electron Microscopy
Q-Q plot	Quantile-quantile plot

NOTATION

A	Base
A^-	Conjugate base anion
$AFM\ R_{am}$	Mean set of Ra obtained from AFM
c	Intercept at y axis
d	Distance of between I_l and I_r
$ESEM\ R_{am}$	Mean set of Ra obtained from 3D electron topography
F	Acting force on a cantilever
F_l	Focal point left
F_r	Focal point right
H	Hydrogen
H^+	Hydrogen ion
I_β	Eucentric image at angle β
I_θ	Eucentric image at angle θ
I_l	Left images
I_r	Right images
k	Stiffness - a geometric dependent parameter
K_a	Chemical equilibrium constant
l	Focal length
L	Evaluating scan length
m	Slope of a curve
M	Lumped effective mass
o	Point of interest for reconstruction
p	Statistical significance
P	Centre of the circle
r	Radius of circle for eucentricity
R_a	Mean profile roughness
R_{am}	Mean of set of R_a of a constant magnification factor
R_{aM}	Mean of Ra of BHLC-1 - 4
$R_{aM'}$	Mean of Ra of BHLC-2 - 4
R^2	Coefficient of determinants or Goodness of curve fitting
S	Scene Geometric parameter
S_a	Mean of total surface roughness constant magnification factor
S_{aM}	Mean of Sa of BHLC-1 - 4
$S_{aM'}$	Mean of Ra of BHLC-2 - 4.

S_{dev}	Standard deviation
Δx	Displacement due to force F
x	Horizontal x axis
x_l	Disparity functions at left
x_r	Disparity function at right
X_l	Left epipolar line
X_r	Right epipolar line
y	Horizontal y axis
z	Vertical z axis
Z_p	Depth of pixels
^0C	Degree centigrade
×	Magnification factor
θ	Eucentric angle for disparity
ω_0	Resonance frequency

CONTENTS

LIST OF ILLUSTRATIONS

Chapter II Background

Chapter III Materials and Methods

Chapter IV Results

Chapter V Discussions

Appendix

LIST OF TABLES

Chapter IV Discussion

CHAPTER I

INTRODUCTION

In this thesis, I have characterized humeral lateral condyle articular cartilage of *Bovine sp.* on the context of nanoscale surface roughness with a novel technique of three-dimensional electron topography (3D-ET).

Articular cartilage is medically and mechanically a very significant biomaterial. It behaves as an extremely low friction coefficient material for articulation of healthy joints [*Park et al., 2004*]. In cases of chronic arthritic conditions, joint replacement therapy remains the final solution. However, there is much interest in developing tissue engineered cartilage [*Chen et al., 2006; Temenoff et al., 2000; Bohari, 2011*] and new synthetic materials [*Ateshian, 2007; Shepherd et al., 2008; Pylios et al., 2008; Shepherd, 2010*] for joint replacement that have the characteristics of articular cartilage. Therefore, a detailed understanding of the surface roughness of cartilage is important. Current contact roughness characterisation techniques always produce micro/nanoscale

deformation due to the acting force of the probe [*Poon et al., 1995; Xu et al., 2009; Ukraintsev et al., 2012; Canale et al., 2011*] on low modulus materials, such as articular cartilage.

This thesis investigates articular cartilage with a non-frequently used non-contact technique of surface roughness characterisation with three-dimensional reconstruction of electron imaging. The technique utilized here is based on stereoscopic three-dimensional reconstruction which is mainly used on the macroscale [*Hisakazu et al., 1999; Sebastian et al., 2008*]. When three dimensions are available, computing roughness or depth information becomes a routine practice. Since, this method has not been tested and verified earlier at nanoscale, the performance has been compared with different means. A standard nano-roughness sample has been used and the roughness values obtained from three-dimensional electron topography were compared with Atomic Force Microscopy (PM-AFM).

The overall aim of this thesis was to investigate surface roughness of articular cartilage using a non-contact method of three-dimensional reconstruction of electron imaging. The overall aim was achieved by the following objectives:

- roughness measurement of a standard sample using 3D electron-topography (3D-ET) for reliability testing,
- roughness measurements have been verified and calibrated with PM-AFM,
- 3D-ET has been implemented on articular cartilage surface, along with a calibration with PM-AFM
- and finally, analysis of roughness with respect to magnification factor.

The rest of the thesis is divided into a further four chapters. **Chapter II** acts as the foundation of this thesis and presents the necessary background information. The basic details of articular cartilage have been provided in the form of a brief introduction to its inherent properties. Theoretical aspects of surface roughness

and different techniques to characterize it are also discussed. Then, I talk about the theory of stereoscopy - the method of three-dimensional reconstruction. Finally, the working principles of the two instruments - electron microscope and atomic force microscope are detailed.

Chapter III focuses on the materials and methods that have been used. Information like sources, geometry and preparation of the standard surface and articular cartilage are discussed here. The method section provides knowledge of the experiments and data analysis. Here, I discuss about characterising standard surface at first to have verification of roughness characterisation with three-dimensional electron topography. Then, we move into atomic force microscopy to calibrate our technique. Ultimately, the method of three-dimensional stereoscopic roughness characterisation is employed on articular cartilage.

Chapter IV holds the results of roughness characterisation and analysis on them. Here, we will observe the relation between magnification and roughness. The calibration of roughness with phase modulation atomic force microscopy to three-dimensional electron-topography is obtained for the surfaces.

In **Chapter V** I discuss all the results and analyse them to arrive to some conclusions. The advantages and disadvantages along with a theoretical thumb-rule for calibration have been derived here.

CHAPTER II
BACKGROUND

2.1. INTRODUCTION

This chapter presents the fundamental scientific knowledge necessary to understand the thesis. The basic structural and physiological state of articular cartilage and its novel properties, unlike other tissues, are discussed here (section 2.2). We will move on to the theory of roughness (section 2.3) and stereoscopic three-dimensional reconstruction (section 2.4 and 2.5), finally ending with the theories of electron imaging (section 2.6) and atomic force microscopy (section 2.7).

2.2. ARTICULAR CARTILAGE

Articular cartilage is a connective soft-tissue, which is found in moving skeletal joints of vertebrates. The basic structural elements of it are collagen fibers, glycosaminoglycan and chondrocyte cells *[Stockwell, 1979].* It typically contains 60 to 70% of water [*Maroudas, 1979].* It has three different cross-sectional layers. After the

bone, articular cartilage starts with the calcified zone. Then, the deep zones where collagen fibers are vertically aligned along with the dense presence of condrocyte cells (pink colour circles in figure 2.1). Finally, there is the superficial layer - where collagen fibers are oriented tangentially; this thin layer is the outer most and is covered with synovial fluid *[Temenoff, 2000; Huber, 2000].*

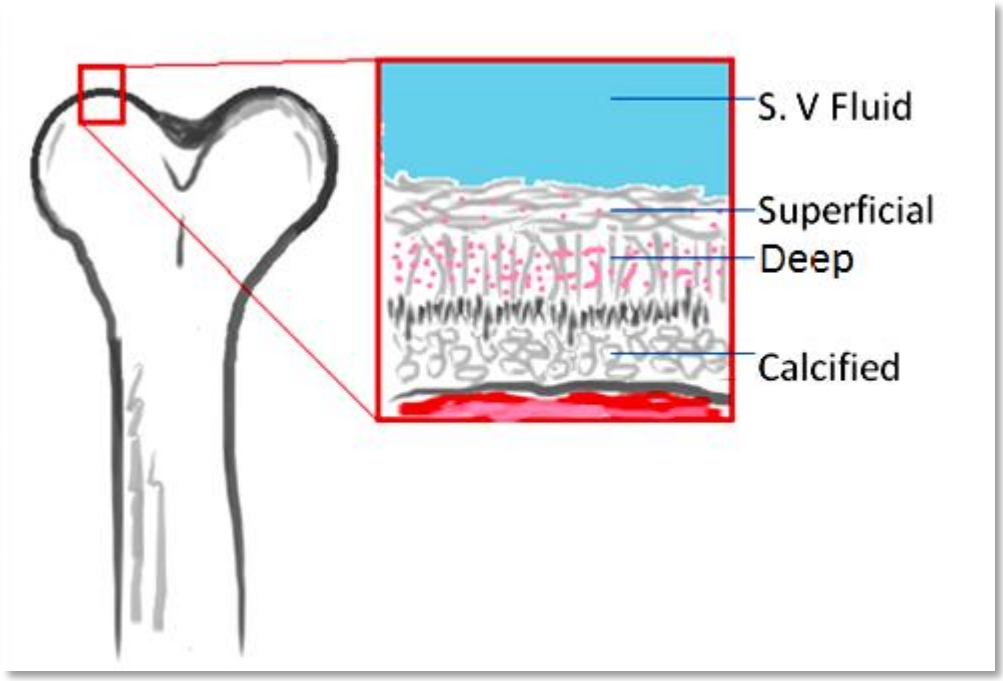

Figure 2.1. Cross-sectional view of articular cartilage internal structure.

The optimal biomechanical properties of articular cartilage enable it to withstand large compressive, tensile and shear loads [*Shepherd et al., 1997; Mow, 1984; Swann, 1991; T. Räsänen, 1996; Radin et al., 1970; Shepherd et al., 1999; Schmidt, 1990; Setton et al., 1995; Persons et al., 1977]*. Articular cartilage does not contain blood vessels and neurons. Absence of them, support it to act as *'an ideal cushioning material'* [*Stockwell, 1979*], since it can damp out whole body load and sudden impact of external load from bone ends below a critical load [*Maroudas et al., 1986; Mow et al., 1997*].

The hydrated collagen network consists of negatively charged proteoglycans which generate high internal pressure. This internal pressure increases the bulk volume of articular cartilage [*Maroudas et al., 1981; Urban et al., 1979*]. The synovial

fluid acts as a non-Newtonian lubricant between two articular cartilage surfaces [*Stockwell, 1979; Bloch et al., 1963*]. Low static and kinetic coefficients of friction make it a unique connective soft-tissue for articulation between two bones, which helps to inhibit wear. Earlier studies have confirmed that the kinetic coefficient of friction of articular cartilage is around 1×10^{-3} to 3×10^{-3} [*Mark et al., 2007; Park et al., 2004*]. But, the biophysical hypothesis of acting as a low friction coefficient material is not yet explored in great deal. Studies have reported that the internal structure of articular cartilage acts with several different modes of lubrication like weeping, squeeze film, etc. [*Dowson et al., 1966; Schmidt, et al., 2007; Gleghorn et al., 2008*]. The surface roughness of articular cartilage plays a crucial role in friction and lubrication of joints.

Contact surface roughness characterization of articular cartilage with AFM have reported roughness values of around 450±237 nm [*Moa-Anderson et al., 2003*] and noncontact techniques like optical coherence tomography and ultrasound imaging have provided values of around 8000 nm and 9000 nm, respectively [*Saarakkala et al., 2009; Saarakkala et al., 2004*]. An attempt with laser profilometer has determined roughness values of around 800±200 nm [*Forster, 1999*]. These roughness ranges are difficult to conceive when we look at the friction coefficient. So, in the thesis I have primarily characterised articular cartilage surface on the context of roughness at nanoscale, beside investigations on qualitative surface morphology.

2.3. SURFACE ROUGHNESS

Roughness is one of the most important surface topographic characterisations, which intuitively refers to the unevenness or irregularity of a texture. It gives an idea of how smooth the surface is at a certain length scale. Roughness is dependent on the vertical and horizontal resolution of the measuring instruments [*Selvaduray, 2002*]. It is also a function of working length scale. Beside this, statistical implications such as sample size (statistical power to select the number of observances) and intervals

affect the roughness. Due to these statistical implications, roughness is quantified as an average roughness or arithmetic mean of vertical distances which is a function of the x axis. For a two dimensional profile it is represented as R_a and for three-dimensional profile as S_a. Figure 2.2 shows the quantification of R_a for roughness of a single two dimensional line.

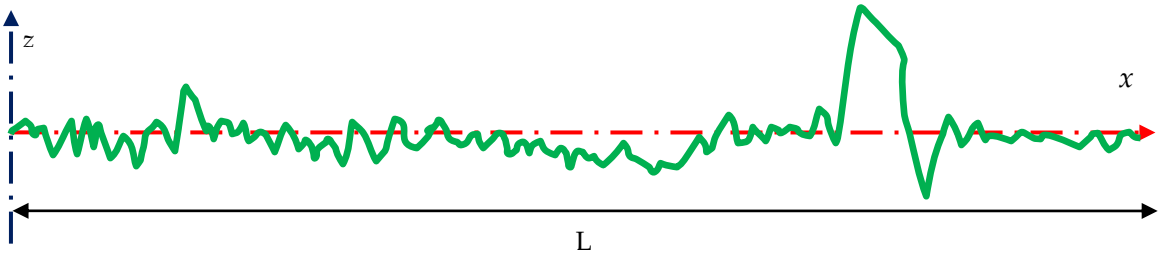

Figure 2.2. Two dimensional profile texture of a surface.

The surface roughness can be calculated from:

$$R_a = \frac{1}{L}\int_0^L |z(\sigma)d\sigma| \qquad Eqn.\ 2.1$$

$$S_a = \frac{1}{A}\int_0^A |z(\sigma,\tau)|d\sigma d\tau \qquad Eqn\ 2.2$$

where, L and A are the evaluating scan length and scan area, respectively, z is the vertical distance on the z axis, σ and τ are the distances along x and y axis, respectively. It is always advised to quantify the standard deviation since it depends on sampling numbers. Due to statistical implications, sometimes the root mean square of surface roughness also comes into consideration [*Selvaduray, 2002*].

Typically, roughness is quantified using a contact technique such as stylus instruments, scanning tunneling microscopy, atomic force microscopy and profilometer. Accuracy of probing can go up to a few nanometers (with a 1 - 2 nm probe diameter) with the atomic force microscopy technique [*Yao et al., 2005; Park*

Scientific, 1997]. But, the problem of any contact technique lies on the probing which ultimately contributes a dilation effect [*Poon et al., 1995; Xu et al., 2009; Binning et al., 1986*] depending on the shape of the probe, as shown in figure 2.3.

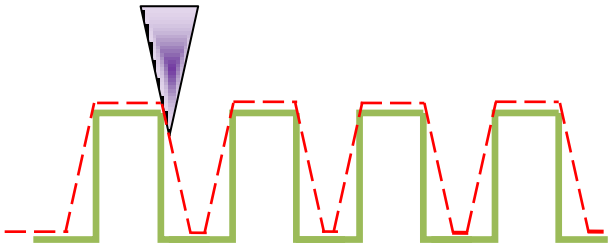

Figure 2.3. Dilation effect due to the conical shape of the probe in contact surface characterisation.

To avoid the dilation effect, a non-contact method like optical ellipsometry came into the picture, but the resolution is highly dependent on the spot size of two optical beams, which are limited on the wavelength of visible light (380 - 740 nm). So, I have tried to utilise an electron beam where the wavelength can be varied with the accelerating voltage which ultimately varies its energy. With electron beam imaging resolution can also be limited by the spacing of the raster scans points. Also energy cannot be infinitely increasing since it will burn the sample.

2.4. Electron Diffraction

The wavelength of negatively charged elementary particle electrons can easily be defined with Plank-Einstein's energy equation [*Einstein, 1906; Przibram, 1967*] (Eqn. 2.3):

$$E = h\nu \qquad Eqn.\,2.3$$

Einstein found that energy E is proportional to frequency ν for any electromagnetic wave, and Plank's proportionality constant (h) ultimately defines the relation [*Einstein, 1906*]. As we know, frequency is inverse of wavelength λ, taking that into account wavelength turns out to be inversely proportional to energy (Eqn. 2.4):

$$\lambda = \frac{h}{E} \qquad Eqn.\,2.4$$

For electron diffraction and for a relativistic approach de Broglie replaced the E with relativistic momentum $\bar{p}$ of electron [*Broglie, 1923*].

$$\lambda = \frac{h}{\bar{p}} \qquad Eqn.\,2.5$$

Now, if an electron with mass m_0 accelerates with electric potential U and elementary charge e, wavelength can be defined to sought velocity v [*Broglie, 1923; Feynman et al., 1964; Vazirani, 2003*]:

$$\lambda = \frac{h}{m_0 v} = \frac{h}{\sqrt{2m_0 eU}} \qquad Eqn.\,2.6$$

So, the wavelength of an electron is not limited unlike a photon. It depends on the electric potential; the higher the electric potential, the lower the wavelength. And the lower the wavelength, the higher the imaging resolution. Practically, in electron microscopy, the wavelength of an electron is in terms of few picometers [*Bendersky et al., 2001*], when it is approaching 70% of the speed of light. Utilising, this elementary particle for surface roughness characterisation not only gives high resolution but also provides a non-contact approach. I have utilised the electron beam to compute depth imaging using the stereoscopic approach and ultimately from it extracted the surface roughness.

2.5. SCANNING ELECTRON MICROSCOPY

Scanning electron microscopy (SEM) is used generally, to image high resolution microscopy down to the nanometer scale. The typical imaging is done with secondary electron detection. In an SEM, accelerated electrons are emitted from a Schottky electron gun (the common gun is of tungsten which is thermionic) and the best available one is a field emission gun or FEG. The electron beam is focused with two magnetic scanning coils and pairs of deflectors inside the column. It scans

in the x and y axes to produce a raster image. This deflection of the beam is controlled by the final deflector. These electrons carry significant amounts of kinetic energy. The electron beam generally has energy of 0.2 keV to 40 keV. When the electron encounters a solid surface it decelerates and produces different signals with secondary electrons, backscattered electrons, diffracted backscattered electrons, X-rays, photons and heat [*Goldstein et al., 2003*] (figure 2.4).

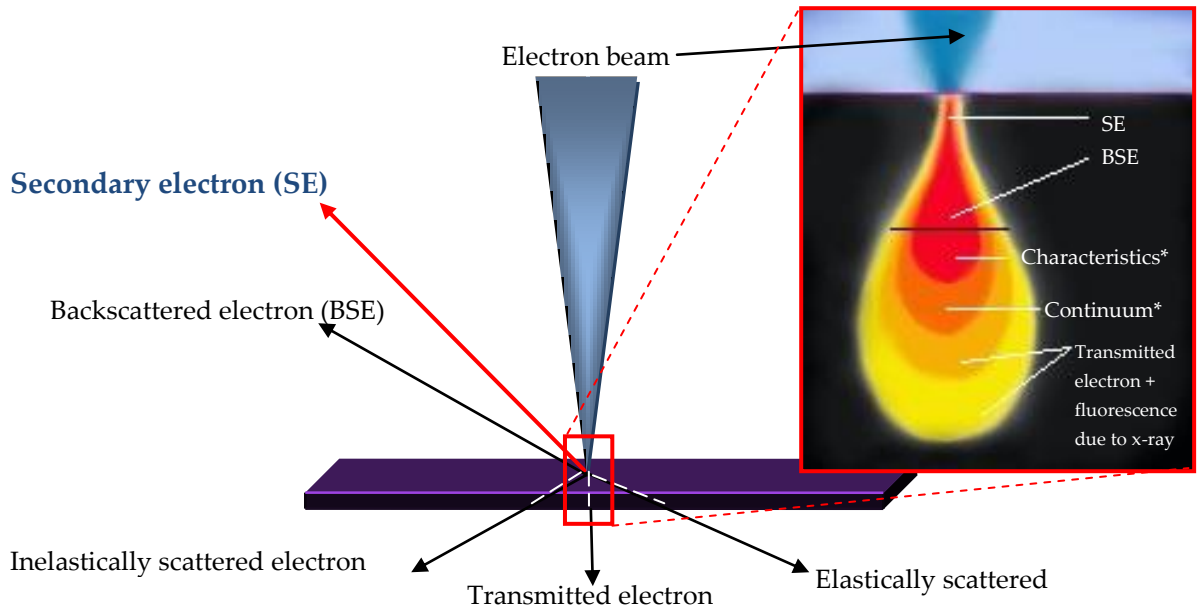

Figure 2.4. Electron-sample interaction resulting with possible types of signals used for imaging. The tear drop schematic shows the sources of different kind of electrons and x-ray [* denotes x-ray].

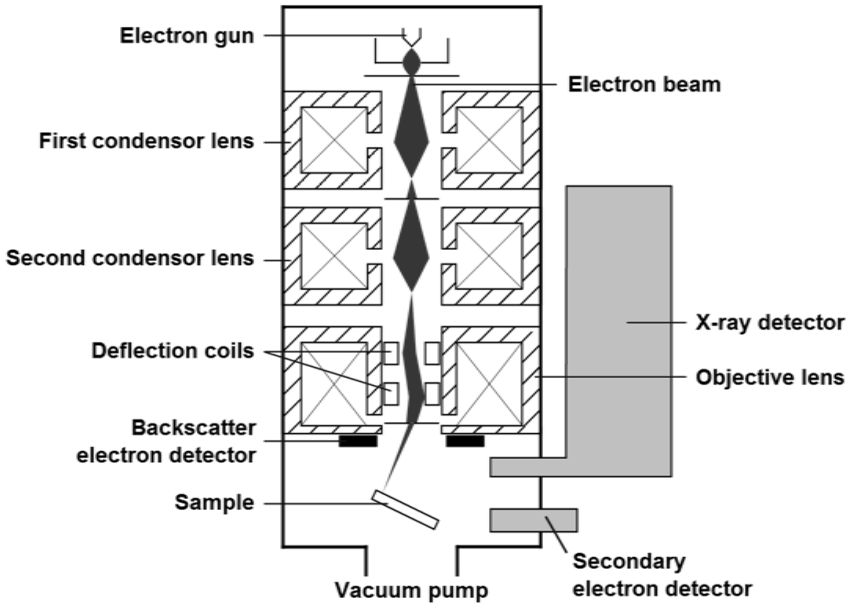

Figure 2.5. Schematic of a scanning electron microscopy [image source: http://en.wikipedia.org/wiki/File:Schema_MEB_(en).svg].

The most frequently used and useful signal are the secondary electrons. The secondary electron detector, or commonly known as SE detectors, are the primary detector of an SEM system, which provides the surface morphology and depth information. To get good intensity of secondary electrons, the working distance should always be less for high resolution imaging. Figure 2.5 shows a schematic diagram of SEM.

2.6. STEREOSCOPIC 3D RECONSTRUCTION

Roughness can be quantified only if the height information or the depth information is available ($z(\sigma)$ in eqn. 2.1). Imaging a constant area from different angles provides a differential height distribution. Stereoscopic image processing is one of the approaches used to determine height distribution. It is very well accepted and well practiced technique of three-dimensional reconstruction.

The stereoscopic approach was inspired by human eyes which have inherent properties of binocular vision. Binocular vision creates a cyclopean image of three-dimensional perception (figure 2.6-B) from two dimensional images [*Julesz, 1971; Ramachandran, 1988*]. The algorithm of stereopsis is to construct a depth image by merging two two-dimensional images captured from slightly different angles [*Marr et al., 1979*]. This angular position is known as the eucentric position, similar to our eyes' position. In eucentric images equal distances from an object is maintained for more than one image capture (figure 2.6-A).

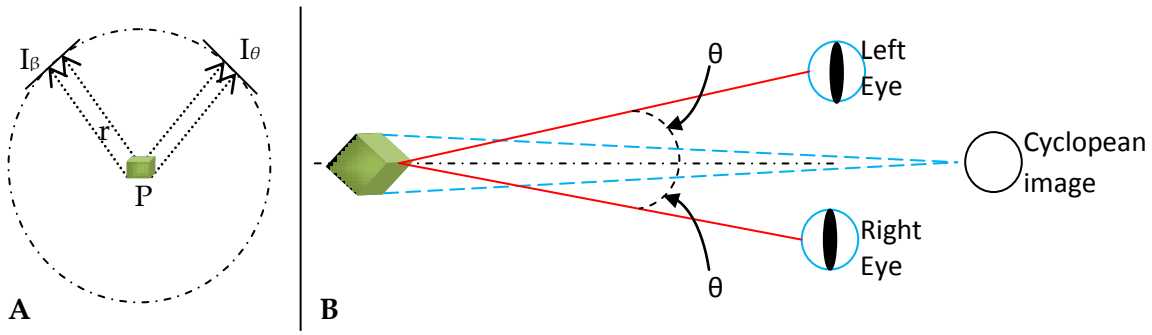

Figure 2.6. (A) Eucentric imaging and (B) cyclopean image reconstruction – principle of stereoscopy.

Given a three-dimensional surface, the algorithm of stereoscopy solves the *corresponding-problem* and *disparity-problem* to reproduce the topography back by capturing N numbers of 2D eucentric images [*Belhumeur, 1992*]. The corresponding-problem is to determine a set of matched locations among those 2D images. It is done by matching pixels of a single 2D image which correspond to the same set of locations in other 2D images. Now, the issues are, how to select these set of locations? There are two approaches: correlation-based and feature-based. In the correlation based approach, the location is chosen by matching intensities and in the feature based approach, it is done by matching sparse sets of image features. Correlation-based matching is problematic since it is based on intensities and with variation of angle intensities of the same location always change. But in the feature-based approach, this problem is an unlikely event since it uses edge-filters to detect edges and matches segments, angles and lines of similar features. It also searches for similarity of geometries [see appendix F].

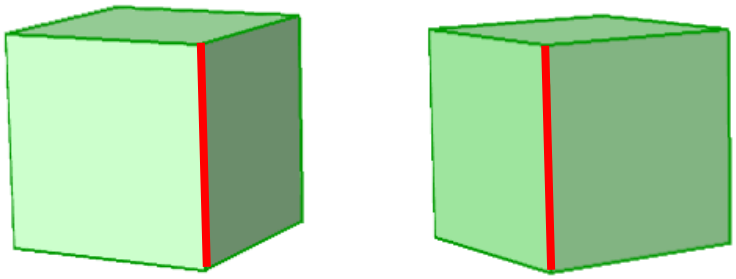

Figure 2.7. Left and right eye view of single object, showing the disparity property of stereopsis. [Figure is exaggerated for better understanding]

The matched location depth, which is a function of its horizontal displacement ($z(\sigma)$), is computed; this is known as disparity between two images. The horizontal displacement is the difference of distances for a constant point which corresponds to a single position, resulting due to capture from different angular positions. In real time with binocular vision, observing a single object with only the left eye and again observing the same with only right eye, gives the concept of

horizontal displacement (figure 2.7). In digital image processing it is the difference in the coordinates of pixels that corresponds to a single point of stereo images.

The major computational problem of this construction involves: *noise* (experimental error like imperfect capturing, lighting variation, disorientation, etc.), *indistinct image features* (high luminescence effectively makes a surface featureless), *salient three-dimensional features* (discontinuity of a surface ('breaks'), depth ('creases') along with steep sloping) and *half occlusion* (depth estimation becomes a difficult job) [*Belhumeur, 1996*]. But these problems were earlier rectified in several modified algorithms.

The Bayseian approach of computer graphic reconstruction is a mature field, but in general a modified Bayeseian framework is used for a computational model of stereopsis [*Belhumeur, 1996*]. In a Bayeseian framework one always infers scene geometry S (a feature-based corresponding problem) for given left images (I_l) and right images (I_r) by considering $P(S|\ I_l, I_r)$. Given the measurement, a probability distribution known as *posterior probability,* is described by Eqn. 2.7.

$$P(S|\ I_l, I_r) = \frac{P\ (I_l, I_r|\ S)\ P(S)}{P(I_l, I_r)} \qquad Eqn.\ 2.7$$

The term $P\ (I_l, I_r|\ S)$ in Bayes' theorem† is referred to as the image formation *or likelihood model* [*Belhumeur, 1996; Bayes, 1963*]. It infers the goodness of geometric matching among the captured images and $P(S)$ is referred to as the *prior distribution model* or initial degree of belief [*Bayes, 1963*]. It measures the probability of a specific geometry S (before the images are captured).

†Bayesian statistical method depends on a 'prior' probability distribution, from where a 'posterior' conditional distribution can be derived. It is an approach to address epistemological uncertainly with probability. It states that a subjective degree of belief rationally changes with the account of evidence. Like, the 'four candles' problem, where a person hears either 'four candles' instead of 'fork handles' [*Spiegelhalter et al., 2009; Stones, 2012*].

$$P(hypotheis|data) = P(data|hypothesis)P(hypothesis)/P(data)$$

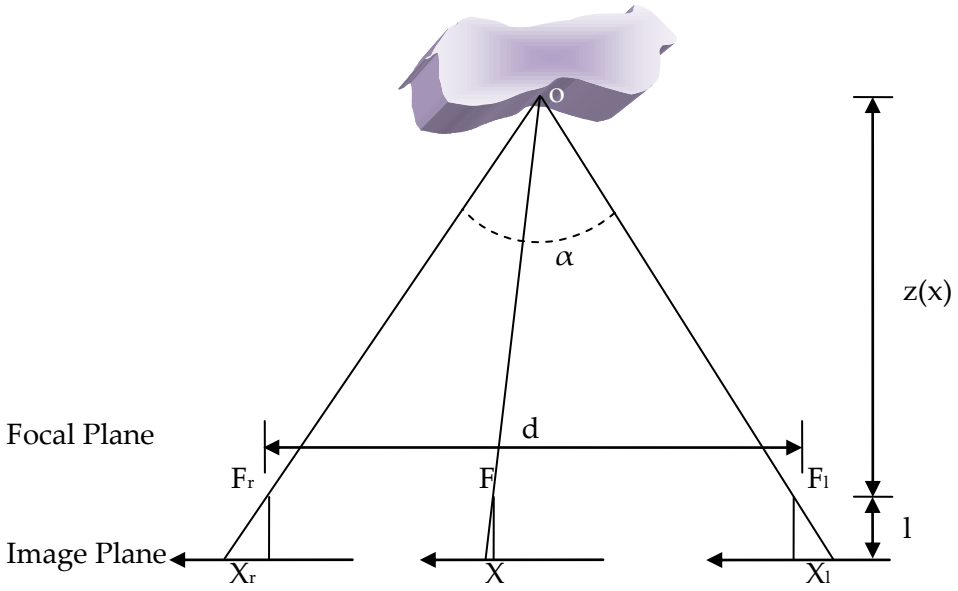

Figure 2.8. F_r, F and F_l are focal points and X_r, X and X_l are epipolar lines. α is the lateral angle. Here, the disparity and distance functions are defined with respect to cyclopean image plane [*Belhumeur, 1996].*

Let, two lenses be positioned at a certain distance *d* from each other and their focal points F_l and F_r are situated at the same plane with focal length l and another virtual cyclopean lens is placed with focal point F (figure 2.8). The primary constraint is that the image plane base is parallel to the focal plane. Now, *o* is the point which is mapped through all three lenses. The lateral angle between this lens with respect to o is α. X_l, X_r and X are epipolar lines for image planes with coordinates $x_l \epsilon X_l$, $x_r \epsilon X_r$ and $x \epsilon X$, respectively. At cyclopean lens if the point *o* is visible from all three lenses, then $x = (x_l + x_r)/2$. A disparity function differential of the left and right view are $x_l = x + d(x)$and $x_r = x - d(x)$. So, the disparity function can be defined as

$$d(x) = \frac{x_l - x_r}{2} \qquad Eqn.\,2.8$$

$$d(x) = \frac{l\,d}{2\,z(x)} \qquad Eqn.\,2.9$$

and the depth of pixels are quantified as

$$Z = \frac{x_l - x_r \cos\alpha}{\sin\alpha} \qquad Eqn.\,2.10$$

2.7. Atomic Force Microscopy

Atomic Force Microscopy (AFM) is a technique to analyse surface topography to determine parameters like surface roughness, stiffness and force mapping. The general principle is based on scanning probe microscopy. The fundamental concept of this instrument lies on surface tunneling microscopy [*Bining et al, 1986*]. The basic element of imaging is a micro cantilever with nanometer range tip. The tips are generally made from silicon sometimes silicon nitride to enhance the stiffness. It works according to Hooke's law ($F= k.\Delta x$, where F is the applied force, k is the stiffness of the cantilever and Δx is displacement), recording the displacement or the deflection of the tip with a quadrant photodiode utilising a laser beam deflection (figure 2.9).

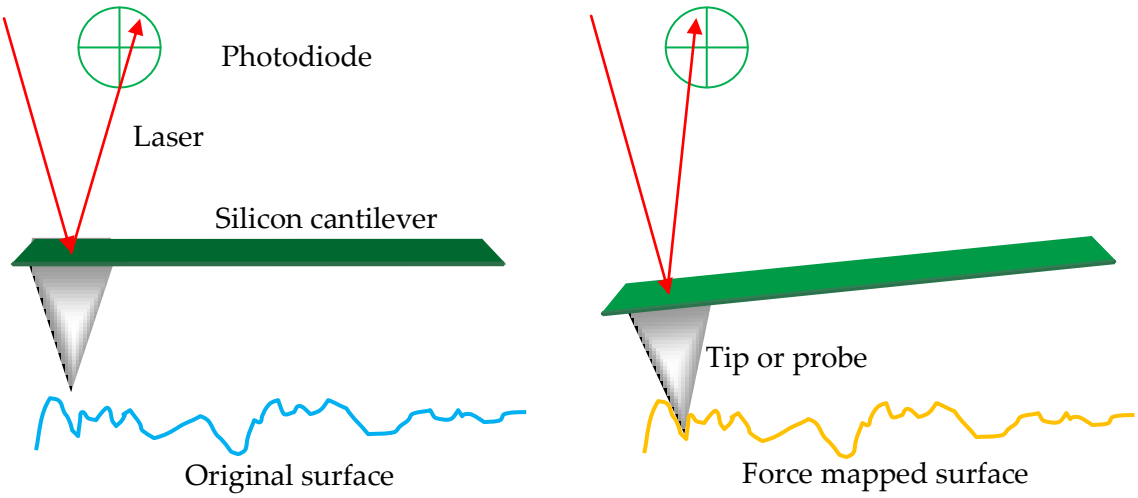

Figure 2.9. Graphical representation of atomic force microscopy principle.

AFM ultimately maps the force topography of the surface. The problem of this method is that due to the applied force the surface can deform [*Canale et al., 2011; Ukraintsev et al., 2012*]. Figure 2.10 shows modeling two domains with two springs. Since two surfaces are in contact, so the stiffness of each will act in series. If one spring is more compliant than the other, then there will be more displacement of the same towards force acting direction (Δx and Δz). Another frequent problem is the stick-slip phenomenon. When two surfaces slide on each other sometimes jerking

occurs. This is because two contact surfaces stick together when the sliding force is less than the static friction. And when the static friction is overcome, they slip. This continuous process is called stick-slip. This kind of jerking profile is often visible under AFM [*Mate et al., 1987; Lantz et al., 1997; Medyanik et al., 2006*].

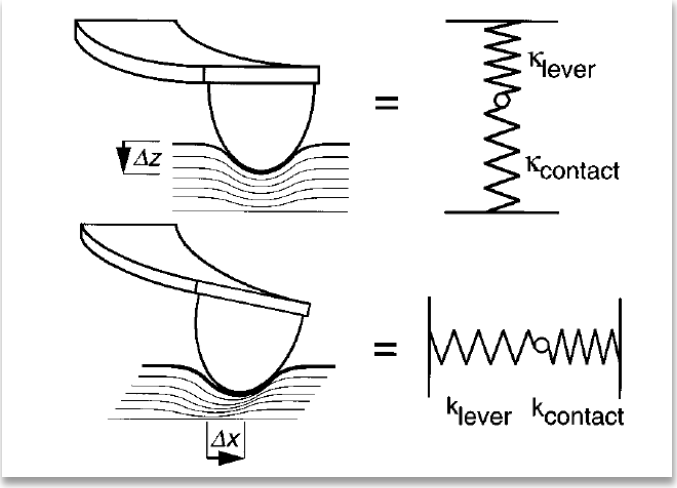

Figure 2.10. Lateral and normal displacement of probe. [*Caprick et al., 1997*, consent taken from the author - Prof. Robert Caprick, University of Pennsylvania, Philadelphia, USA]

To avoid these problems, tapping mode imaging is used to provide better results [*Zhong et al., 1993; Hansma et al., 1994*]. Phase modulation is an extension of tapping mode where more information can be achieved compare to simple tapping mode [*Fukuma, 2006*]. In phase-modulation, the cantilever always fluctuates near its resonance frequency ($f_0 = \sqrt{k/m}\ /2\pi$ where, k is stiffness of the cantilever and m is lumped effective mass). This oscillation is generally provided with a piezo-actuator. The imaging is done by sensing the phase shift due to the interaction force. The motion of the cantilever can be described by Eqn. 2.11 [*Fukuma, 2006*].

$$\frac{d^2\check{z}}{dt^2} + \frac{\omega d\check{z}}{Q\ dt} + \omega^2\check{z} = \omega^2 A_{exc}\cos(\omega t) + \frac{\omega^2}{k}F_{ts} \qquad Eqn.\ 2.11$$

where, ω, $\check{z}$, t, Q, A_{exc} and F_{ts} are the rate of change of angular displacement ($2\pi f_0$), vertical probe position (at harmonic oscillation $\check{z} = A\sin(\omega t + \Delta\varphi)$; $\Delta\varphi$ is phase shift), time, quality factor, fixed amplitude and interaction force, respectively.

CHAPTER III
MATERIALS AND METHODS

3.1 INTRODUCTION

This chapter will present the materials and methods used in the surface characterization of articular cartilage. The cartilage was characterised using two techniques: scanning electron microscopy and atomic force microscopy. Before the cartilage was investigated, a standard sample was used to verify and validate the techniques proposed for cartilage. Figure 3.1 gives a brief overview of the process flow of surface roughness characterisation. Figure 3.2 provides a detailed process flow of the same.

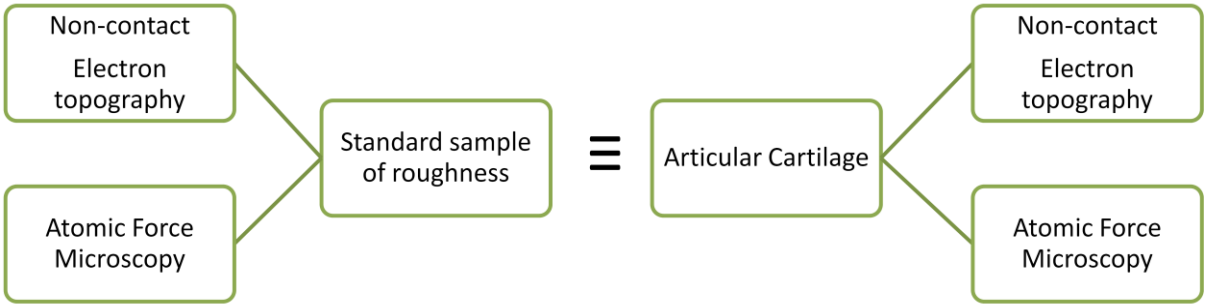

Figure 3.1. The road-map of the quantitative analysis of surface roughness characterization.

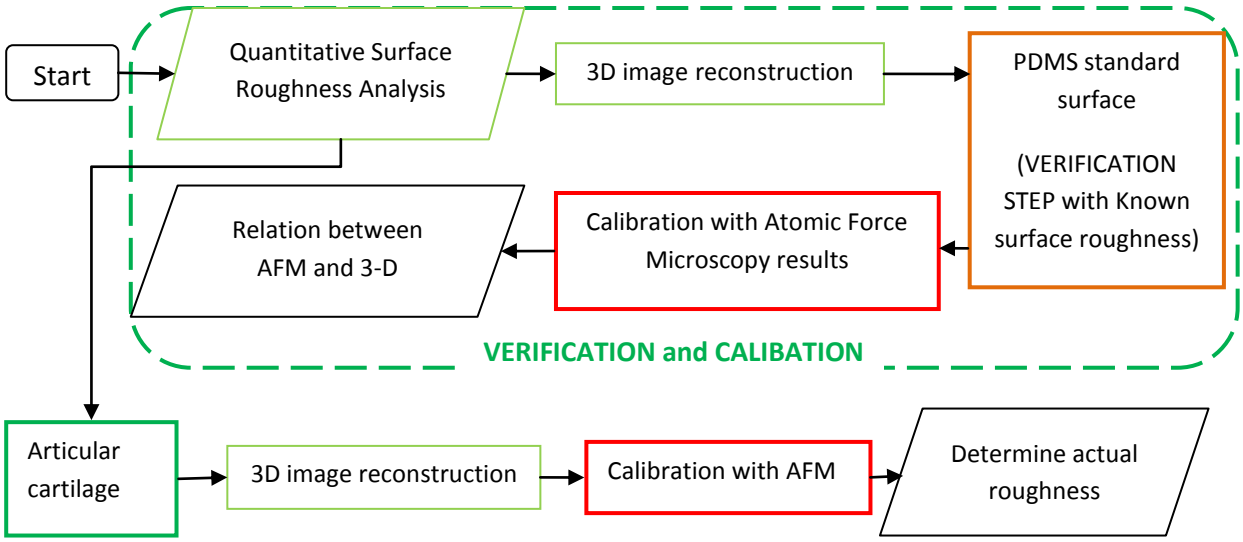

Figure 3.2. The process flow of quantitative analysis - surface roughness characterization and calibration of electron topography.

3.2. STANDARD SAMPLE PREPARATION

A standard surface roughness sample was purchased from Rubert and Company Ltd., Manchester, UK. The sample is known as a *sinusoidal reference - specimen 543-X,* as shown in figure 3.3. The datasheet from the company is shown in appendix A. According to the datasheet, the surface was made from electroformed nickel and other specifications were as follows;

I. the surface morphology was sinusoidal,

II. measurement equipment used was Talystep Mk 1; TSetp #4; Stylus tip 700 nm,

III. the average profile roughness (± standard deviation), Ra = 35.48 ± 1.2 nm.

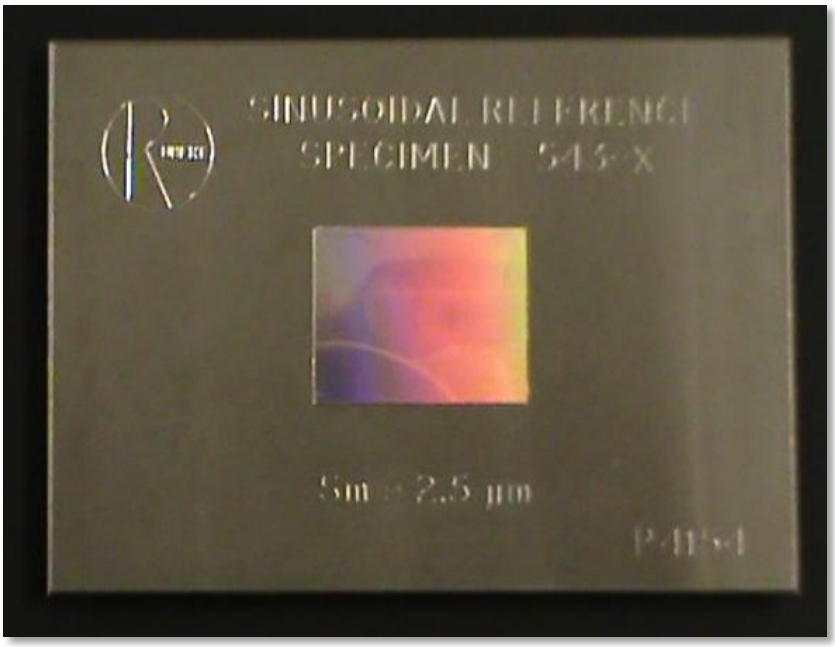

Figure 3.3. The electroformed nickel standard roughness sample holding a mean profile roughness of 35.48 nm (rainbow effect zone).

The total size of the standard nickel surface was 60 mm × 45 mm. The size of the whole metallic surface was large enough to cause spontaneous degassing inside the vacuum chamber of the SEM. So, the nickel surface was replicated onto polydimethylsiloxane (PDMS) and cut into small pieces to avoid the degassing problem. Figure 3.4 provides the process flow of the soft-lithography process of the nickel surface with PDMS. The PDMS was prepared with 10:1 w/v of Sylgard 184 Silicone elastomer and its curing agent (manufactured by Dow Corning Corporation, Midland, USA), followed by rigorous mixing of them in a teflon beaker using a spatula. The mixture was degassed by keeping the viscous fluid in open air under atmospheric pressure for 20 minutes. After that the liquid PDMS was poured onto nickel surface. It was then allowed to cure overnight, which produces a transparent and solid peelable material at room temperature. Since PDMS is a non-conductor, for SEM the surface was sputter coated with ~10 nm of platinum (figure 3.8.B) (see Appendix E for a description of the sputter system).

Figure 3.5 shows one of the samples prepared for SEM. Six samples of the PDMS were prepared for SEM.

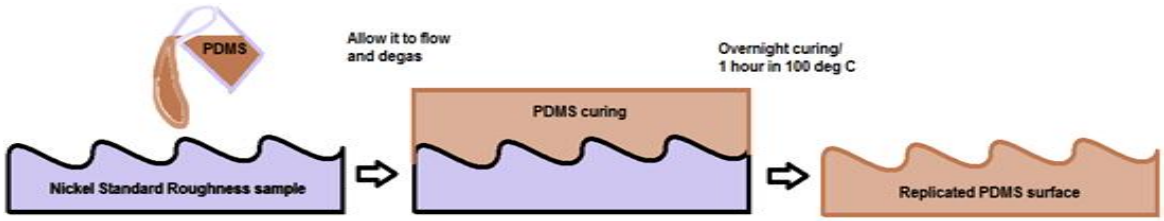

Figure 3.4. Softlithography of standard nickel surface with PDMS (cured overnight).

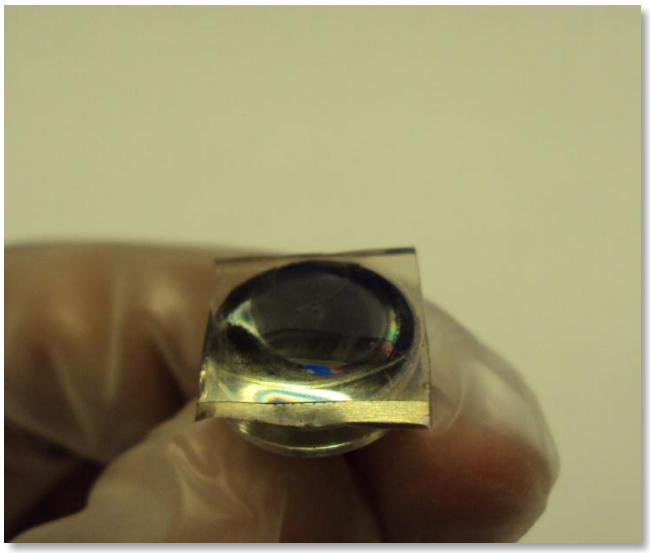

Figure 3.5. The PDMS replicated surface of standard nickel surface, showing the rainbow effect similar to the original surface, shown in figure 3.3.

3.3. ARTICULAR CARTILAGE PREPARATION

Articular cartilage was obtained from the bovine lateral humeral condyle. The specimens of *Bovine sp.* leg were obtained from a local butcher shop (Johnstans Butchers, Kings Heath, Birmingham, UK). The average weight of the animal was 310 kg (confirmed by the butcher and verified with DEFRA's statistics [*DEFRA, 2012*]). There were several samples which I have analyzed for qualitative analysis or surface morphology analysis, among them four explants of cartilage have undergone roughness or quantitative investigations. These four explants came from the same animal's lateral humeral condyle within a 20 mm × 20 mm region (figure 3.6). Trials were carried out with plenty of samples which are not

calibrated with AFM because of prolonged scan duration. The samples were obtained only after slaughter for human consumption, no living beings were sacrificed for our experiments. Health and safety regulations [*Birmingham, 2010*] towards biological specimen handling, chemical handling and waste management were followed.

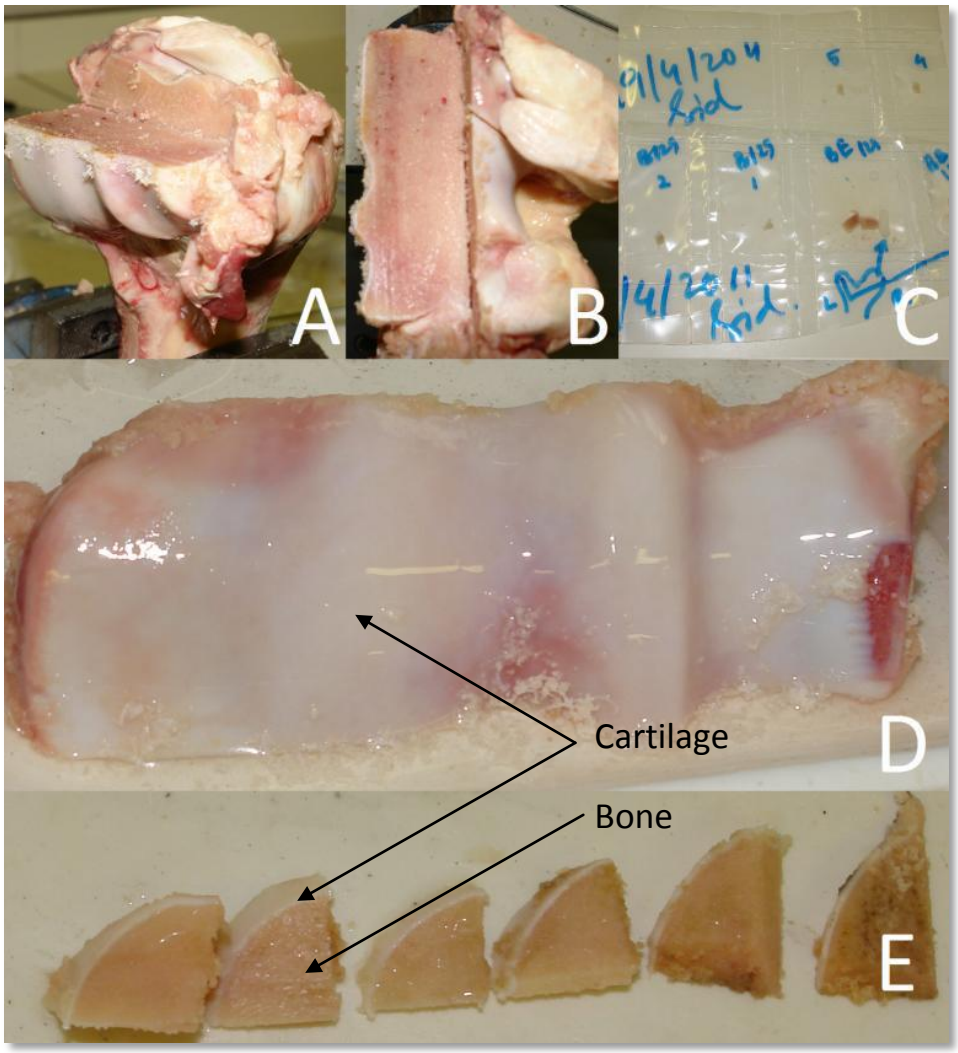

Figure 3.6. The above leg was obtained from a cow (*Bovine sp*.) 3.6.A and 3.6.B are excised lateral condyle zone, 3.6.D is the lateral condyle part with cartilage and 3.6.E excised cartilage C, finally only slight bony parts remain in it.

The cartilage samples were handled in a Class II laboratory. Quarter-strength Ringer's solution was prepared by dissolving a tablet of 1.2 g (Oxoid Ltd, Hampshire, UK) into 500 mL of distilled water and was used to keep the samples hydrated. Sodium Azide (Sigma Aldrich, Missouri, US) was added to the Ringer's solution to prevent the growth of bacteria.

Due its articular cartilage's water content, dehydration is essential to achieve the required vacuum level for electron microscopy imaging. On the other hand, it denatures the native structural conformation when it loses water. To avoid this miss-configuration of collagen fibers and GAG molecules, fixation of the native structure is an essential requirement before dehydration.

Figure 3.7.A. Critical point drier of carbon dioxide and 3.7.B sputtering system of platinum.

The explants were fixed with 2.5 % glutaraldehyde (Agar Scientific Ltd, Essex, UK) solution in 0.1 M physiological equivalent phosphate buffer solution added with 8% paraformaldehyde (Sigma Aldrich, Missouri, US) (see appendix B for preparation) for 20 minutes at room temperature prior to dehydration [*Shepherd et al., 1977; Gwynn et al., 2001*]. This involved 50%, 70%, 90%, 100% ethanol (Sigma Aldrich, Missouri, US) and 100% dry ethanol being applied for 10 minutes to desiccate the water content. Supercritical drying was then used to remove the internal fluid from the sample [*Kääb et al., 1999*] and carbon dioxide was used as the supercritical drying agent (CO_2 supercritical point is 31.1 °C at 7.4 × 10^4 mBar) to allow it to flow without resistance. The E3000 Critical Point Dryer (Polaron Equipment Ltd., Hertfordshire, England – figure 3.7.A) is the critical point dryer used in the experiments. After desiccation the samples were sputtered

with ~10 nm of Platinum (Pt) to avoid charging effects under SEM. An Emscope SC-650 (TAAB Laboratories Equipment Ltd., Birkshire, UK – figure 3.7.B) was used for sputtering. Preliminary experiments were undertaken to investigate the effect of the chemicals and none was found [see appendix C].

3.4. ELECTRON MICROSCOPY

3.4.1 IMAGING

Scanning Electron Microscopy (SEM) was used to image the surfaces of the materials using equipment based in the Centre for Electron Microscopy, University of Birmingham, UK. The machine used was a Philips XL-30 FEG ESEM (FEI Company, Hillsboro, USA), as shown in figure 3.8. The machine has a field emission electron gun source and it can work within a broad range of vacuum levels from low to high (10^{-5} to 10^{-7} mbar). The microscope can be operated in different modes: cryogenic temperature ESEM and normal high vacuum SEM mode. The experiments presented here were carried out at normal high vacuum SEM mode with secondary electron emission detection (SE detector).

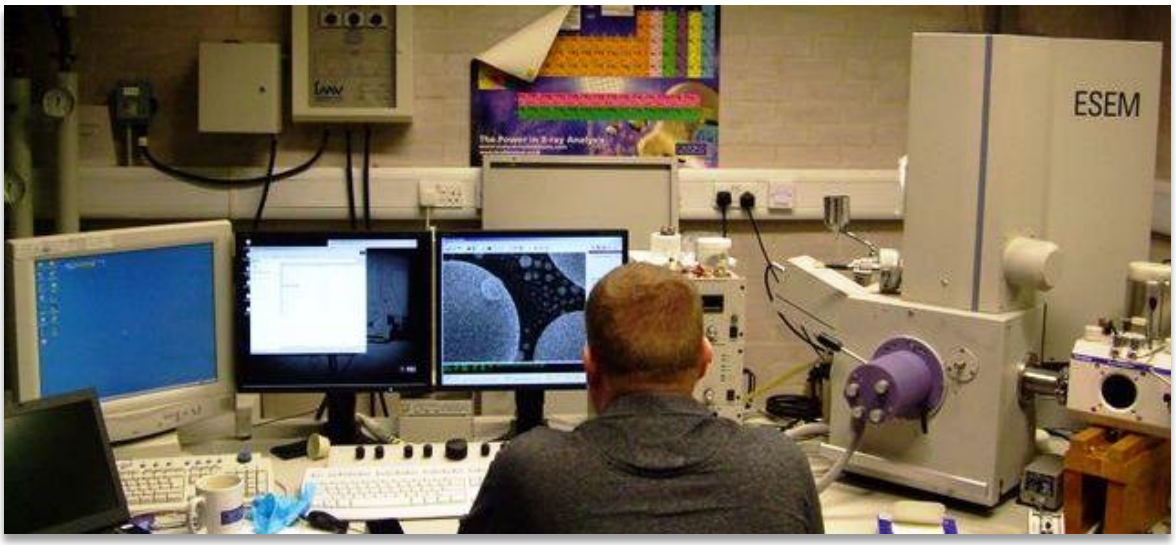

Figure 3.8. Philips XL 30 FEG ESEM.

ESEM was also employed and the related problem is described in appendix D. At high vacuum SEM, the standard surface and cartilage surfaces are observed and images are captured at different magnifications of 500×, 800×, 1200× and 2000×. PDMS and cartilage surfaces were prepared for SEM. High vacuum pressure i.e. less than 10-7 mbar was used to obtain high resolution images of the cartilage surface. All the images were scanned at 10 kV accelerating voltage of the electron beam and the working distance was always less than 10 mm (WD).

3.4.2. STEREOSCOPIC 3D ELECTRON-TOPOGRAPHY

The background and theory of stereoscopic imaging was discussed in chapter II. With the knowledge of that computation approach, a set of *eucentric* (differential angular views of) electron microscopy images have been used to reconstruct the surface of PDMS and articular cartilage in three-dimensions. The images of a constant area of certain magnification were captured from an angular view of +Δ5° (95°), Δ0° (90°) and -Δ5° (85°). The setup of the stage on the SEM was manual so it was only possible to capture eucentric image with a magnification of up to 2000×. Capturing eucentric images of a constant region at higher magnification without digital actuation is a difficult job, since tilting at higher magnification results in a higher order of lateral displacement which enhances the probability of losing the track on a constant area. The experimental setup is represented schematically in figure 3.9, where the blue stage is perpendicular to the electron beam with a differential angle of Δ0° and the dotted tilted zone is differential tilted view at ± Δ5°.

Surface reconstruction and surface characterization were performed with MeX 5.0.1 software (Alicona Imaging GmbH, Grambach/Graz, Österreich) under Windows XP 32bit platform [*Alicona, 2008*]. (The details of the algorithm has already discussed in chapter II).

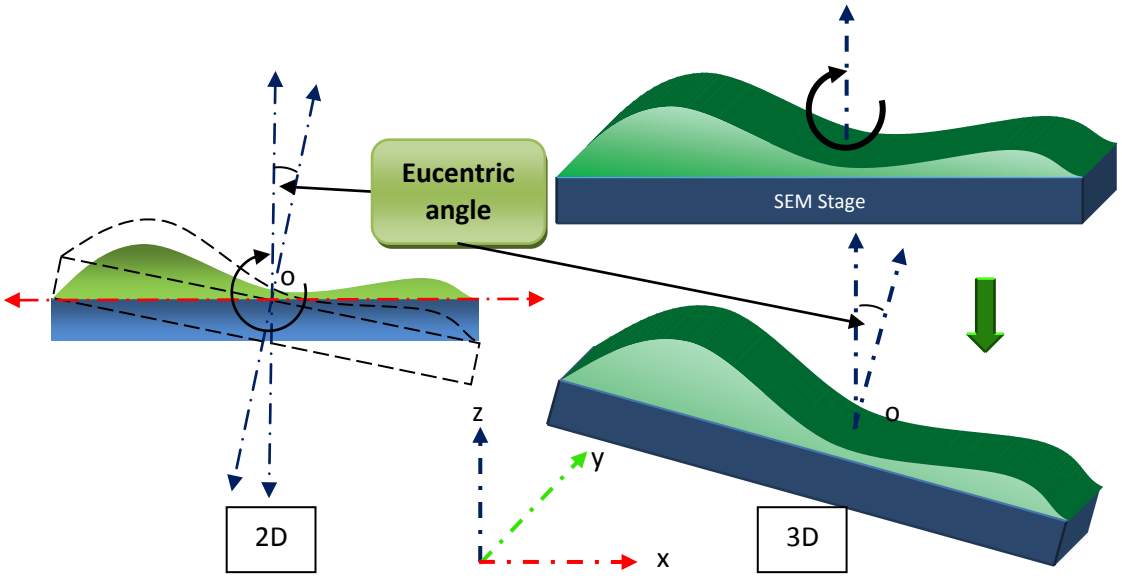

Figure 3.9. Eucentric tilting of sample where 'O' is the point with respect to that the sample should rotate.

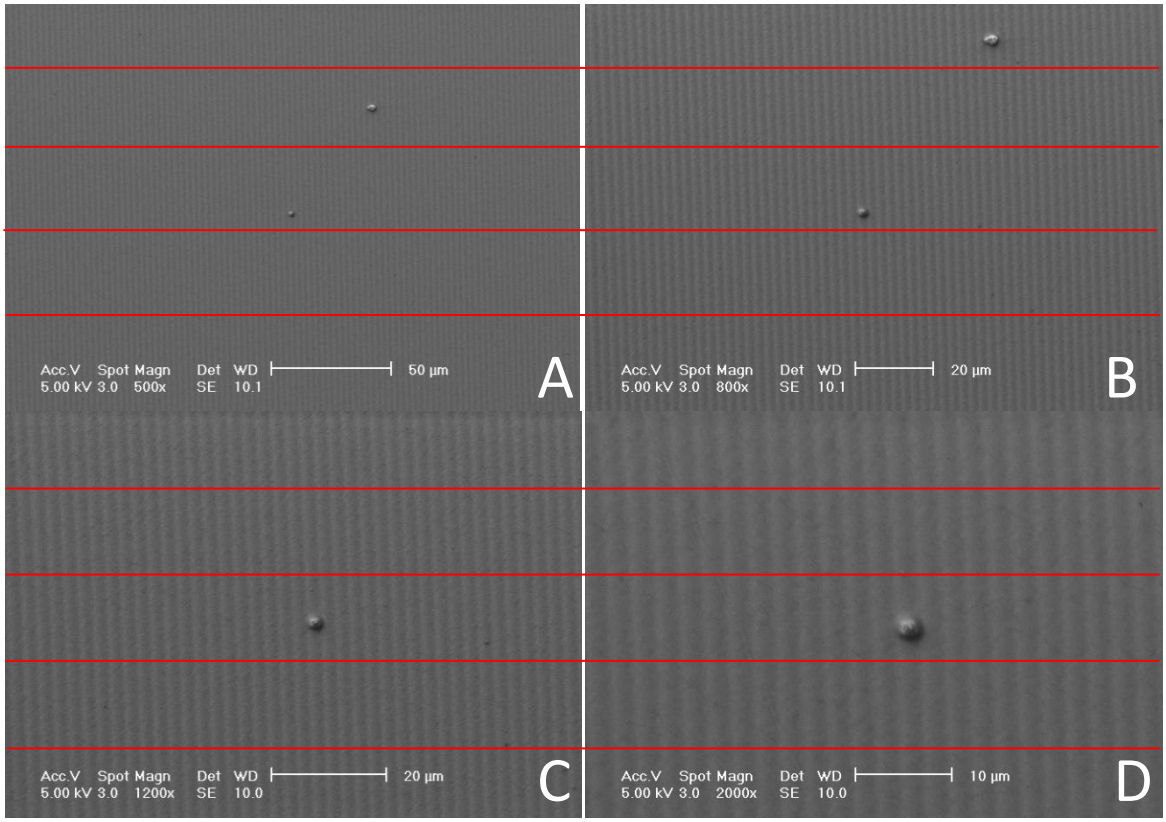

Figure 3.10. The uniform nano-roughened PDMS surface under SEM at 500× (A), 800× (B), 1200× (C) and 2000× (D). The red line shows the approximate position of Ra value measurements for four iterations of each sample.

Six PDMS surfaces were measured using three-dimensional electron-topography. After this verification, four cartilage surfaces were investigated for roughness characterisation. The mean profile roughness was determined at

different magnification factors with four iterations of evenly spacing profile line (figure 3.10 and 3.11) for each sample; the total surface roughness was also quantified. To determine the dependence of magnification factor, a systematic study was carried out for PDMS and the cartilage surface where I considered four different magnification factors (500×, 800×, 1200× and 2000×). The area of scan will decrease as magnification increases (here, from 240 × 170 μm^2 to 60 × 40 μm^2).

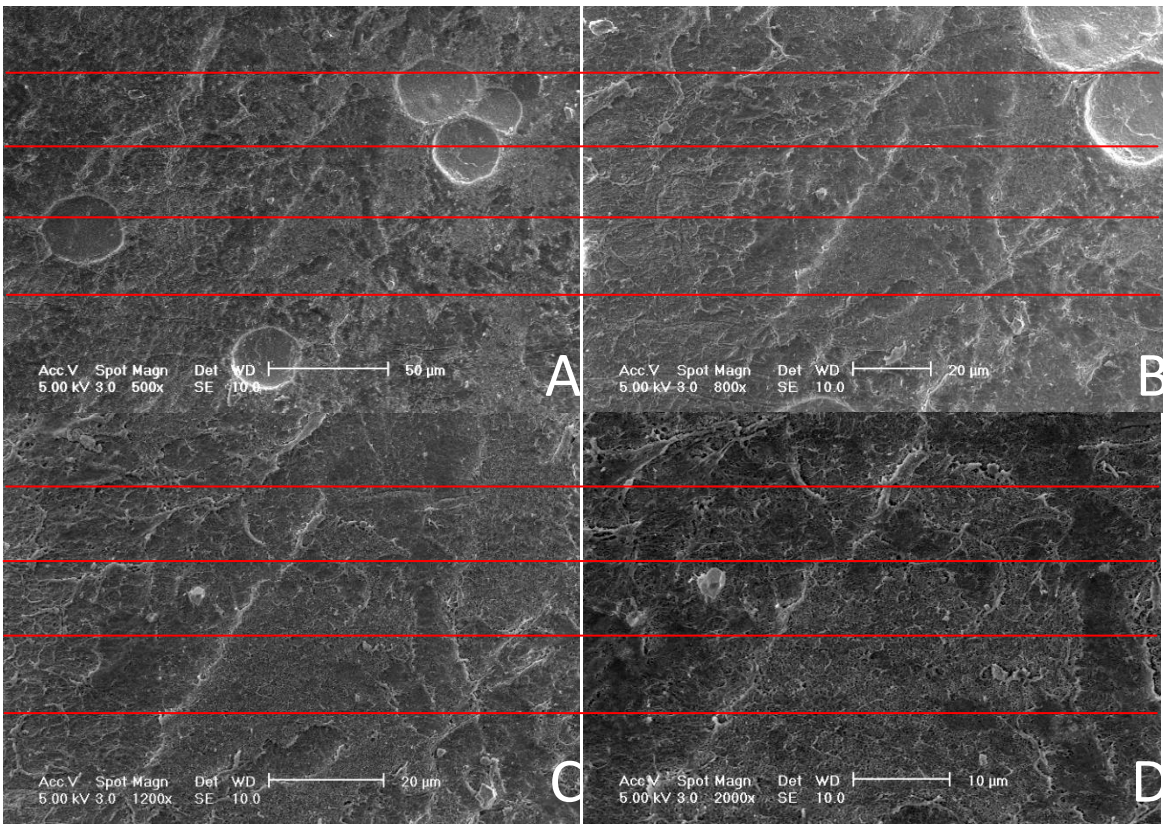

Figure 3.11. Magnification factor of (A) 500×, (B) 800×, (C) 1200× and (D) 2000× has utilized to visualize a region of the bovine humeral lateral condyle articular cartilage. The red line shows the approximate position of Ra value measurements for four iterations of each sample.

3.5. Atomic Force Microscopy

After the electron microscopy characterisation, the same samples were measured using Atomic Force Microscopy. A Nanowizard model (JPK Instruments AG, Berlin, Germany – figure 3.12) was used to obtain a set of roughness values with a ~10 nm diameter CSC17 Silicon cantilever purchased from MIKROMASCH, Tallinn, Estonia. Constant areas of 25 × 25 μm^2 were

scanned on the PDMS and articular cartilage (the area of scan is less than the SEM scan area. This provides the local distribution of roughness. So, number of trials with different samples ultimately determines the reproducibility.). Three-dimensional topography from the force mapping was obtained with AFM. Initially the profile roughnesses of PDMS and cartilage were measured at four evenly oriented spaces (similar to electron topography). The mean value was then calculated along with the standard deviation. The total surface roughness of each sample was also determined.

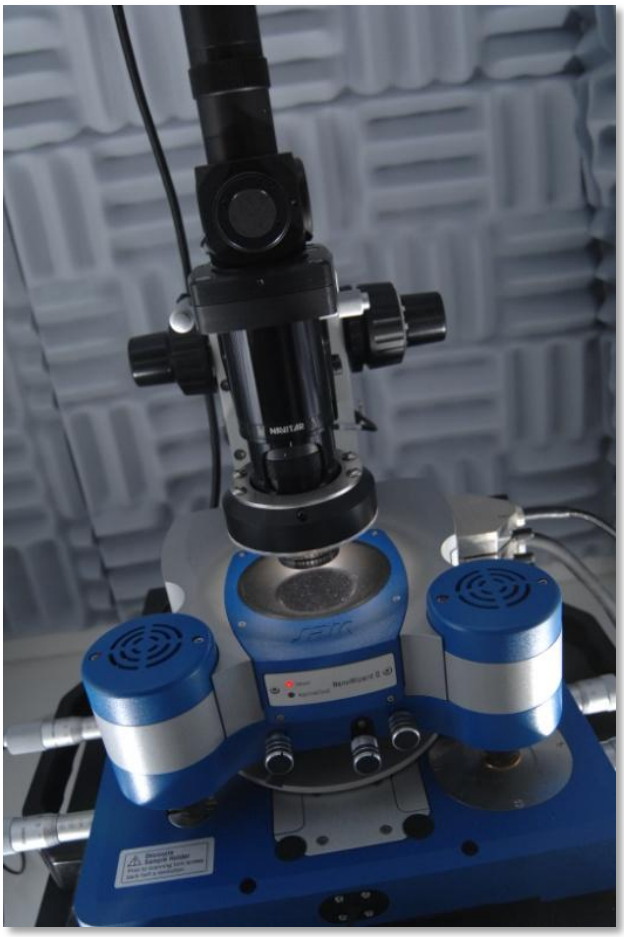

Figure 3.12. The atomic force microscopy system, model Nanowizard manufactured by JPK Instruments AG, Berlin, Germany.

3.6. DATA ANALYSIS

Surface roughness values obtained with the 3D electron-topography were plotted against corresponding captured magnification factor to find the distributions between roughness and magnification factor. This helps to

determine the correlation between roughness and magnification factor. This is done with simple linear regression analysis. From six PDMS surfaces, I achieve an empirical correlation between roughness (mean profile and surface) and magnification factor. The same analysis was carried out with four articular cartilage samples. The correlation was obtained with critical parameters like slopes (m), y intercepts (c) and coefficient of determinants (R^2) of the fitted function. Beside these, to understand the level of significance p value analysis were also taken into account. Where, the level of significance for the p value was considered to be less than 0.05.

AFM roughness values were utilised to calibrate the roughness values measured from three-dimensional electron topography. Obtained roughnesses for six PDMS samples and four cartilage samples at each magnification factors were plotted against AFM roughness. A comparison with an ideal linear function between AFM roughness and 3D electron-topography roughness was also obtained.

The software employed for the above anslysis were Microsoft Office XL 2007, Minitab 15 and MATLAB R2010.B.

CHAPTER IV

RESULTS

4.1. PDMS

4.1.1. SCANNING ELECTRON MICROSCOPY

The SEM images of the PDMS surface were uniform and had a sinusoidal distribution (as we can observe in figure 4.1). The surfaces shown were scanned with magnifications of 500× (figure 4.1.A) and 1200× (figure 4.1.B). One of the 3D-toporgaphic reconstructions of PDMS SEM surface captured at 2000× of magnification factor is shown in figure 4.2.

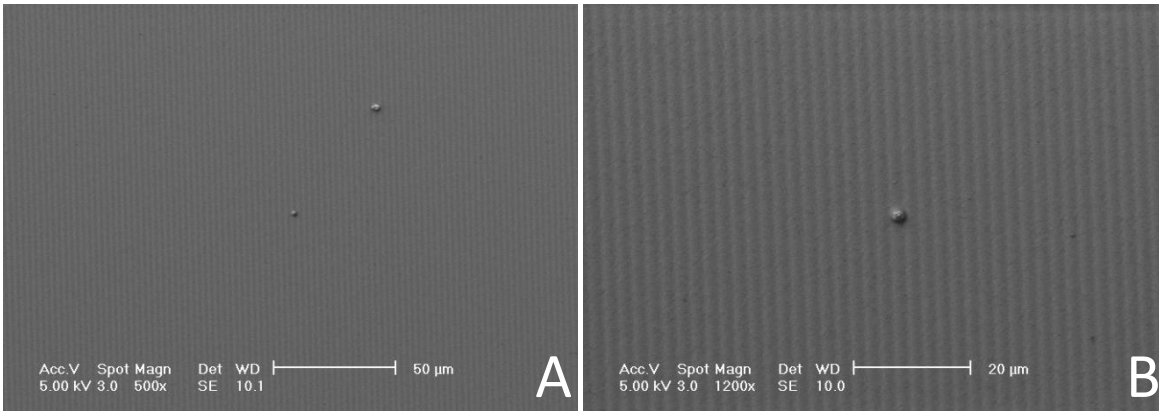

Figure 4.1. The uniform nano-roughened PDMS surface under SEM at 500× (A) and 1200× (B).

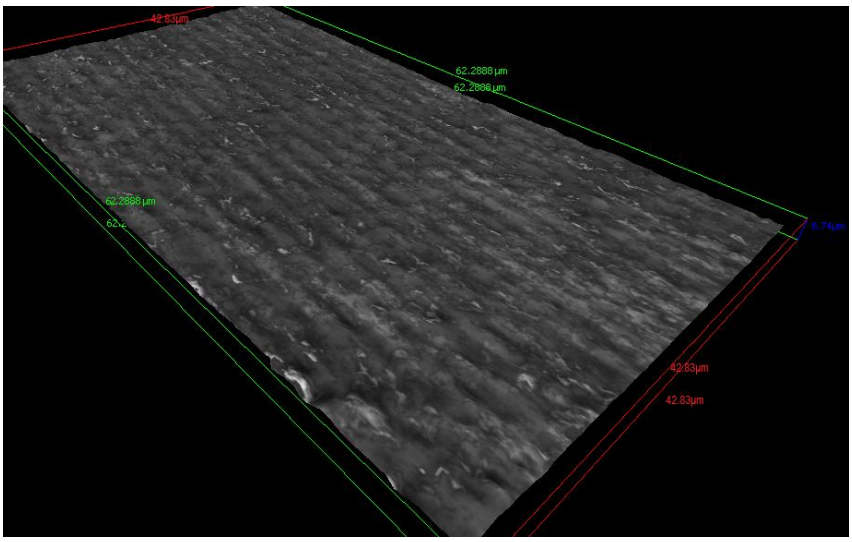

Figure 4.2. The topographic reconstruction of three dimensional surfaces of polydimethylsiloxane (PDMS) at 2000×. The surface roughness of these surfaces has been quantified in the next section.

4.1.2. Roughness Characterization with 3D Electron-Topography

Profile roughness measurement (R_a) and surface roughness measurement (S_a) of six samples of PDMS (PDMS-1 – 6) are tabulated in table 4.1. Four iterations of profile roughness (the red lines shown in figure 3.10 in chapter III) are represented as $R_{a1\text{-}4}$ and their mean, standard deviation and total surface roughness are denoted as R_{am}, S_{Dev} and S_a, respectively.

Table 4.1. PDMS sample profiles and surface roughness values at different magnifications (the subscripts of sample notations correspond to the magnification factor).

Sample No.	Profile roughness (nm)				Mean Profile Roughness (nm)	Standard Deviation (±nm)	Total surface roughness (nm)
	R_{a1}	R_{a2}	R_{a3}	R_{a4}	Ra_m	S_{Dev}	S_a
PDMS-1$_{500\times}$	63	51	79	63	64	11.48	87
PDMS-2$_{500\times}$	42	61	58	48	52.25	8.80	72
PDMS-3$_{500\times}$	67	58	82	61	67	10.67	91
PDMS-4$_{500\times}$	75	67	52	82	69	12.88	99.1
PDMS-5$_{500\times}$	69	61	46	78	63.50	13.57	84
PDMS-6$_{500\times}$	83	71	63	71	72	8.24	87
PDMS1$_{800\times}$	131	127	142	139	134.75	6.94	183
PDMS2$_{800\times}$	97	91	128	89	101.25	18.15	135
PDMS3$_{800\times}$	142	129	176	125	143	23.16	181
PDMS4$_{800\times}$	143	138	119	178	144.50	24.61	185
PDMS5$_{800\times}$	129	131	192	142	148.50	29.55	185
PDMS6$_{800\times}$	172	151	133	149	151.25	16.00	191
PDMS-1$_{1200\times}$	257	252	261	342	278	42.82	278
PDMS-2$_{1200\times}$	215	263	241	169	222	40.41	283
PDMS-3$_{1200\times}$	295	278	261	372	301.50	49.00	292
PDMS-4$_{1200\times}$	293	278	210	340	280.25	53.76	351
PDMS-5$_{1200\times}$	271	259	284	291	276.25	14.17	298
PDMS-6$_{1200\times}$	253	289	251	321	278.50	33.28	281
PDMS-1$_{2000\times}$	683	592	513	467	563.75	94.79	1126
PDMS-2$_{2000\times}$	489	531	462	481	490.75	29.12	837
PDMS-3$_{2000\times}$	710	739	561	582	648	89.53	962
PDMS-4$_{2000\times}$	783	632	501	678	648.50	116.89	829
PDMS-5$_{2000\times}$	670.9	521	831	776	699.72	136.41	862
PDMS-6$_{2000\times}$	532	591	525	798	611.50	127.80	819

The range of roughness values of PDMS is between 52.25 ± 8.8 nm and 699.72 ± 136.41 nm. The minimum and maximum values of S_a are 72 nm and 1126 nm, respectively. Mean profile roughness (R_{am}) of PDMS was plotted against magnification factor. Two datasets are linearly fitted, in figure 4.3 – 4.8 for PDMS-

1 – 6, respectively. The linear regression for all PDMS samples holds a very close relation. The parameters of linear function have been tabulated in table 4.2.

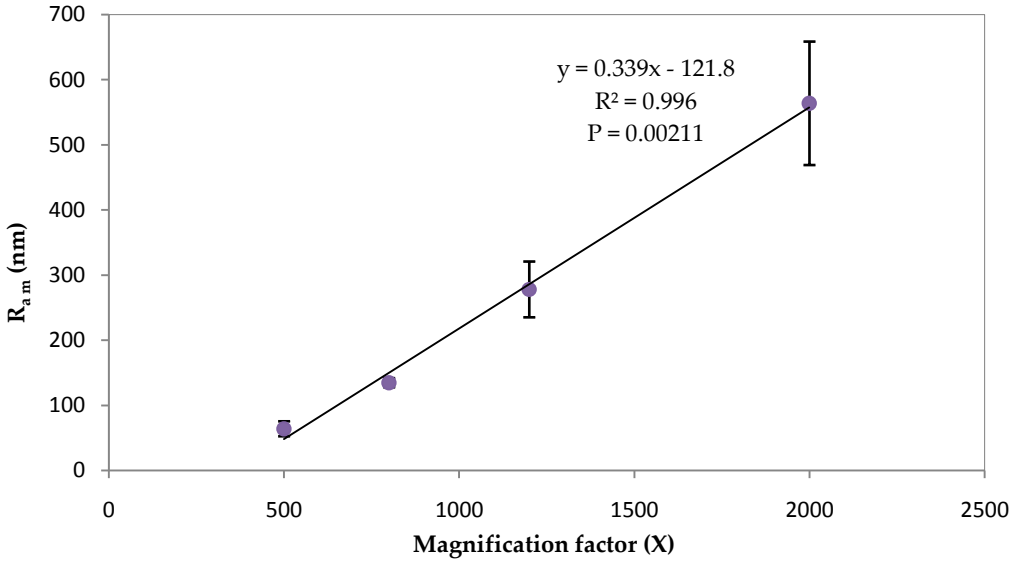

Figure 4.3. Mean profile roughness R_{am} (nm) of PDMS-1 plotted against magnification factor (×). Error bars represent the standard deviation.

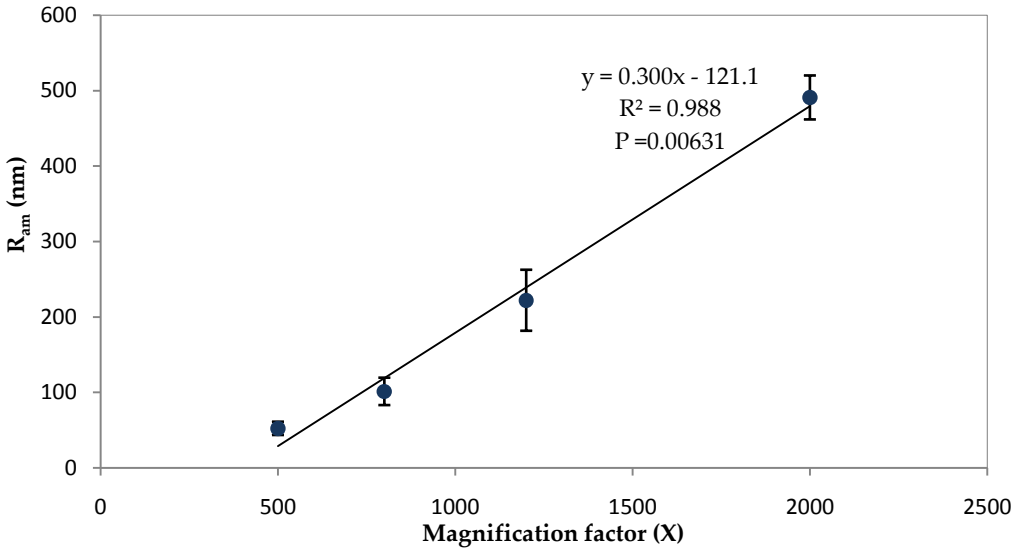

Figure 4.4 Mean profile roughness R_{am} of PDMS-2 plotted against magnification factor (×). Error bars represent the standard deviation.

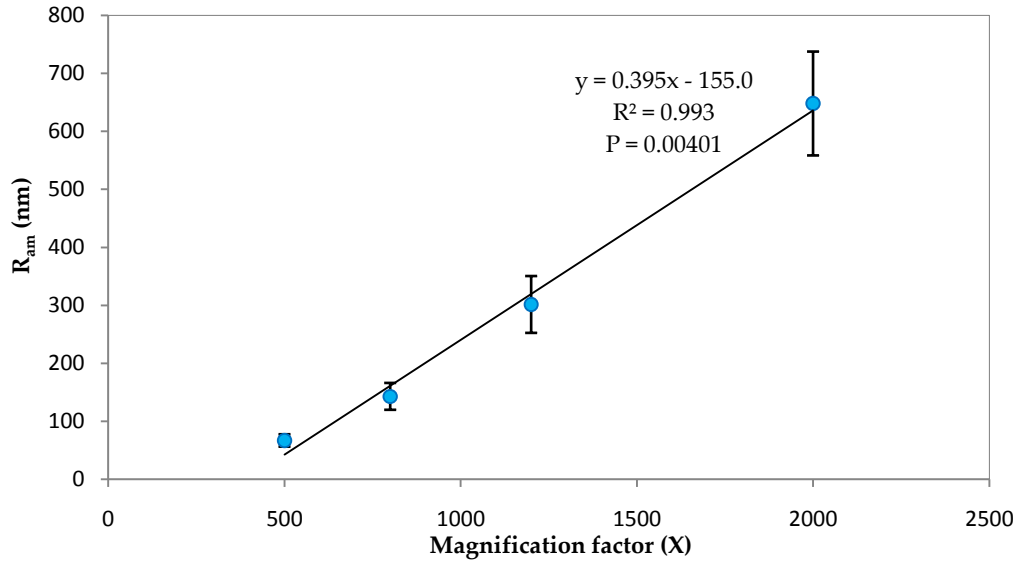

Figure 4.5. Mean profile roughness R_{am} of PDMS-3 plotted against magnification factor (×). Error bars represent the standard deviation.

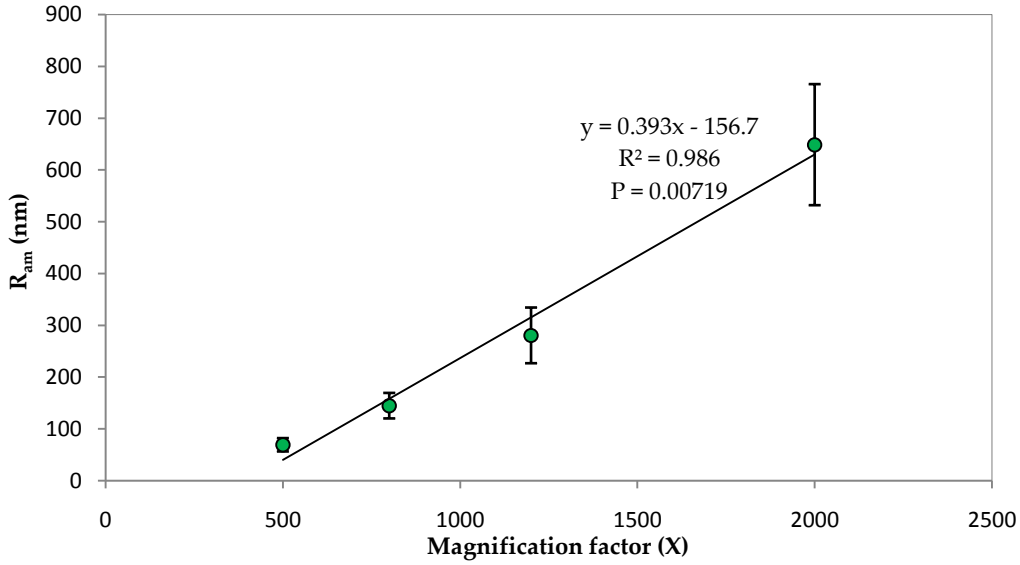

Figure 4.6. Mean profile roughness R_{am} of PDMS-4 plotted against magnification factor (×). Error bars represent the standard deviation.

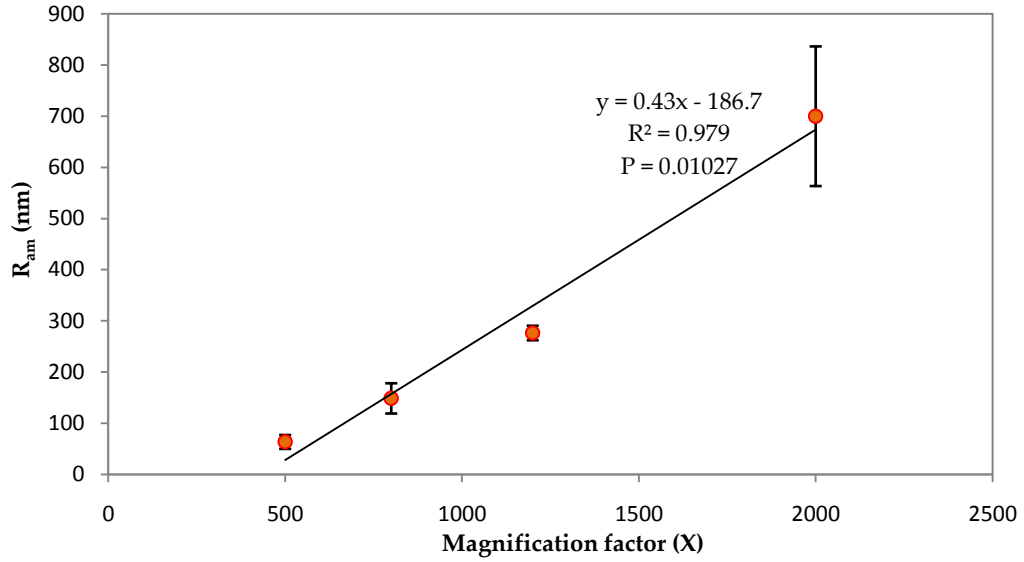

Figure 4.7. Mean profile roughness R_{am} of PDMS-5 plotted against magnification factor (×). Error bars represent the standard deviation.

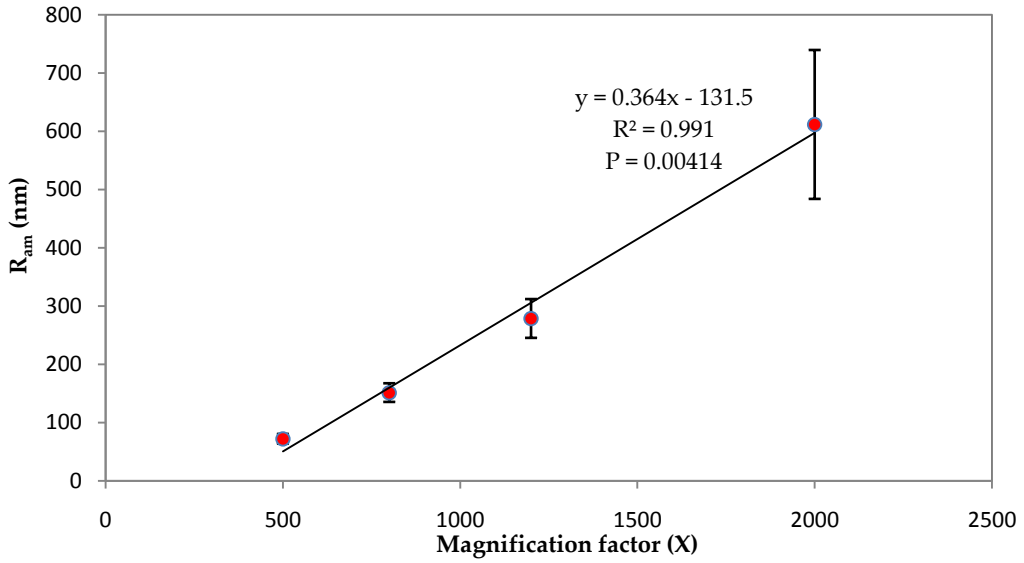

Figure 4.8. Mean profile roughness R_{am} of PDMS-6 plotted against magnification factor (×). Error bars represent the standard deviation.

For all the plots $p<0.05$ which infers a significant relation. As compared in table 4.2, the slope or *m* values of all fitted lines are positive and very close to each other. The intercept of *y* or *c* are also in very close proximity with negative values. The fitness of data-points of every instance is greater than 97%. The smallest R^2 value is 0.979 (for PDMS-5) and the best fitted line is obtained with PDMS-1 where the R^2 is 0.996.

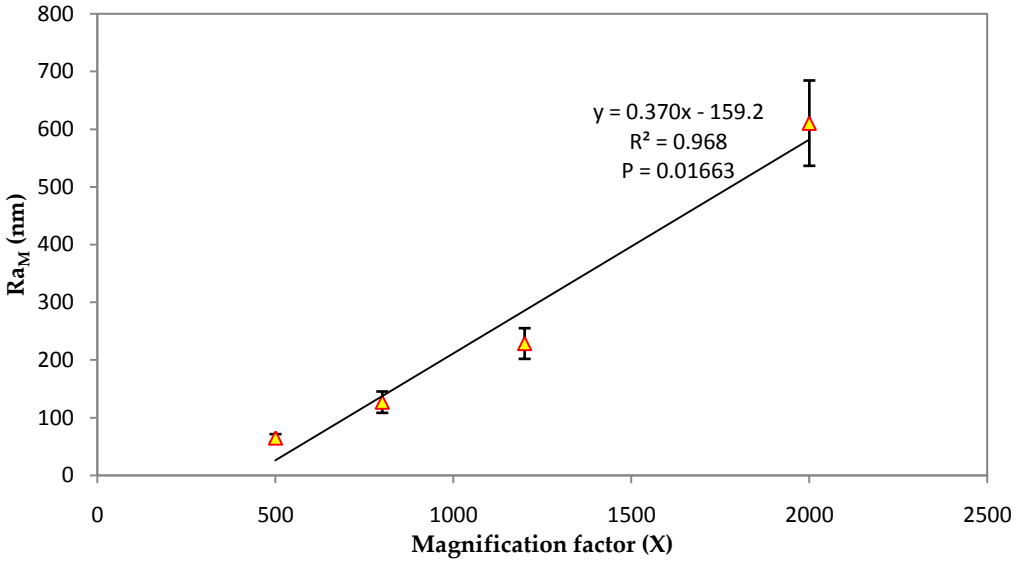

Figure 4.9. Ra_M i.e. mean Ra_m of all sample (PDMS-1 – 6) for 500×, 800×, 1200× and 2000× has been plotted here. Error bars represent the standard deviation.

The comparative analysis fit the data with a linear trend line that gave a good fit. [comment: "a power fit could also have been used, but the R^2 values were similar to the linear fit. More data points would be required to confirm the exact relationship."] The mean of all the profile roughness values and mean of the all the total surface roughness values (of specific magnification factor) have been quantified and plotted against corresponding factor of magnification in figure 4.9 and 4.10, respectively.

Table 4.2. Comparative regression analysis of linear relation between magnification factor and profile roughness of PDMS-1 – 6. Here, m, c, R^2 and p(x) denote slope, y-intercept, coefficient of determinant and statistical significance respectively.

Sample Considered	Slope of the curve	Intercept at *y* axis	Coefficient of determinants	Statistical significance
	m (+/-)	*c (nm)*	R^2	*p value*
PDMS -1	+0.339	-121.8	0.996	0.00211
PDMS-2	+0.300	-121.1	0.988	0.00631
PDMS-3	+0.395	-155.0	0.993	0.00401
PDMS-4	+0.393	-156.7	0.986	0.00719
PDMS-5	+0.430	-186.7	0.979	0.01027
PDMS-6	+0.364	-131.5	0.991	0.00414

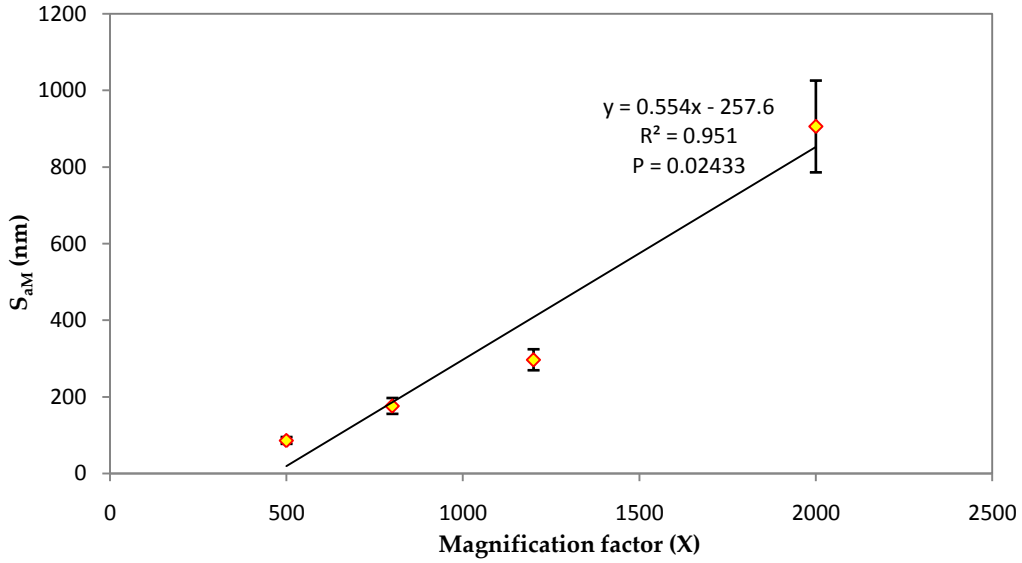

Figure 4.10. S_{aM} i.e. mean S_a of all samples (PDMS-1 – 6) for 500×, 800×, 1200× and 2000× has been plotted here. Error bars represent the standard deviation.

The PDMS standard sample has shown a linear relationship between roughness and magnification.

4.1.3. Atomic Force Microscopy

After the three-dimensional electron microscopic analysis of the PDMS, the samples were then scanned with AFM. The surface result is very close to the three-dimensional topography of electron microscopy (figure 4.11).

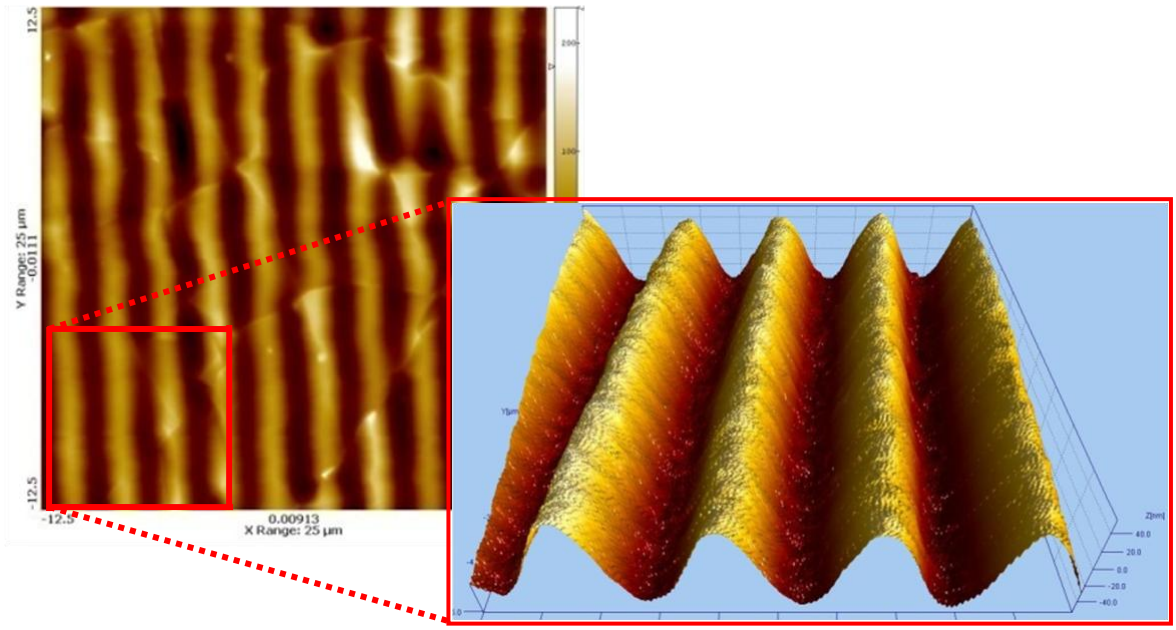

Figure 4.11. The atomic force microscopy surface of PDMS where the surface was sinusoidal. The global area scanning was 25 µm × 25 µm and the 3D topography is of 10 µm × 10 µm.

Table 4.3. Roughness of standard PDMS samples measured by AFM. Profile roughness (Ra_{1-5}), Mean profile roughness (R_{am}) and Total surface roughness (S_a).

Sample No.	Profile Roughness (nm)					Mean of profile roughness (nm)	Standard Deviation (± nm)	Total Surface Roughness (nm)
	R_{a1}	R_{a2}	R_{a3}	R_{a4}	R_{a5}	R_{am}	S_{Dev}	S_a
PDMS-1	24.9	25.7	26.9	24.9	26.0	25.68	0.83	28.9
PDMS-2	25.1	24.8	25.9	22.3	25.6	24.74	1.42	29.4
PDMS -3	24.7	24.9	26.1	24.9	25.9	25.30	0.64	28.8
PDMS-4	25.5	25.8	24.9	25.9	47.3	29.88	9.74	28.3
PDMS-5	26.1	24.6	25.1	27.0	26.5	25.86	0.99	29.1
PDMS-6	24.3	25.7	24.9	25.1	25.1	25.02	0.50	29.5

The surface was sinusoidal as we can see in figure 4.11. The values of surface roughness obtained from atomic force microscopy are shown in table 4.3.

4.1.4 Comparison of 3D electron-topography and AFM

The mean profile roughness values from the 3D electron-topography (table 4.1) are plotted against mean profile roughnesses obtained from AFM in figures 4.12 – 4.15. Figures 4.12, 4.13, 4.14 and 4.15 are plots of magnification factor of 500×, 800×, 1200× and 2000×, respectively.

The data are fitted with a linear regression. In the ideal condition, where roughness values obtained from the 3D electron-topography matched the values from AFM, then the points should have passed through a line of slope 1 that intercepts at the origin. The green dashed line in all the plots are the ideal lines.

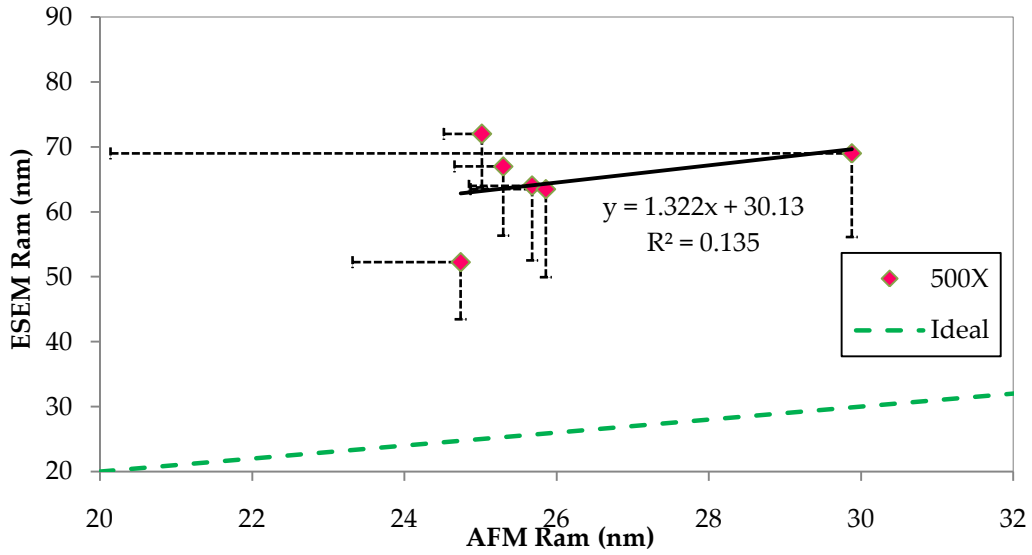

Figure 4.12. Plot of mean profile roughness (ESEM Ram) obtained from electron-topography at 500× against mean profile roughness obtained from AFM (AFM Ram). Error bars represent standard deviations (towards positive as well).

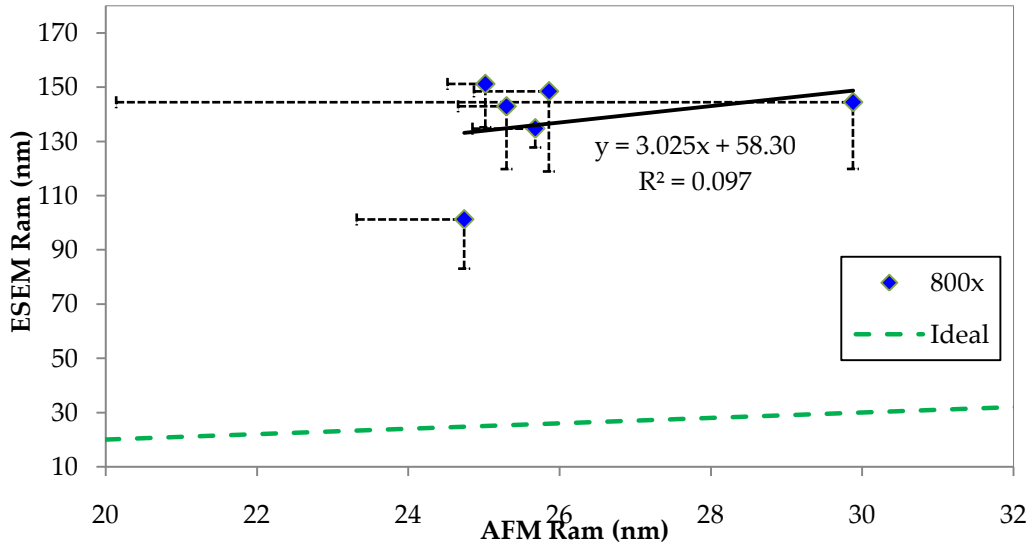

Figure 4.13. Plot of mean profile roughness (ESEM Ram) obtained from electron-topography at 800× against mean profile roughness obtained from AFM (AFM Ram). Error bars represent standard deviations (towards positive as well).

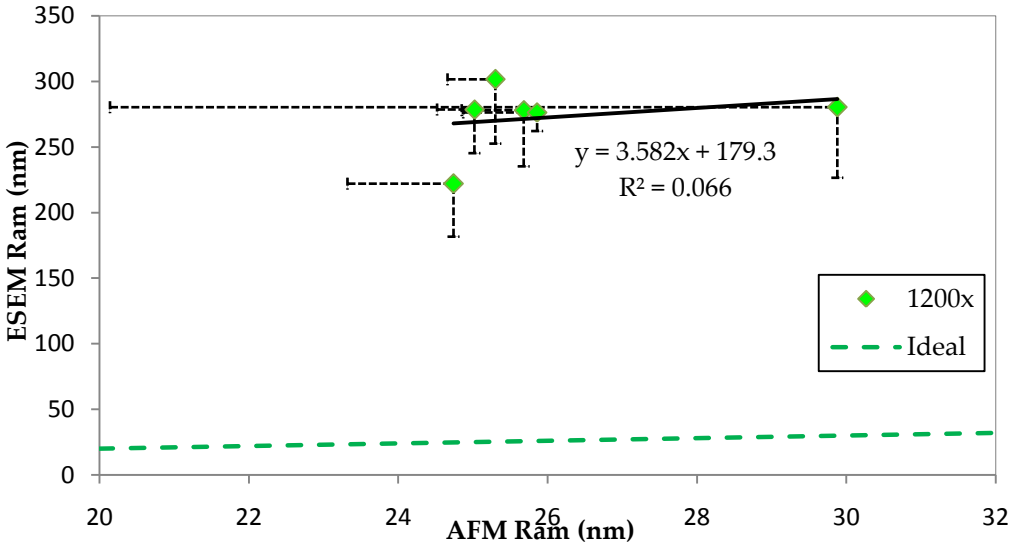

Figure 4.14. Plot of mean profile roughness (ESEM Ram) obtained from electron-topography at 1200× against mean profile roughness obtained from AFM (AFM Ram). Error bars represent standard deviations (towards positive as well).

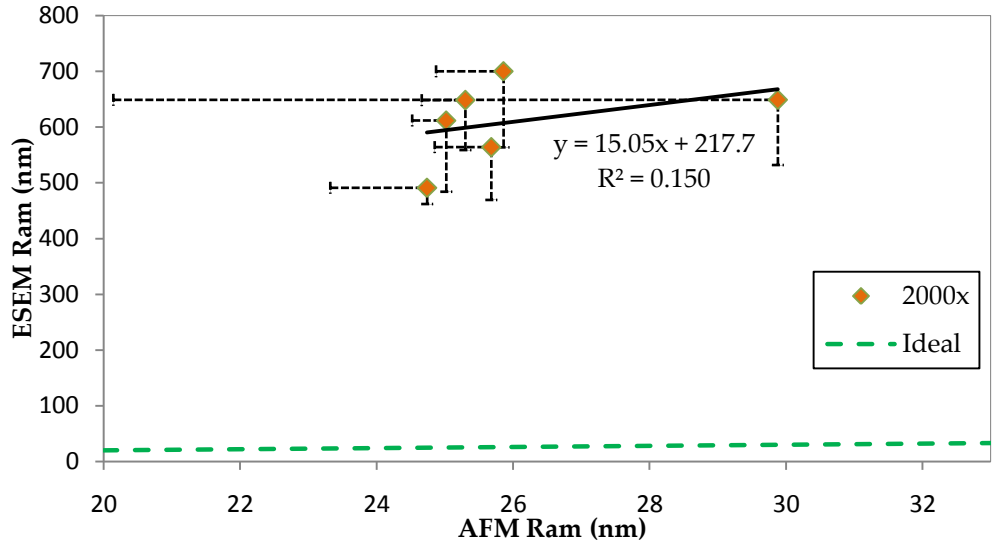

Figure 4.15. Plot of mean profile roughness (ESEM Ram) obtained from electron-topography at 2000× against mean profile roughness obtained from AFM (AFM Ram). Error bars represent standard deviations (towards positive as well).

4.2. ARTICULAR CARTILAGE

4.2.1. SCANNING ELECTRON MICROSCOPY

The bulk surfaces of bovine humeral lateral condyle is shown in figure 4.16. The cartilage has not detached from the bony part. The superficial layer of articular cartilage is extremely inhomogeneous within 200 to 300 μm as shown in 4.17.

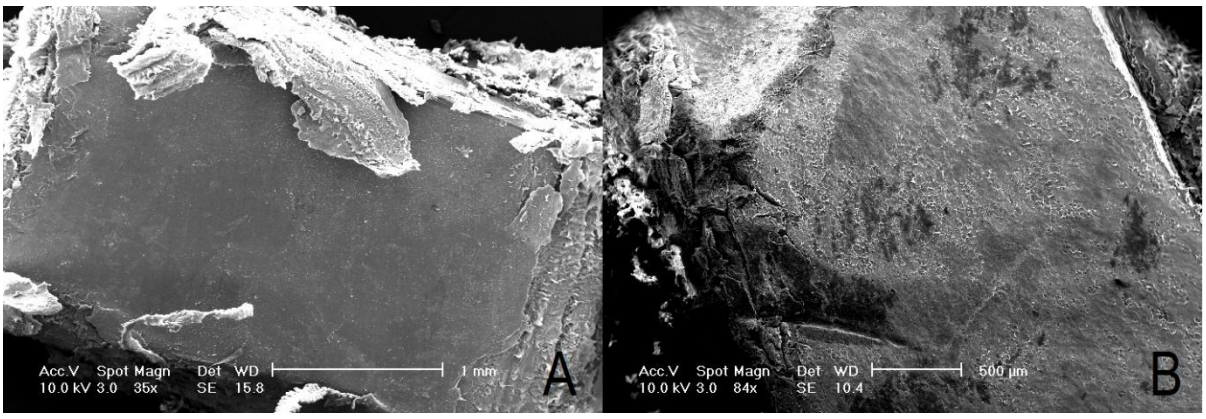

Figure 4.16. A and B are two portions of humeral lateral condyle taken from within couple of millimeter range.

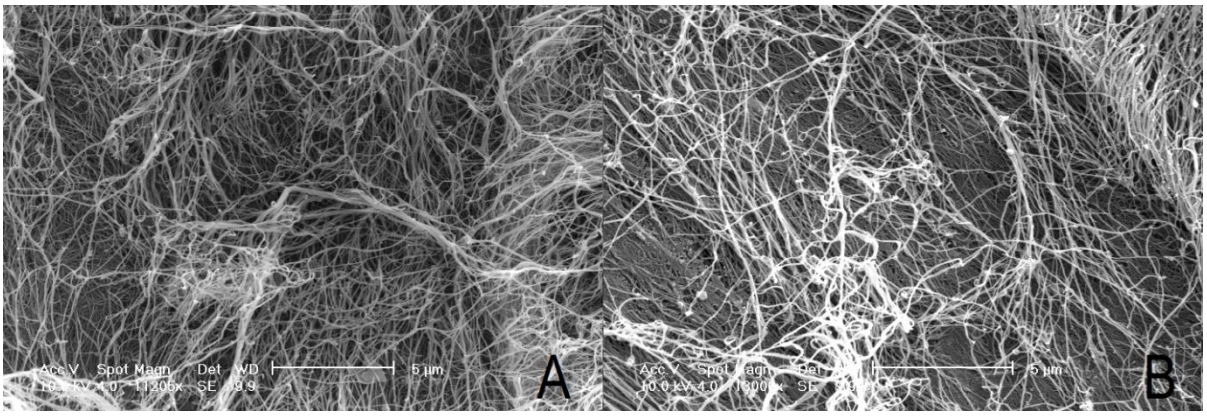

Figure 4.17. The inhomogeneous surface of articular cartilage, A and B are captured within a range of 200 - 300 μm.

The surface shown in figure 4.18 contains defect. The rupture shown in the figure should have a significant effect on total surface roughness. The figure 4.19 shows a reconstructed topography at 2000× magnification. It was obtained from the same joint of humeral lateral condyle. The surface shown in figure 4.19 was encoded as BHLC- 3.

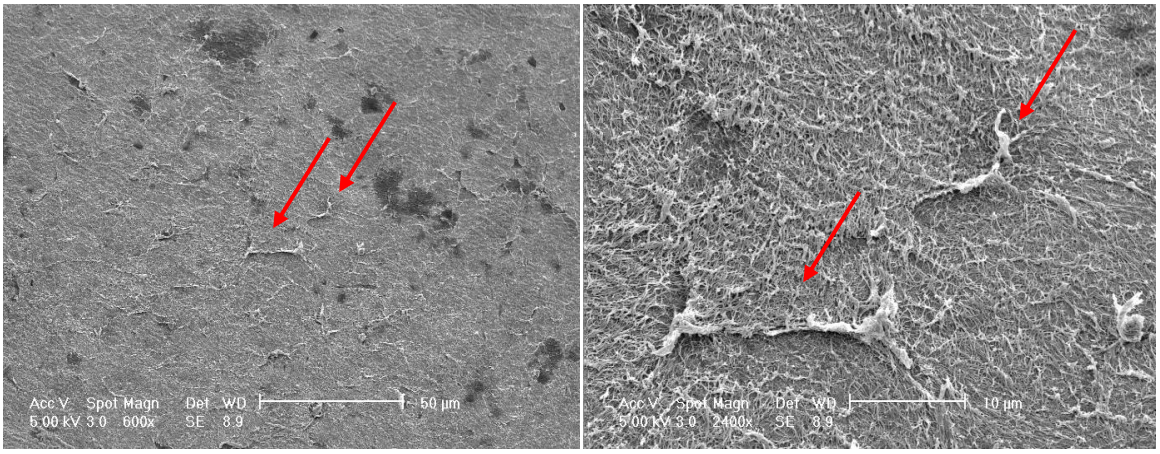

Figure 4.18. The surface contains some evidence of wear at a very small scale. The red arrows indicate ruptured layers.

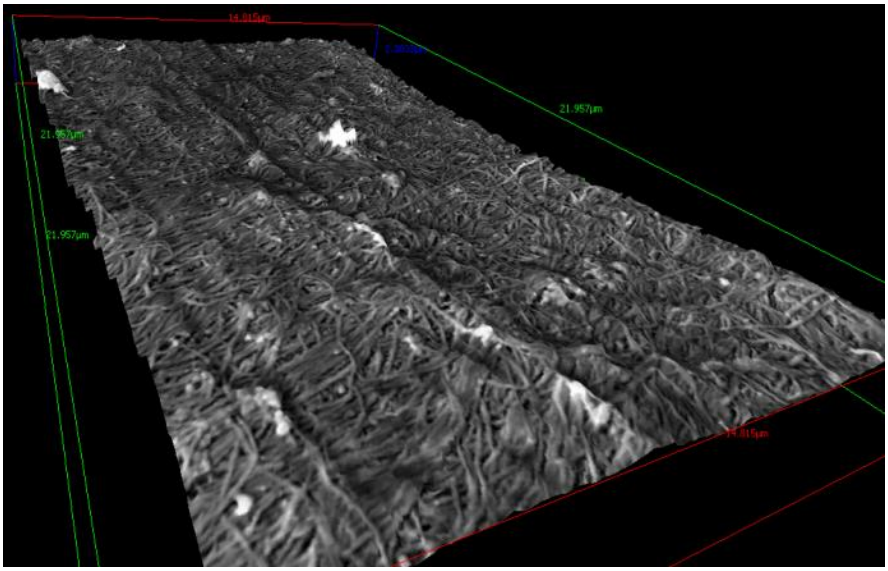

Figure 4.19. Surface of BHLC-3 reconstructed at 2000× of magnification factor.

4.2.2. Roughness characterization with 3D Electron-topography

Three dimensional topography of the articular cartilage of a bovine humeral lateral condyle leads to quantification of surface roughness. Four different magnification factors were considered: 500×, 800×, 1200× and 2000×. The roughnesses at each magnification factor are shown in table 4.4.

Table 4.4. Roughness variation of four articular cartilage explants from a bovine humeral lateral condyle within an area of 20 mm × 20 mm at magnifications of 500×, 800×, 1200× and 2000×; the subscripts of each sample notation is the particular magnification factor at which it has scanned. For profile roughness measurement, each sample has undergone four measurements of roughness quantification from Ra_1 to Ra_4. These four quantified values provide mean Ra_m values with a standard deviation of S_{Dev}; variation of the total surface roughness considering the scanned area is S_a.

Sample No.	Profile Roughness (nm)				Mean Profile Roughness (nm)	Standard Deviation (± nm)	Total Surface Roughness (nm)
	Ra_1	Ra_2	Ra_3	Ra_4	Ra_m	S_{Dev}	S_a
BHLC-1$_{500\times}$	176.0	168.9	166.3	178.9	172.52	5.90	195.3
BHLC-2$_{500\times}$	258.2	260.1	170.9	165.1	213.57	52.68	231.1
BHLC-3$_{500\times}$	231.0	167.9	154.1	143.0	174	39.34	260.8
BHLC-4$_{500\times}$	166.0	171.5	165.2	158.7	165.35	5.24	183.1
BHLC-1$_{800\times}$	195.1	186.2	188.1	190.7	190.02	3.85	198.1
BHLC-2$_{800\times}$	271.5	282.3	190.0	185.3	232.27	51.75	207.1
BHLC-3$_{800\times}$	251.0	176.1	176.9	163.8	191.95	39.82	231.9
BHLC-4$_{800\times}$	186.5	190.1	190.5	177.9	186.25	5.85	198.9
BHLC-1$_{1200\times}$	112.0	119.2	123.1	136.2	122.62	10.15	147.1
BHLC-2$_{1200\times}$	283.9	291	270.5	286.8	283.05	8.85	295.7
BHLC-3$_{1200\times}$	271.9	192.3	198.9	201.5	216.15	37.36	283.1
BHLC-4$_{1200\times}$	205.1	223.9	236.2	201.9	216.77	16.18	258.2
BHLC-1$_{2000\times}$	63.10	79.20	81.00	61.90	71.3	10.19	85.60
BHLC-2$_{2000\times}$	310.2	299.5	288.7	356.2	313.65	29.69	315.9
BHLC-3$_{2000\times}$	389.3	463.1	410.8	409.2	418.1	31.55	398.1
BHLC-4$_{2000\times}$	326.9	313.5	305.6	325.3	317.82	10.10	318.5

The mean profile roughness i.e. Ra_m was in the range of 71.3 ± 10.1 nm to 418.1 ± 31.5 nm. The total surface roughness S_a was in the range of 85.6 nm to 398.1 nm. The mean profile roughness values obtained in table 4.4 are plotted against corresponding magnification factor in figure 4.20 – 4.23. Figure 4.20, 4.21, 4.22 and 4.23 are plotted for BHLC-1, -2, -3 and -4, respectively. Data obtained from table 4.4 are fitted using a linear regression. After observing the inconsistent roughness values of BHLC-1 (figure 4.20) compared to the other samples (figure 4.21 – 4.23),

table 4.5 has been tabulated with important linear regression parameters for a comparative analysis for all four samples.

Table 4.5 compares the parameters - slope (*m*), intercept at *y* axis (*c*) and coefficient of determinants of fitted lines *(R^2)*. The R^2 determines the goodness of fit of the line which ultimately infers the reliability of the data. For BHLC-2, -3 and -4 R^2 values are more than 0.9 as well as their slopes are positive. On the contrary, for BHLC-1 the R^2 are less than 0.9 and the slope is negative, as well as the intercept of *y* or *c* value is maximum here.

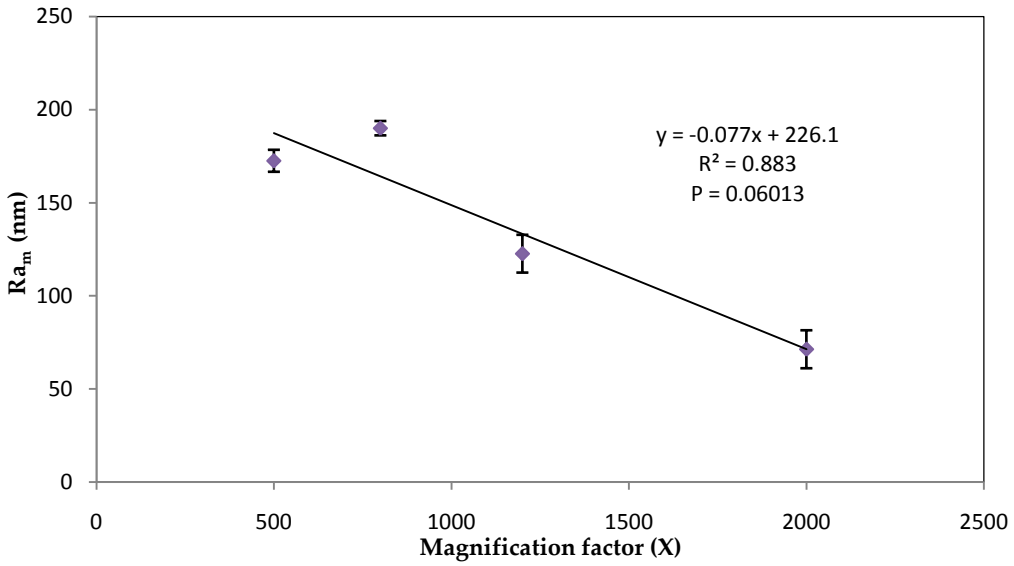

Figure 4.20. Plot of BHLC-1's mean roughness (Ra_m) against magnification factors. Error bars represent the standard deviation

In figure 4.20, as p > 0.05 the relation is not significant, also between 500× and 800× the roughness actually increases. Since the trend of the roughness in BHLC-1 does not follow other samples, a comparative analysis has been carried forward to determine the effect of BHLC-1. The mean profile roughness of the four samples or Ra_m of particular magnification factor has been averaged out and tabulated in table 4.6. In case of Ra_M',BHLC-1 was not considered. But for Ra_M all four samples were considered.

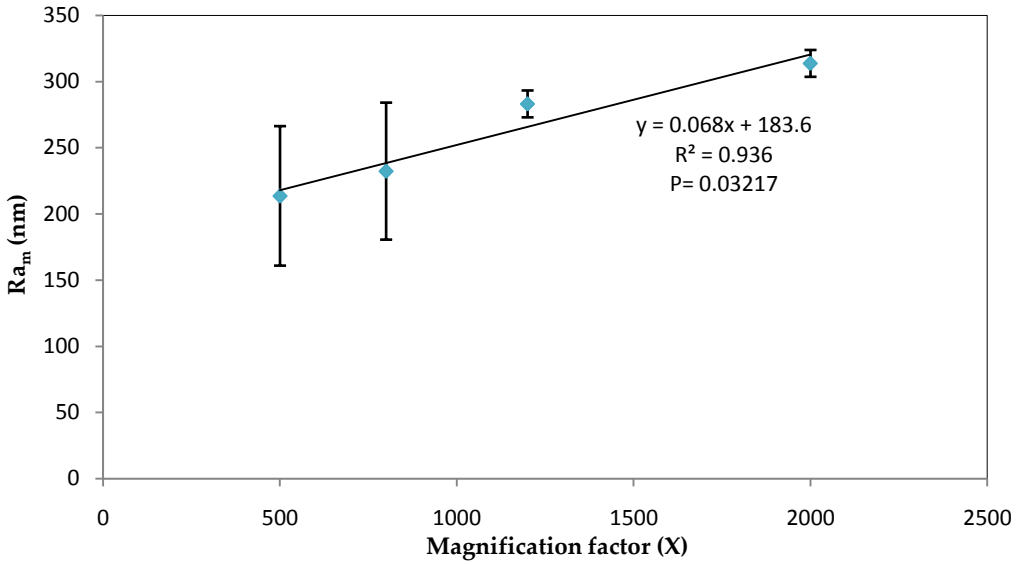

Figure 4.21. Plot of BHLC-2's mean roughness (Ra_m) against magnification factors. Error bars represent the standard deviation

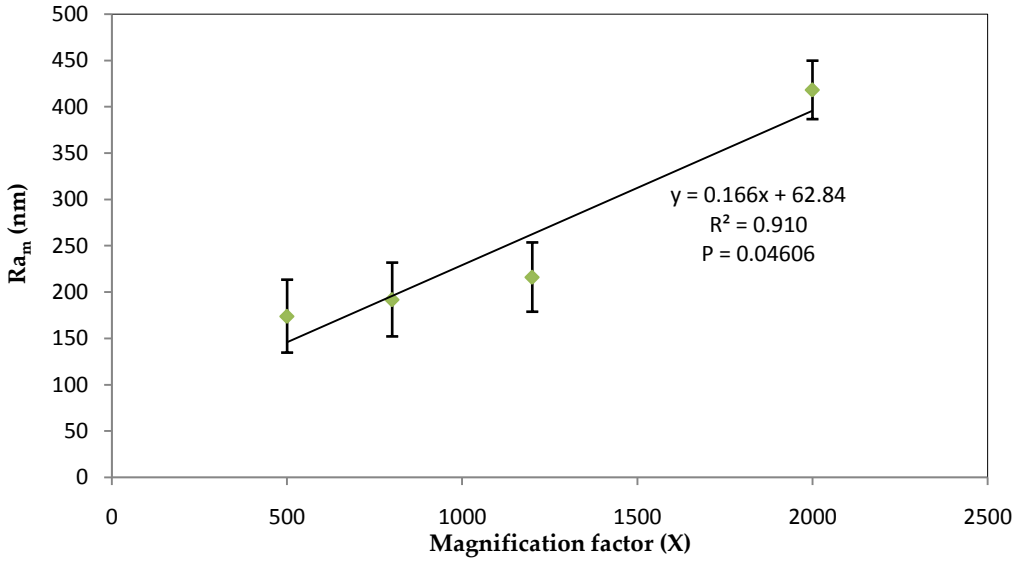

Figure 4.22. Plot of BHLC-3's mean roughness (Ra_m) against magnification factors. Error bars represent the standard deviation.

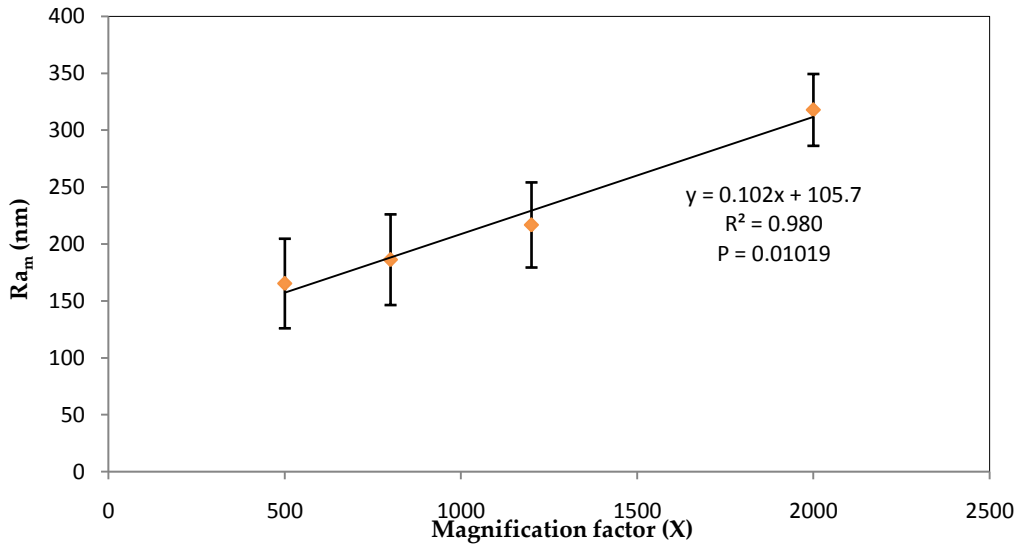

Figure 4.23. Plot of BHLC-4's mean roughness (Ra_m) against magnification factors. Error bars represent the standard deviation.

Table 4.5. Quantified values like slope, intercept at y axis and coefficient of determinants of the fitted lines of the linear regression from the above graphs are tabulated as m, c, R^2 and P respectively.

Sample No.	**Figure No.**	Slope of the curve	Intercept at *y* axis	Coefficient of determinants	Statistical significance
		m (+/-)	c (nm)	R^2	p value
BHLC-1	**4.20**	-0.077	226.1	0.883	0.06013
BHLC-2	**4.21**	+0.068	183.6	0.936	0.03217
BHLC-3	**4.22**	+0.166	62.84	0.910	0.04606
BHLC-4	**4.23**	+0.102	105.7	0.980	0.01019

The tabulated values of table 4.6 have been plotted in figures 4.24 and 4.25. Figure 4.24 shows the average of all samples roughness (Ra_M') for each magnification factor, although figure 4.25 does not take BHLC-1 into account. Figure 4.24 and 4.25 can be considered as master plots of the cartilage profile roughness. In figure 4.24 the relationship is not significant since $p>0.05$, but for figure 4.25 $p<0.05$ which is a significant relation. So, it clarifies inclusion of BHLC-1 increases the p value in figure 4.24 and vice-versa in figure 4.25. Comparing

these two plots, differences are tabulated in table 4.7. From table 4.7, we can determine the fitness of curve is much better for Ra_M' than compare to Ra_M, where the coefficients of determinants for Ra_M' is 0.977 and 0.770 for Ra_M. Beside R^2 values, the slope of two linear functions and standard deviations of each data points also infers the effect of BHLC-1. S_{Dev} at 2000× is ±133.4 nm for Ra_M and ±55.5 nm for Ra_M', so the error value of average of average roughness is large for Ra_M (where BHLC-1 is included).

Table 4.6. Mean profile roughness of all samples at their scanned magnification factor. Since, the variation of roughness in BHLC-1 is not as consistent as others; here I have tabulated two kinds of Ra_M and $Ra_{M'}$ including and excluding BHLC-1 respectively.

Including BHLC-1			**Excluding BHLC-1**		
Magnification factor (×)	**Mean of all Ra_m (nm)**	**Standard Deviation (±nm)**	**Magnification factor (×)**	**Mean of all Ra_m (nm)**	**Standard Deviation (±nm)**
	Ra_M	**S_{Dev}**		**$Ra_{M'}$**	**S_{Dev}**
500	181.36	33.44	500	184.30	40.83
800	200.12	35.1	800	203.49	40.37
1200	181.98	62.04	1200	238.65	39.35
2000	280.21	133.41	2000	349.85	55.52

After analyzing the profile surface roughness, the total surface roughness values were also computed. The total available surface area was taken into account (under the scanned aperture of the electron beam) to quantify the total surface roughness or S_a (see table 4.4). Figure 4.26 and 4.27 provides the complete picture of the mean total surface roughness analysis of the bovine humeral lateral condyle cartilage. The mean total surface roughness or Sa_M (figure 4.26) is the average out value of S_a (table 4.4) of all four samples of certain magnification factor and Sa_M' (figure 4.27) is the mean of three samples (excluding BHLC-1).

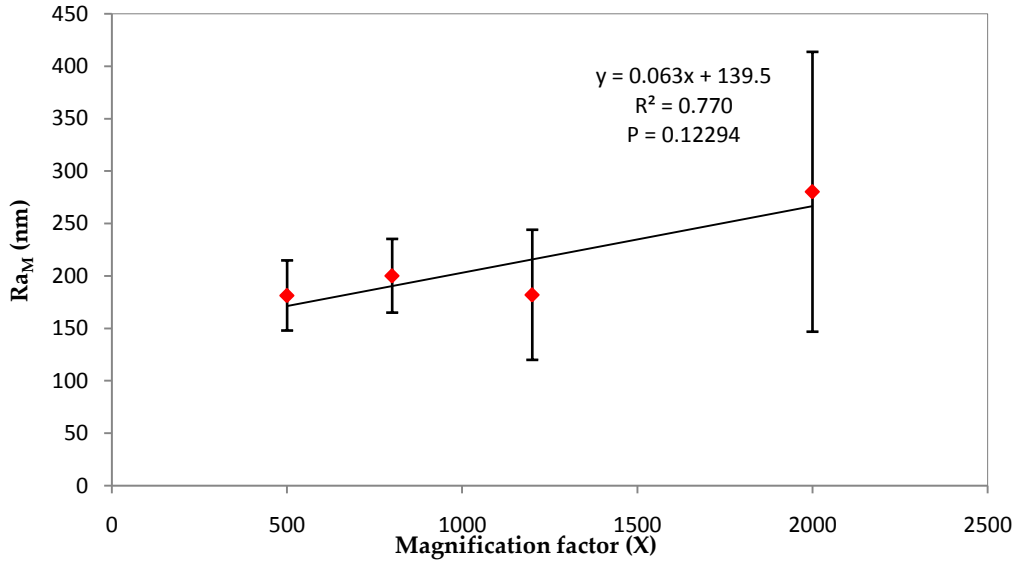

Figure 4.24. Plot of mean roughness for all samples (Ra_M) against magnification factors including all four samples. Here $p > 0.05$, it is not a significant relation. Error bars represent the standard deviation.

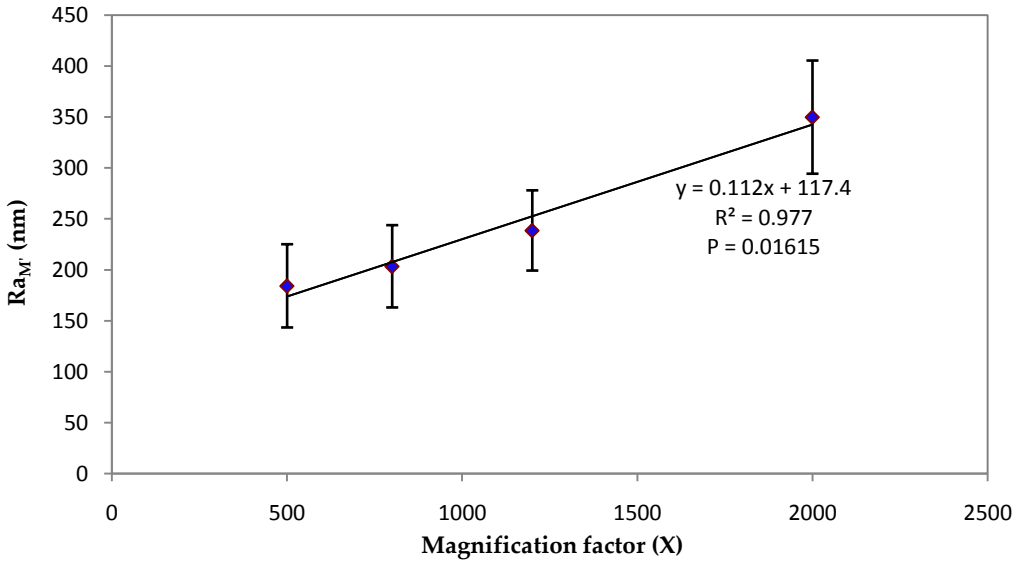

Figure 4.25. Plot of mean roughness for all samples ($Ra_{M'}$) against magnification factors excluding BHLC-1. Error bars represent the standard deviation.

Table 4.7. Comparison of fitted linear function's parameter for Ra_M and $Ra_{M'}$.

Sample Considered	Figure No.	Slope of the curve	Intercept at *y* axis	Coefficient of determinants	Statistical significance
		m (+/-)	c (nm)	R^2	p value
BHLC-1 – 4	39	+0.063	139.5	0.770	0.12294
BHLC-2 – 4	40	+0.112	117.4	0.977	0.01615

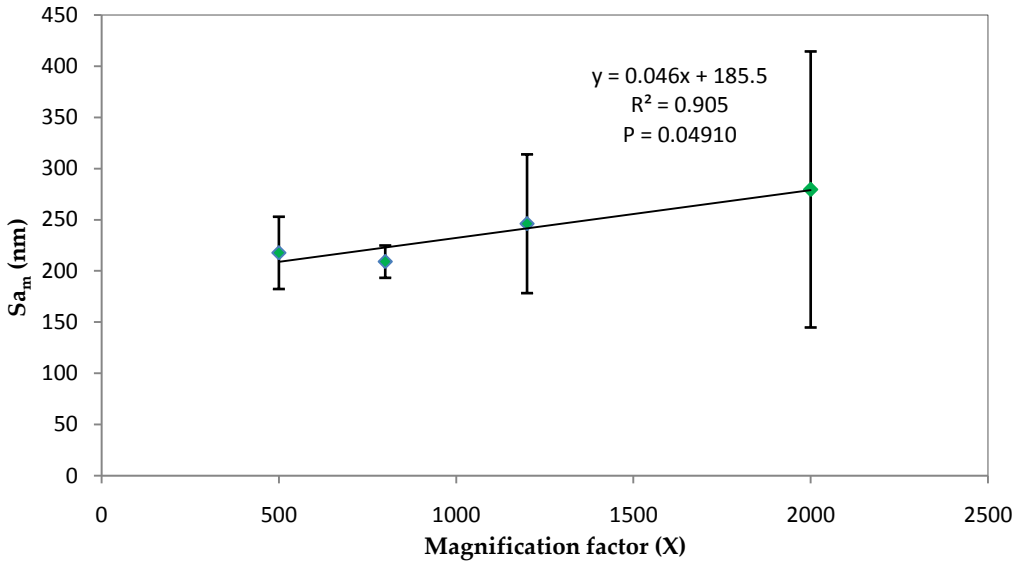

Figure 4.26. Plot of mean of total surface roughness (Sa_m) against magnification factor, considering all samples. Error bars represent the standard deviation.

Comparing figure 4.26 and 4.27, it is observed that the linear function for Sa_M values are a poorer fit than Sa_M', since the R^2 values for Sa_M and Sa_M' are 0.905 and 0.921, respectively. Beside the coefficient of determinant, the standard deviation values at maximum magnification factor is ±134.79 nm for Sa_M, but at the same factor of magnification the standard deviation of Sa_M' is much less i.e. ±46.72 nm.

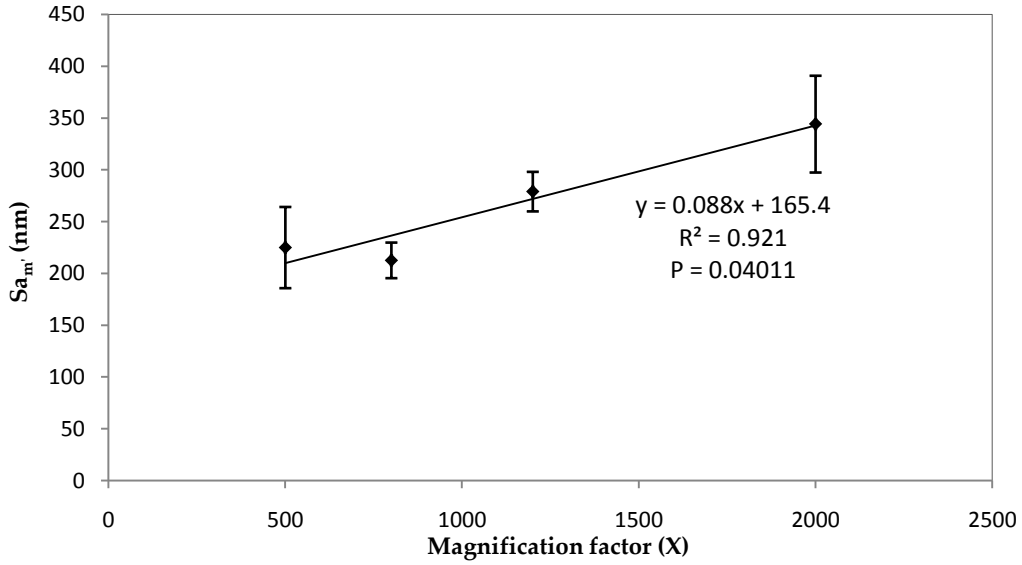

Figure 4.27. Plot of mean of total surface roughness (Sa_m) against magnification factor, excluding BHLC-1. Error bars represent the standard deviation.

4.2.3. Atomic Force Microscopy

After the 3D electron-topography, the phase modulated force topography of articular cartilage was undertaken and is presented in figure 4.28. The same cartilage surfaces (BHLC-1 - 4) that were used for electron microscopy were measured using AFM. The four profile roughnesses were denoted as R_{a1-4}. The mean of them has been denoted as R_{am} and the total surface roughness as S_a; obtained roughness values are tabulated in table 4.8. The range of roughness values was from about 78 to 114 nm.

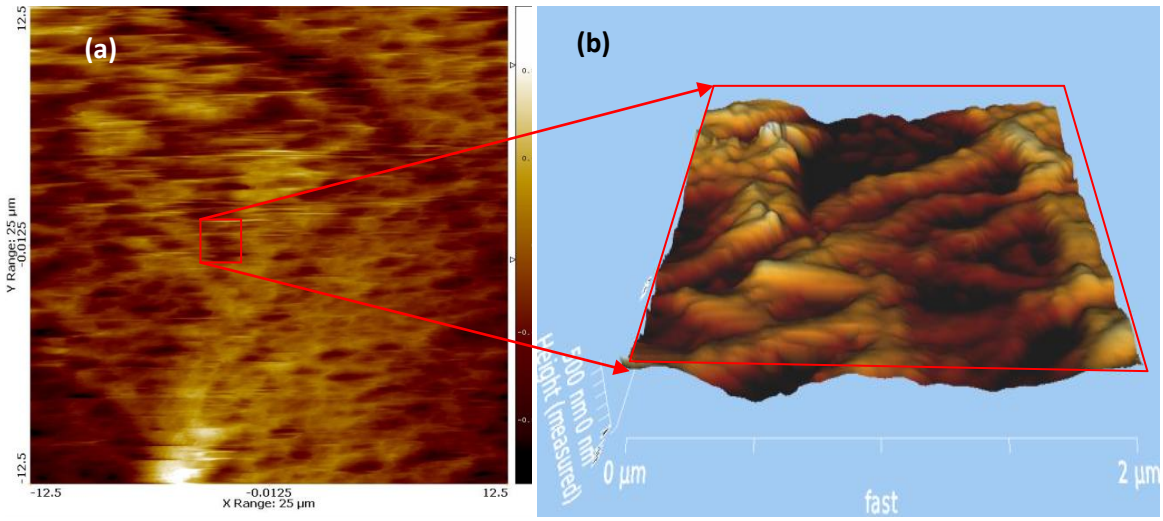

Figure 4.28. Shows phase plot topography of articular cartilage with atomic force microscopy. (a) The sample contains slight smearing effect, but at high resolution (b) it is not observed.

Table 4.8. Sample BHLC-1 – 4 is of bovine articular cartilage of humeral lateral condyle. Mean profile roughness or R_{am} and Total surface roughness or S_a has tabulated here.

Sample No.	Profile Roughness (nm)				Mean of profile roughness (nm)	Standard Deviation (± nm)	Total Surface Roughness (nm)
	R_{a1}	R_{a2}	R_{a3}	R_{a4}	R_{am}	S_{Dev}	S_a
BHLC-1	89.3	80.1	79.2	63.1	77.925	10.886	89.50
BHLC-2	169	133	80.6	74.8	114.350	44.862	136.0
BHLC-3	114	82.1	73.5	66.8	84.100	20.894	86.20
BHLC-4	85.1	87.2	81.0	76.9	82.550	4.563	89.10

4.2.4. COMPARISON OF 3D ELECTRON-TOPOGRAPHY AND AFM

The surface roughness values of articular cartilage obtained from three-dimensional electron-topography were compared with AFM roughness values obtained from the same sample. Initially, the mean profiles of each magnification factor are plotted against AFM mean profile roughness (figure 4.29 - 4.32). All of them are fitted with a linear correlation.

In ideal condition, where roughness obtained from 3D electron-topography matches that of the AFM, the points should have passed through a line of slope 1 that intercepts the origin. The green dashed line in all the plots are the ideal lines.

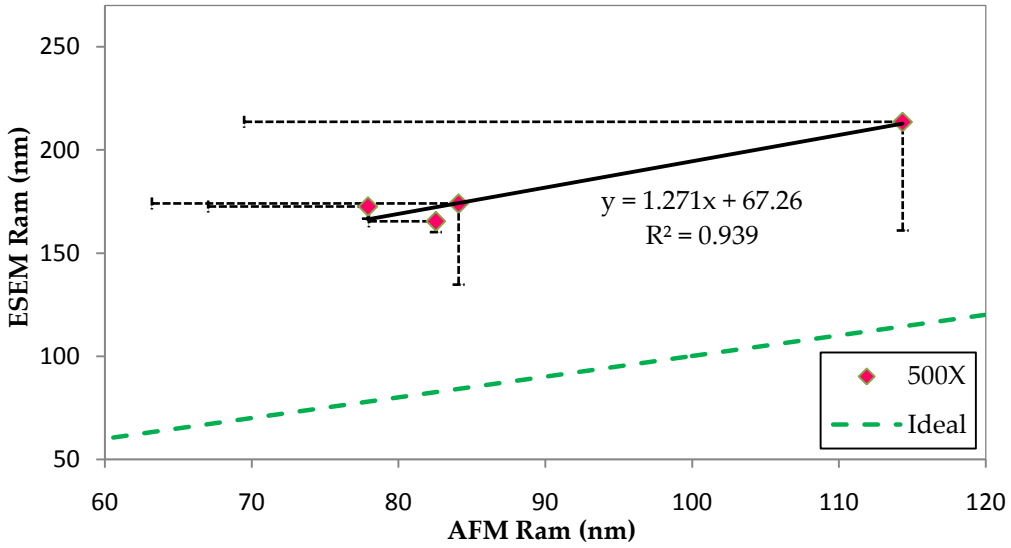

Figure 4.29. Plot of mean profile roughness (ESEM Ram) obtained from electron-topography at 500× against mean profile roughness obtained from AFM (AFM Ram). Error bars represent the standard deviation (towards positive as well)..

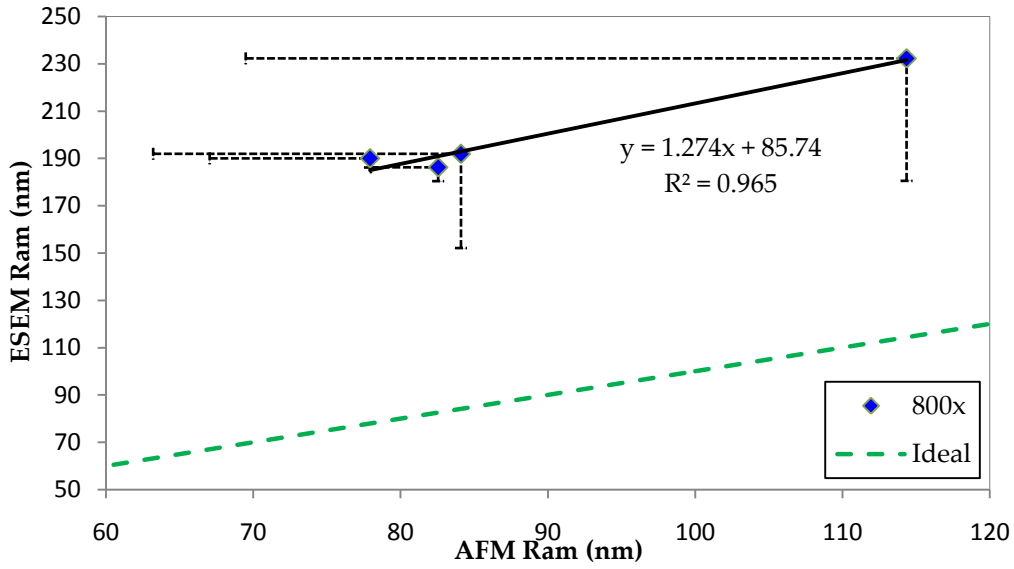

Figure 4.30. Plot of mean profile roughness (ESEM Ram) obtained from electron-topography at 800× against mean profile roughness obtained from AFM (AFM Ram). Error bars represent the standard deviation (towards positive as well)..

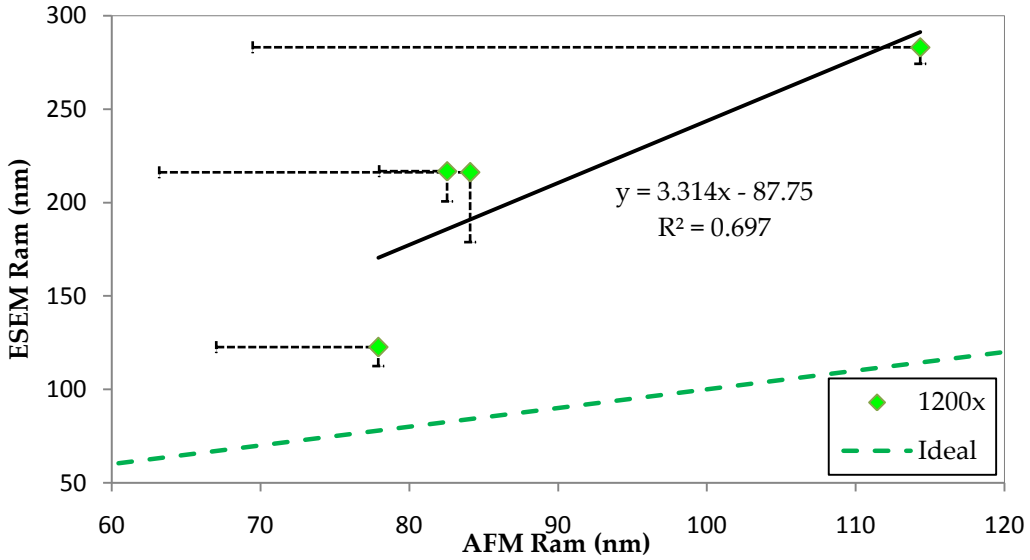

Figure 4.31. Plot of mean profile roughness (ESEM Ram) obtained from electron-topography at 1200× against mean profile roughness obtained from AFM (AFM Ram). Error bars represent the standard deviation (towards positive as well)..

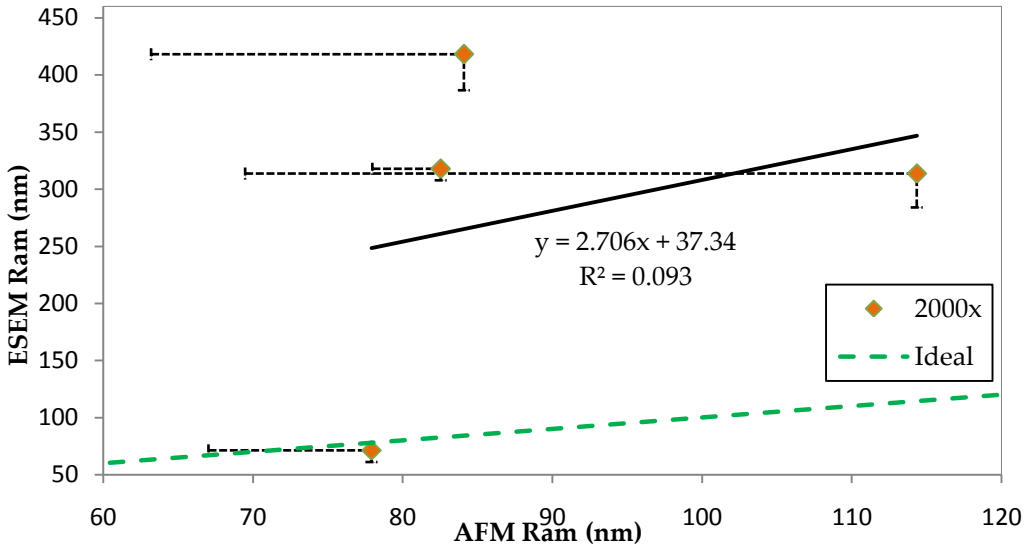

Figure 4.32. Plot of mean profile roughness (ESEM Ram) obtained from electron-topography at 2000× against mean profile roughness obtained from AFM (AFM Ram). Error bars represent the standard deviation (towards positive as well).

CHAPTER V
DISCUSSION

5.1. PDMS

The PDMS standard surface (used to determine the reliability of stereoscopic three-dimensional reconstruction at the nanoscale), was a sinusoidal surface as observed using SEM (figure 4.1). The three-dimensional reconstruction also produced a similar distribution (figure 4.2). Qualitatively, the PDMS surface was inferring that the approach can be employed as a noncontact technique for surface roughness characterization. To verify the 3D-ET method, AFM topography was also used and this produced a similar surface topography for the PDMS samples (figure 4.11). The period and amplitude of the sinusoidal profile were found to be 2 μm and 88 nm, respectively.

The datasheet of the standard surface states that, the roughness was around 35 nm, measured with a stylus of tip radius of 700 nm. After reconstruction the surface topography of eucentric SEM images, profile roughness and surface roughness values (arithmetic mean) were extracted from four different magnifications – 500×, 800×, 1200× and 2000×. With magnification factor the roughness is linearly varying (figure 4.3 - 4.8) from 52 nm to 611 nm. So, at low magnifications, the SEM technique gave surface roughness values closest to the measured standard sample. To arrive at a final conclusion I have plotted mean profile roughness of all six samples obtained at different magnifications against magnification factor. This master plot shows the same trend as the individual sample. The standard deviation of roughness at any particular magnification is very less, which supports the reliability of the technique.

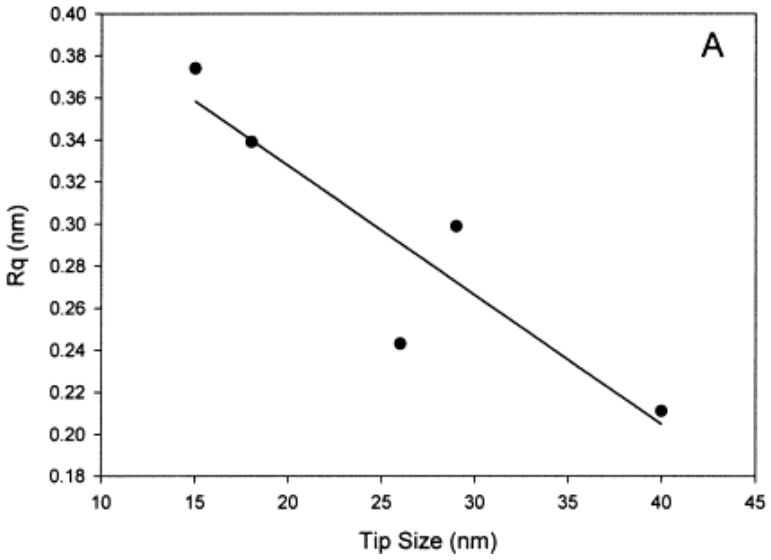

Figure 5.1. Image size of 500 nm was scanned with different AFM probe dimensions. The plot shows roughness as function of probe diameter. [*Sedin et al., 2001.* The License obtained from Elsevier to reuse the image].

Roughness increases with a decrease in the working length scale, which has been detailed by others [*Sedin et al., 2001*]. *Sedin et al. [2001] used a* quartz surface with an image size of 500 nm that was scanned with different diameter probes. As shown in figure 5.1, the roughness increases with decrease in working length scale. The literature has mentioned the roughness is a function of probe diameter.

The decrease in probe diameter is equivalent to a decrease in working length scale or increase in magnification factor. The results obtained by *Sedin et al.*, shows a similar trend to the results presented in this thesis. The same hypothesis works behind the roughness variation observed with an increase in magnification factor. As the magnification increases, the images show finer and finer features of the structure, so roughness naturally varies with different magnification factors (figure 5.2). In figure 5.2, we can see R_a at higher magnification increases due to the Δx factor which is due to the capture of fine features at high magnification. This ultimately integrates into the final value. Whereas, when we calibrate the same surfaces under AFM, consistently we get a roughness in the range of 25 to 29 nm. The reason is AFM does not have any variation of tip diameter; we had a single variable experiment. Entire samples were scanned with a tip diameter of 10 nm.

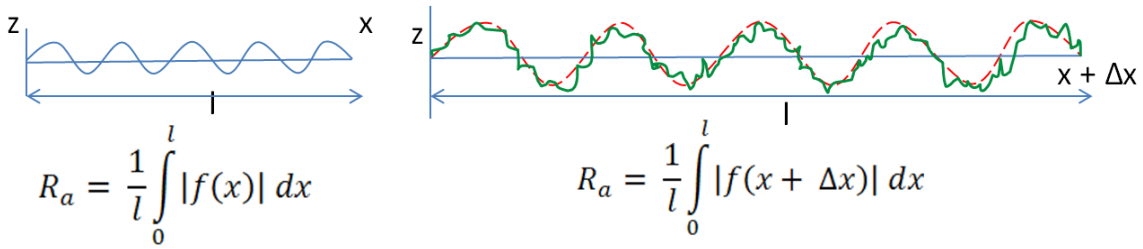

Figure 5.2. Concept of increment in roughness with magnification.

A comparative study was carried out with AFM and four different stereoscopic reconstructions magnifications (figure 4.12 – 4.15). The x axis is always constant since AFM was a single variable experiment. But the y axis is always incremental from figure 4.12 to 4.15 since the magnification was varying from 500× to 2000×. So, the roughness values at y axis were also varying. The slope value at 500× is close to 1. But for 800×, 1200× and 2000× it has increased to 3, 3.5 and 15, respectively. Although the curve is not well-fitted due to AFM being a single variable experiment [so quantile-qauntile of 3D-ET and AFM were plotted to determine whether the data populations are normally distributed or not - see appendix H] but an approximate calibration can be obtained. From this calibration

a linear equation can be derived, so that one can quantify a single value of roughness, if only measured with stereoscopic SEM reconstruction.

$$R_{am}^{ESEM} = a.R_{am}^{AFM} + b \qquad Eqn.5.1$$

Where, R_{am}^{ESEM} is the obtained arithmetic mean value from stereoscopy and R_{am}^{AFM} can be considered as single value of roughness. Constant a and b can be determined from our comparative plot of stereoscopy and AFM (figure 4.12-4.15). This calibration should help to determine the roughness by taking into account of a correction factor.

5.2. ARTICULAR CARTILAGE

The superficial surface of articular cartilage is highly inhomogeneous and contains basically collagen fibers in different patterns (figure 4.17) and some porous features started appearing from 252× of magnification which could affect the ultimate roughness of cartilage surface. These features were nearly 5 – 10 μm in dimension (figure 5.3). After getting confidence with the standard roughness surface of PDMS, these cartilage surfaces were three-dimensionally reconstructed from SEM images (figure 4.19).

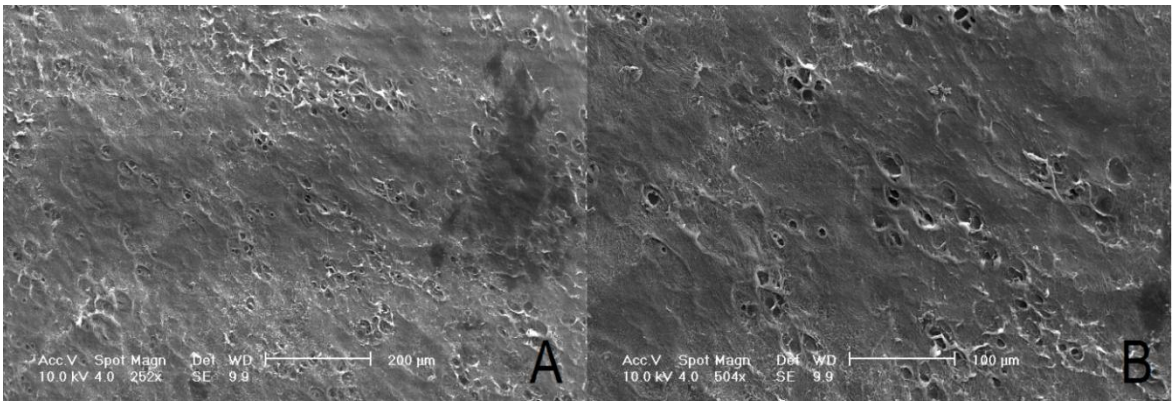

Figure 5.3. Porous features on the superficial surface of articular cartilage.

Like PDMS, articular cartilage surface roughness values were also characterized at magnifications of 500×, 800×, 1200× and 2000× for four different samples. These roughnesses were similarly plotted against their corresponding

magnification factor. The trends of them are also linearly increasing (excluding BHLC-1). I suspect that sample BHLC-1 was affected possibly with typical stereopsis error as mention in background, so providing an out of trend variation from the other samples. The roughness variation shows at table 4.4 that at 1200× and 2000× the profile has become over-flattened. These two points are affecting the sample. Beside stereopsis error digital subtraction of unnecessary background level may also leads over-flattening the profile particular at these two magnifications.

Now when the reconstruction error is encountered a small systemic experiment was designed. In which the major source of typical stereopsis error was determined. Unlike the homogeneous PDMS surface, capturing eucetric images at high magnification for inhomogeneous cartilage is difficult. This is because of the uncontrolled manual stage actuation. It was probably affecting BHLC-1 at two particular above mentioned magnification factors. BHLC-1 only demonstrates negative slope (figure 4.20), whereas the other samples consistently produced positive slopes of 0.06 to 0.1 (figure 4.21 - 4.23). When we exclude this particular sample (BHLC-1) for global analysis, a similar trend was obtained to PDMS samples (figure 4.25 and 4.27). When sample BHLC-1 is included for the mean global analysis we end up with very high standard deviation (figure 4.26 and 4.28) and statistically insignificant p values around 0.122 and 0.05.

Beside this stereoscopic analysis AFM topography produces consistent roughness values ranging from 77 to 114 nm. I presume since our minimum feature on the cartilage surface was 20 nm i.e. of collagen fibers, the AFM tip of 10 nm would be sufficient. Like PDMS, AFM studies for cartilage were also carried out with a single tip. Due to this a comparative analysis between SEM stereoscopy and AFM the x axis or the AFM roughness axis is always constant. It observed that the slope at 500× and 800× is nearly 1 and parallel to the ideal line (figure 4.29 and 4.30), but as I increase the magnification the slope increases. The Eqn. 5.1 also

holds for cartilage, from which we can determine the roughness for bovine humeral lateral condyle articular cartilage is in the range 70 - 120 nm.

As I have discussed in chapter II about the molecular adhesion and stick-slip problems, the same evidence still exist for us although PM-AFM was used and in theory it should provide indifferent topography. But figure 5.4 shows one of the examples which we have come across, where this phenomenon is strongly present. The maximum amplitude of the profile is more than 1.6 µm. These peak values are contradictory for a surface like cartilage. The black encircled region of figure 5.4.B is one of the peaks which is artificial and generated due to the molecular adhesion between the probe and the surface. These kind of peaks are everywhere in the same image. The topography shown by the red circle in figure 5.4.A and B are proof of stick-slip.

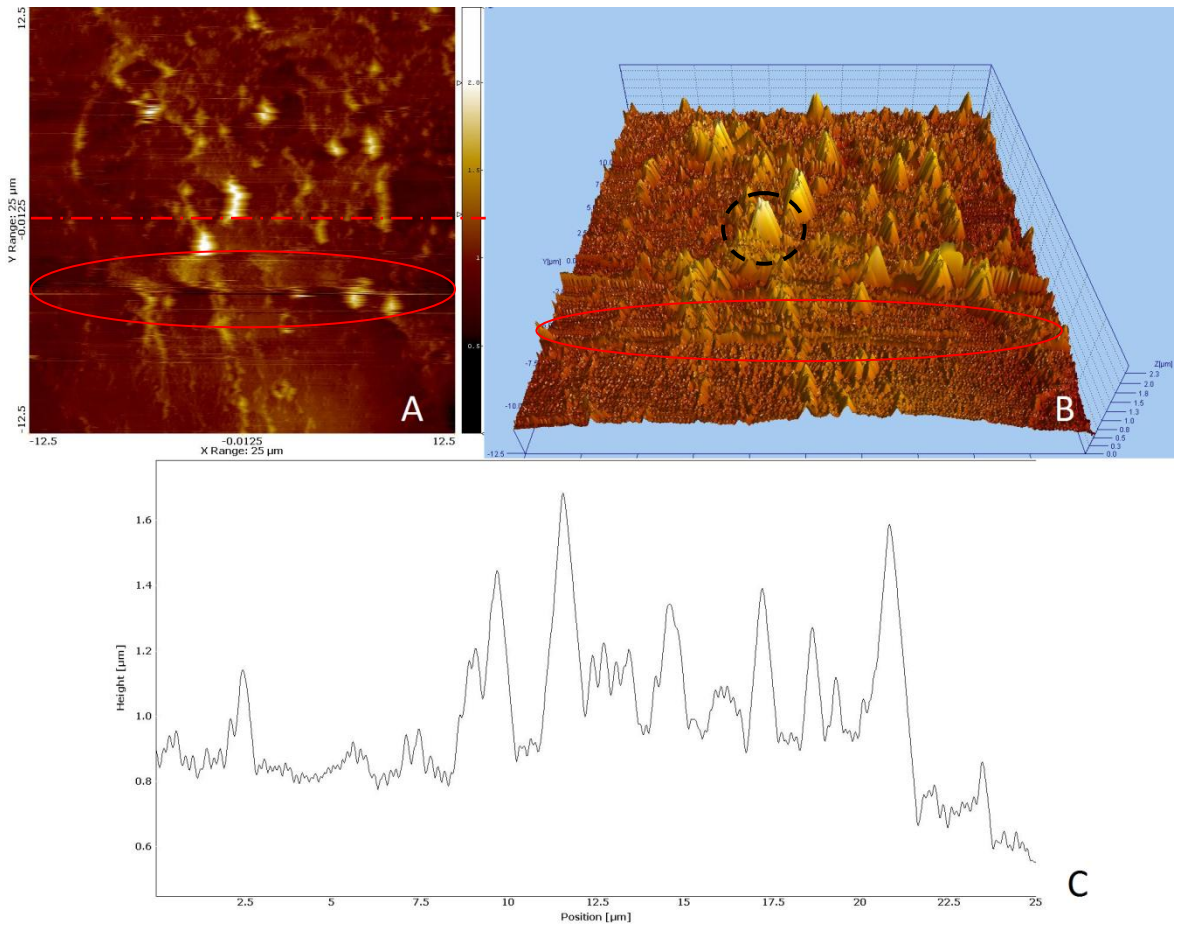

Figure 5.4. A and B are surface topography obtained with phase modulation. The surface shows presence of molecular adhesion and stick-slip problem. C shows the profile of the red line of A

This is to mention that PM-AFM - considered as non-contact force microscopy was very hard to generate the original topography. The reproducibility of a same topography was very difficult. With combination of force mapping and PM-AFM I have managed to characterise and calibrate the surface of articular cartilage. But the technique is not at all high throughput. A 25 μm × 25 μm surface imaging used to take more than 12 hours.

Coming back to 3D-ET and its problem, it was encountered that unwanted debris leads to an increase in surface roughness. So, I have always avoided imaging surfaces with contamination and debris. Another problem is capturing eucentric images at high magnification, which I aim to recover in the near future with a digitally actuated SEM stage. Less precision due to manual actuation sometimes affected our reconstruction. Therefore, I did imaging with differential angle of not more than ± Δ5°. Our future aim is to rectify these two problems to utilise this efficient technique to characterise articular cartilage. Appendix F enlightens on some of the typical issues of 3D-ET, which were mentioned in the background (chapter II- section 2.5).

Surface characterisation of articular cartilage with noncontact 3D electron-topography provides much better result compare to earlier literature and our present evidence of AFM. The technique of 3D-ET used here has not been used in earlier literature to quantify the surface roughness or characterization for cartilage. It was discussed in the background (chapter II - section 2.2) that earlier attempt with Laser Profilometer determined a roughness value of ~800 nm (±200 nm) [*Forster, 1999*]. The standard deviation suggests that it may not be a reliable technique for small-scale roughness characterization. A few studies on Optical Coherence Tomography and Ultrasound imaging have reported that surface roughness of articular cartilage of human patient is nearly ~8000 nm and ~9000 nm respectively [*Saarakkala et al., 2009; Saarakkala et al., 2004*]. In recent year [2011], using optical coherence tomography Saarakkala *et al.,* claimed the roughness of

healthy and degraded bovine articular cartilage are 2500 nm (±700 nm) and 18500 nm (±4200 nm). There are several studies on Ultrasound imaging for roughness quantification [*Chiang et al., 1996; Kaleva et al., 2009; Wang et al., 2009*]. But the roughness obtained is similar to above mentioned. On the contrary, atomic force microscopy (AFM) showed surface roughnesses of 72±23 nm and 65±24 nm for fresh and frozen *Bovine* cartilage samples, respectively for local Ra and for global (100 μm × 100 μm area) Sa it was 450±237 nm for fresh samples and 495±189 nm for frozen samples [*Moa-Anderson et al., 2003*]. Lately, Park *et al., [2011]* has also found a value (462±216 nm) to that of Moa-Anderson *et al., [2003]* with AFM. But still the standard deviation is not appreciable. The scanning contains artifacts of stick-slip and molecular-dragging [figure 5.5], these certainly affect the total roughness mentioned. The values are not verified with high-resolution AFM topography like figure 4.11. AFM results vary with tip diameter, contact force and deformation of surface. It can provide an idea rather than a perfect standard value. The resolutions of any of these methods are merely closer to electron microscopy; any optical method is limited by the wavelength of the light.

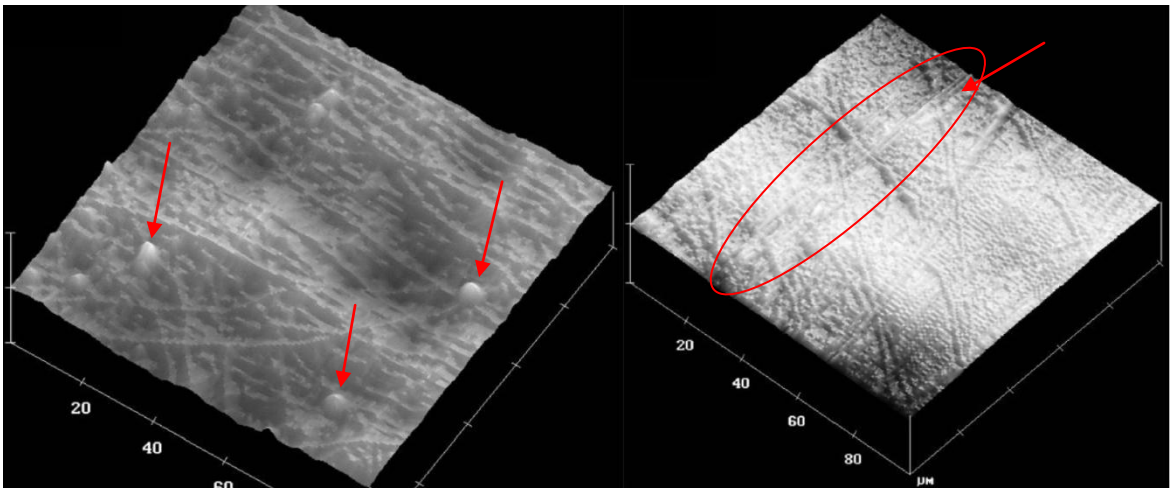

Figure 5.5. Both the surfaces of bovine articular cartilage contain slip-stick (red arrow) and molecular dragging evidence (red encircled region) *[Park et al., 2011]* [Permission taken from the corresponding author - Prof. Gerard A. Ateshian, Columbia University].

The roughness obtained with any optical measurement and ultrasound in the above paragraph always determines roughness for global surface area due to

their limited precision, where global peaks and valleys are coming into account. That is the reason for Saarakkala *et al., [2011]* is getting such a large roughness values. The degraded cartilage roughness values infer that the method is considering the large peaks and valleys of global distribution. If this is the case then accuracy at the small-scale is neglected. To be precise, a local analysis of very small-scale (at least nanoscale) surface roughness is needed to produce accurate and better surface of replacement material. Scanning electron microscopy is generally used for nanoscale qualitative surface morphology analysis. But, this well-established qualitative technique was used here towards quantitative analysis of surface roughness. Verification with respect to standard surface provided us with the confidence to pursue this technique. The roughness analysis used here was mainly considered the local distribution. The ranges found (if BHLC-1 is excluded) here with 3D-ET was 165 nm to 418 nm with a smaller standard deviation compare to the earlier literature.

The thesis shows a path of utilising stereoscopy at the nanoscale, which should be a breakthrough for cartilage surface characterisation with a pure non-contact method. Using an electron beam enables high resolution imaging, unlike optical resolution. So, performing surface roughness extraction should provide highly accurate quantification. Roughness characterisation of inhomogeneous articular cartilage surface was the primary goal which will lead us to artificial replacement for articular cartilage with the optimum surface features for the required tribological performance. This thesis provides not only an analysis of surface roughness characterisation of articular cartilage, but also offers a detail philosophy of 3D-ET with respect to magnification. Over the range of magnifications based on which the experiments were designed, it was observed within this range roughness is more or less linearly variable with magnification. Now it depends on the medical practitioners and biomedical engineers to determine which magnification they should work on. Even if they are confused

whether to work at very high magnification or less, our derived calibration with AFM should help to determine a single roughness. The detail analysis mentioned in the thesis should contribute a good impact to mimic the articular cartilage artificially and testing them in real-time.

The research presented in this thesis shows a path and a philosophy of articular cartilage roughness characterisation. A constant surface's texture keeps varying with working length scale. So mentioning roughness alone does not provide the complete picture unless working length scale is mentioned. Research questions comes into platform for any natural material that is, at what particular working length biomedical engineering should stay tuned! Is there truly a particular working length scale? To answer that, in future the research should be carried out considering a broad range of working length scale for tribological analysis.

5.3. CONCLUSIONS

The main conclusions of this thesis are:

1) Using 3D-ET roughness was found to increase with magnification irrespective of any material.

2) Using 3D-ET cartilage roughness was found to be in the order of 165 nm to 418 nm. The appreciable standard deviation provide its reliability.

3) Using AFM cartilage roughness was found to be in the order of 77 nm to 114 nm. Roughness obtained from AFM is not a high-throughput approach due to combining force mapping and phase-modulation mode.

4) Analysis of roughness with respect to magnification (for the range of working length scale considered here) entails, roughness is a function of magnification, which is linear.

5) Verifying 3D-ET with standard surface and comparing 3D-ET with AFM provide a way for roughness correction.

Parts of the thesis are published in:

S Ghosh, J Bowen, K Jiang, D M Espino and D E T Shepherd. Investigation of techniques for the measurement of articular cartilage surface roughness. *Micron* (in press corrected proof) (http://dx.doi.org/10.1016/j.micron.2012.06.007)

S Ghosh, D E T Shepherd and K Jiang. Preliminary investigation of surface characteristics of articular cartilage with 3-d tomography. IEEE 2011 International Conference on Nanoscience, Technology and Societal Implications (NSTSI). (http://dx.doi.org/10.1109/NSTSI.2011.6111998)

REFERENCES

MeX Alicona. MeX Manual for MeX 5.0.1 EN 01.02.2008. Alicona Imaging GmbH, 2008.

G A Ateshian. Artifical cartilage: Weaving in three dimensions. Nature Materials, 2007;6:89-90.

T Bayes and R Price. An Essay towards solving a problem in the Doctrine of Chance. Philosophical Transactions of the Royal Society of London, 1763;53:370–418.

P N Belhumeur and D Mumford. A Bayesian treatment of the stereo correspondence Problem Using Half-Occluded Regions. 1992;IEEE 3/92: 506–512.

P N Belhumeur. A Bayesian approach to binocular vision stereopsis. International Journal of Computer Vision, 1996;19:237-260.

L A Bendersky and F W Gayle. Electron diffraction using transmission electron microscopy. Journal of Research of the National Institute of Standards and Technology, 2001;106:997–1012.

B Bloch and L Dintenfass. Rheological study of human synovial fluid. Journal of Surgery. 1963:33;108–113.

S P M Bohari. Effect of ultrasound on production of extracellular matrix by cells in culture. PhD thesis submitted to University of Birmingham, Birmingham, UK, 2011.

G Binning, C F Quate, C Gerber. Atomic force microscope. Physical Review Letter, 1986;56:930.

L de Broglie. Waves and Quanta. Nature, 1923;112:540.

C Canale, B Torre, D Ricci and P C Braga. Recognizing and avoiding artifacts in atomic force microscopy imaging. Methods of Molecular Biology, 2011;736:31-43.

R W Carpick and M Salmeron. Scratching the surface: Fundamental investigations of tribology with atomic force microscopy. Chemical Review, 1997;4:1163.

F H Chen, K T Rousche and R S Tuan. Technology Insight: adult stem cells in cartilage regeneration and tissue engineering. Nature Reviews Rheumatology, 2006;2:373-382.

E H Chiang, R S Adler, C R. Meyer, J M. Rubin, D K Dedrick and T J Laing. Quantitative assessment of surface roughness using backscattered ultrasound: The effects of finite surface curvature. Ultrasound in Medicine & Biology, 1994;20:123-135.

Department for Environment Food and Rural Affairs. UK Slaughter statistics. Published by DEFRA, February, 2012.

A Einstein. On the theory of light production and light absorption. Annalen der Physikser, 1906;20:199–206.

R Feynman, R Leighton, and M Sands. The Feynman lectures on physics: Volume 1. Addison-Wesley, Boston, USA, 1964.

H Forster and J Fisher. The influence of continuous sliding and subsequent surface wear on the friction of articular cartilage. Proceedings of Institution of Mechanical Engineers. Part H Journal Engineering in Medicine, 1999:213;329–345.

T Fukuma, J I Kilpatrick and S P Jarvis. Phase modulation atomic force microscope with true atomic resolution. Review of Scientific Instruments, 2006;77: 123703-1-5.

J Goldstein, D E Newbury, D C Joy, C E Lyman, P Echlin, E Lifshin, L Sawyer and J R Michael. Scanning Electron Microscopy and X-ray Microanalysis. 3rd Edition, Springer, Berlin, Germany, 2003.

A P Gwynn, S Wade, M J Kääb, G R Owen and R G Richards. Freeze-substitution of rabbit tibial articular cartilage reveals that radial zone collagen fibres are tubules. Journal of Microscopy, 2001;197:159-172.

P K Hansma, J P Cleveland, M Radmacher, D A Walters, P E Hillner, M Bezanilla, M Fritz, D Vie, H G Hansma, C B Prater, J Massie, L Fukunaga, J Gurley and V Elings. Tapping mode atomic force microscopy in liquids. Applied Physics Letter, 1994;64:1738-40.

Health and Safety Unit. Health and Safety Policy. UHSP/0/10, University of Birmingham, Birmingham, UK

R Howland and L Benatar. A practical guide to scanning probe microscopy. ThermoMicroscopes (Presently Veeco Instruments Inc. New York, USA), 1997.

S Hisakazu, M Mizunuma, M Nishida, M Inoue, M Inoue and I Masahiro. 3D-CT Stereoscopic Imaging in Maxillofacial. Journal of Computer Assisted Tomography, 1999;23:276-279.

Y Huang, S Saarakkala, J Toyras, L Wang, J S Jurvelin and Y-P Zheng. Effects of optical beam angle on quantitative optical coherence tomography (OCT) in normal and surface degenerated bovine articular cartilage. Physics in Medicine and Biology, 2011;56:491.

M Huber, S Trattni and F Lintner. Anatomy, biochemistry, and physiology of articular cartilage. Investigative Radiology. 2000:35; 573-580.

B Julesz. Foundations of cyclopean perception. University of Chicago press, Chicago, USA, 1971, Now at MIT Press, Cambridge, Massachusetts, USA, 2006.

E Kaleva, S Saarakkala, J S Jurvelin, T Virén and J Töyräs. Effects of ultrasound beam angle and surface roughness on the quantitative ultrasound parameters of articular cartilage. Ultrasound in Medicine & Biology, 2009;35:1344-1351.

M J Kääb, G Richards, P Walther, J ap Gwynn and H Nötzli. A comparison of four preparation methods for the morphological study of articular cartilage for Scanning Electron Microscopy. Scanning Microscopy, 1999;13:61-69.

M A Lantz, S J O'Shea, A C F Hoole and M E Welland. Lateral stiffness of the tip and tip-sample contact in frictional force microscopy. Applied Physics Letter, 1997;70:970-2.

D Marr and T Poggio. A computational theory of human stereo vision. Proceedings of Royal Society of London, 1979;204:301-328.

A Maroudas. Physicochemical properties of articular cartilage. Adult Articular Cartilage, 1979; 215–290.

A Maroudas and C Bannon. Measurement of swelling pressure in cartilage and comparison with the osmotic pressure of constituent proteoglycans. Biorheology. 1981:18;619–632.

A Maroudas, J Mizrahi, E P Katz, E J Wachtel and M Soudry. Physicochemical properties and functional behavior of normal and osteoarthritic human cartilage. Articular Cartilage Biochemistry. 1986:311–329.

C M Mate, G M McClelland, R Erlandsson and S Chiang. Atomic-scale friction of a tungsten tip on a graphite surface. Physical Review Letter, 1987;59:1942-45.

S N Medyanik, W K Liu, In-Ha Sung and R W Carpick. Predictions and observations of multiple slip modes in atomic-scale friction. Physical Review Letter, 2006;97:136106-1-4.

B J Moa-Anderson, K D Costa, C T Hung and G A Ateshian. Bovine articular cartilage surface topography and roughness in fresh versus frozen tissue samples using atomic force microscopy. Summer Bioengineering Conference, Sonesta Beach Resort in Key Biscayne, Florida, 2003.

V C Mow, M H Holmes and W Michael Lai. Fluid transport and mechanical properties of articular cartilage: A review. Journal of Biomechanics. 1984:17;377–394.

V C Mow and A Ratcliffe. Structure and function of articular cartilage and meniscus. Basic Orthopedic Biomechanics. 1997:113–178.

S Park, K D Costa and G A Ateshian. Microscale frictional response of bovine articular cartilage from atomic force microscopy. Journal of Biomechanics, 2004:37;1679-1687.

J R Parsons and J Black. The viscoelastic shear behavior of normal rabbit articular cartilage. Journal of Biomechanics, 1977:10;21-29.

K Przibram. Letters on wave mechanics: Schrödinger, Planck, Einstein, Lorentz. Philosophical library, New York, USA, 1967

C Y. Poon and B Bhushan. Comparison of surface roughness measurements by stylus profiler, AFM and non-contact optical profiler. Journal of Wear, 1995;190:76–88.

T Pylios and D E T Shepherd. Soft layered concept in the design of metacarpophalangeal joint replacement implants. Bio-medical Materials and Engineering, 2008;18:73-82.

V S Ramachandran. Perception of shape from shading. Nature, 1988;331:163-166.

E L Radin, I L Paul and Martin Lowy. A comparison of dynamic force transmitting properties of subcondral bone and articular cartilage. Journal of bone and Joint Surgery. 1970:52;444-456.

T Räsänen and K Messner. Regional variations of indentation stiffness and thickness of normal rabbit knee articular cartilage. Journal of Biomedical Materials Research. 1996:31;519–524.

S Saarakkala, J Toyras, J Hirvonen, M S Laasanen, R Lappalainen and J S Jurvelin. Ultrasonic quantitation of superficial degradation of articular cartilage. Ultrasound Medical Biology, 2004:30; 783–789.

S Saarakkala, S-Z Wang, Y-P Huang and Y-P Zhen. Quantification of the optical surface reflection and surface roughness of articular cartilage using optical coherence tomography. Physical Medical Biology. 2009:54;6837–685.

M B Schmidt, Van C Mow, Lawrence E. Chun, David R. Eyre. Effects of proteoglycan extraction on the tensile behavior of articular cartilage. Journal of Orthopaedic Research. 1990:8;353-363.

K Sebastian, K Matthias and S Thomas. Stereoscopic 3D from 2D video with super-resolution capability. Journal of Signal Processing: Image Communication, 2008;23:665-676.

D L Sedin and K L Rowlen. Influence of tip size on AFM roughness measurements. Applied Surface Science, 2001;182: 40-48.

G Selvaduray. Surface Roughness. Lecture notes on Methods in Materials Engineering, San Jose State University, Department of Chemical Engineering 2002. [http://www.sjsu.edu/faculty/selvaduray/page/papers/mate210/surface.pdf]

L A Setton, Van C Mow and D S Howell. Mechanical behavior of articular cartilage in shear is altered by transection of the anterior cruciate ligament. Journal of Orthopaedic Research. 1995:13;473–482.

D E T Shepherd. Joint Replacement Implants. Chapter 8 in Biomechanics of Hard Tissues: Modeling, Testing, and Materials (eds A. Öchsner and W. Ahmed), Wiley-VCH Verlag GmbH, 2010.

D E T Shepherd and G Azangwe. Synthetic versus tissue-engineered implants for joint replacement. Applied Bionics and Biomechanics, 2008;4:179-185.

D E T Shepherd and B B Seedhom. A technique for measuring the compressive modulus of articular cartilage under physiological loading rates with preliminary results. Proceedings of Institution of Mechanical Engineers, Part H: Journal of Engineering in Medicine, 1997;211:155-165.

D E T Shepherd and B B Seedhom. The 'instantaneous' compressive modulus of human articular cartilage in joints of the lower limb. Rheumatology, 1999;38:124-132.

N Shepherd and M Mitchell. The localization of articular cartilage proteoglycan by electron microscopy. The Anatomical Record, 1977;187:463-475.

D Spiegelhalter and K Rice. Bayesian statistics. Scholarpedia, 2009;4(8):5230.

R A Stockwell. Biology of Articular Cartilage. 1979, Cambridge University Press, Cambridge, UK.

A C Swann and B. Seedhom. The stiffness of normal articular cartilage and the predominant acting stress levels: implications for the aetiology of osteoarthrosis. Rheumatology. 1991;32:16-25.

J S Temenoff and A G Mikos. Review: tissue engineering for regeneration of articular cartilage. Biomaterials, 2000;21:431-440.

E Ukraintsev, A Kromka, H Kozak, Z Remeš and B.Rezek. Artifacts in Atomic Force Microscopy of Biological Samples. Atomic Force Microscopy Investigations into Biology - From Cell to Protein. Chapter 2:29-54, InTech Publication, Croatia, Rijeka, 2012.

J P G A Urban, A Maroudas, M T Bayliss and J Dillon. Swelling pressures of proteoglycans at the concentrations found in cartilaginous tissues. Biorheology. 1979:16;447–464.

U Vazirani. Planck-Einstein relation, Time Dependent Schrodinger Eq., Position Momentum representation and deBroglie Relation. Lecture 7 of Qubits, Quantum Mechanics, and Computers, University of California, Berkeley, 2003.

S Wang, Y Huang, S Saarakkal and Y-P Zheng. Quantitative Assessment of Articular Cartilage with Morphologic, Acoustic and Mechanical Properties Obtained Using High-Frequency Ultrasound Original Research Article. Ultrasound in Medicine & Biology, 2010;36: 512- 527.

M Williams. Snow hydrology (Geog 4321): skiing at the triple point. University of Colorado, Boulder, 2007.

M Xu, D Fujita, K Onishi and K Miyazawa. Improving accuracy of sample surface topography by atomic force microscopy. Journal of Nanoscience and Nanotechnology, 2009;10:6003-7.

N Yao, Z L Wang. Handbook of Microscopy for Nanotechnology. Kluwer Academic Publishers, New York, USA, 2005.

Q Zhong and D Inniss. Fractured polymer/silica fiber surface studied by tapping mode atomic force microscopy. Surface Science Letter, 1993;290:L688-692.

APPENDIX

APPENDIX A: DATASHEET OF STANDARD ROUGHNESS

Rubert + Co Ltd
the home of surface measurement

Rubert + Co Ltd
Acru Works, Demmings Road, Cheadle SK8-2PG, England
Tel: (44)-0161-428-6058 Fax: (44)-0161-428-1146
email: info@rubert.co.uk
website: www.rubert.co.uk

certificate #41172

REPORT OF ROUGHNESS MEASUREMENTS

for sinusoidal roughness master standard type 543E

Measurement	date:	1.04.2011
	equipment used:	Talystep Mk 1
		TStep #4, stylus tip 0.7 μm
Object measured	specimen type:	543E sinusoidal
	serial number:	P1
	manufacturer:	Rubert

Measuring conditions

vertical magnification Mv = 100 000
horizontal speed = 0.3 mm / min
datapoint spacing = 0.009 μm
filter Gaussian, cutoffs λc = 0.025 mm, λs = zero
traverse length = 5 λc = 0.126 mm

calibration

the instrument was first calibrated on a certified stepheight of 91.3 nm ± 1.5 nm resulting in a vertical calibration factor of 0.974802

measuring plan

12 profiles were taken in 3 lines of 4 each, spaced diagonally evenly over the measuring area, and for each profile Ra and Rz were evaluated in accordance with ISO 4287.

Results for 543E-P1

Ra (nm) n = 12
mean = 35.48 nm
standard deviation = 0.250 nm

Rz (nm) n = 12
mean = 126.08 nm
standard deviation = 4.274 nm

Uncertainty

U(Ra) = 0.670 nm

U(Rz) = 10.7 nm

The certified parameter values, with expanded uncertainties for a coverage factor of k = 2, are therefore:

Ra = 35.48 nm ± 1.2 nm

Rz = 126.1 nm ± 21.4 nm

signed . . . . . .

date 16-06-2011

APPENDIX B: PREPARATION OF PHOSPHATE BUFFER AND FIXATIVES

Process: Phosphate buffer and fixative preparation

Application: To maintain physiological pH *in vitro.*

Principle: Inhibition to change pH by reaching chemical equilibrium between the acid and its conjugate base. The basic chemical equilibrium $K_a = [H^+][A^-]/[HA]$ where $HA = H^+ + A^-$ and HA is the acid and A^- is the conjugate base.

Protocol for phosphate buffer:

1. Prepare disodium hydrogen phosphate (Sigma Aldrich, Missouri, USA) of 0.1 M, hydrochloride acid (Fisher Scientific, Leicestershire, UK) of 0.1 M and sodium hydroxide of 0.1 M (Merck KGaA, Darmstadt, Germany).
2. To obtain pH 7 mix 756 ml of disodium hydrogen phosphate of 0.1 M and 244 ml of 0.1 M hydrochloride acid and check pH (with pH meter), add sodium hydroxide until it reaches pH 7.
3. Store it at 4°C non-reactive beaker.

***Protocol for fixative preparation*:**

1. Add 16 g of paraformaldehyde (Sigma Aldrich, Missouri, USA) to 100 ml of DI water. Then heat exactly at 60°C along with few drops of 1M NaOH until the solution get clear. Allow it to cool.
2. Then 5 ml of 25% glutaraldehyde (Agar Scientific Ltd, Essex, UK) added to 95 ml of 0.1 M above phosphate buffer.
3. Add 50 ml of paraformaldehyde solution to 50 ml of glutaraldehyde phosphate buffer solution. Mix the solution thoroughly.
4. The final solution contains 2.5% glutaraldehyde with 8% paraformaldehyde in 0.1 M phosphate buffer with pH 7.

APPENDIX C: FIXATION OF ARTICULAR CARTILAGE

Our complete investigation depends on fixed and dehydrated samples of articular cartilage for normal high vacuum SEM. To determine whether our fixed sample is getting affected with the chemicals or not, a study of morphological comparison between unfixed and fixed surface was extremely important

The significance of cryogenic mode ESEM is the native water and other compositions are not affected at this condition. It provides good magnification but not as good as high vacuum. Since, working temperature is very low, the dehydration of sample becomes insignificant because the liquid part solidifies. A set of samples have compared to determine the effect of paraformaldehyde, glutaraldehyde and ethanol on the cartilage surface. These samples used in a high vacuum SEM. Another set of samples were not chemically fixed or dehydrated. Prior to moving into the cryogenic chamber these samples were at fully hydrated conditions in Ringer's solution.

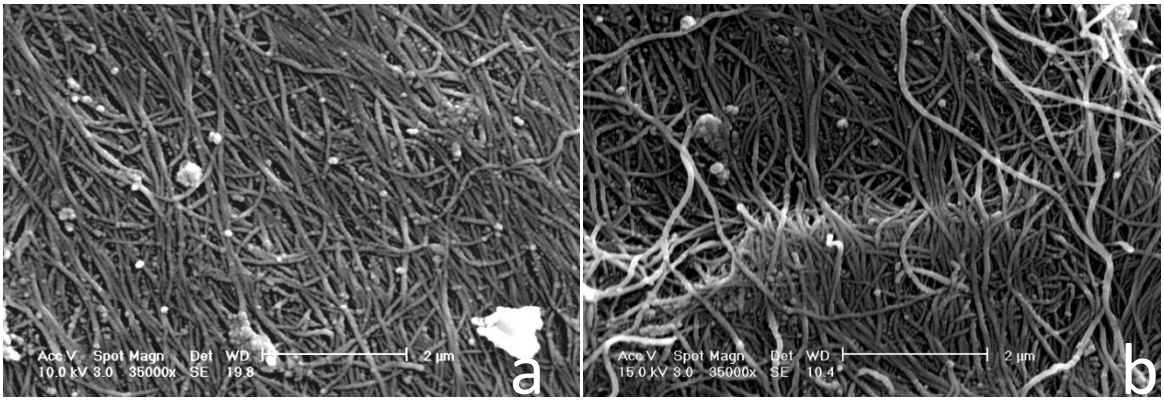

Figure C.1. (a) The surface is chemically unfixed and scanned under cryogenic temperature and (b) is chemically fixed surface, scanned under high vacuum and room temperature. It is observed that the chemical fixation process is not affecting the surface morphologically.

The surface morphology of the cartilage surface is not majorly affected with the chemical fixation protocol as we can see in figure C.1. There are two images; figure C.1.a and C.1.b are cryo-ESEM surface and SEM surface respectively. The collagen fibers have not shrunk or swollen up. The total surface morphology is fixed properly without changing the surface characteristics

APPENDIX D: PROBLEM OF CRYO-ESEM

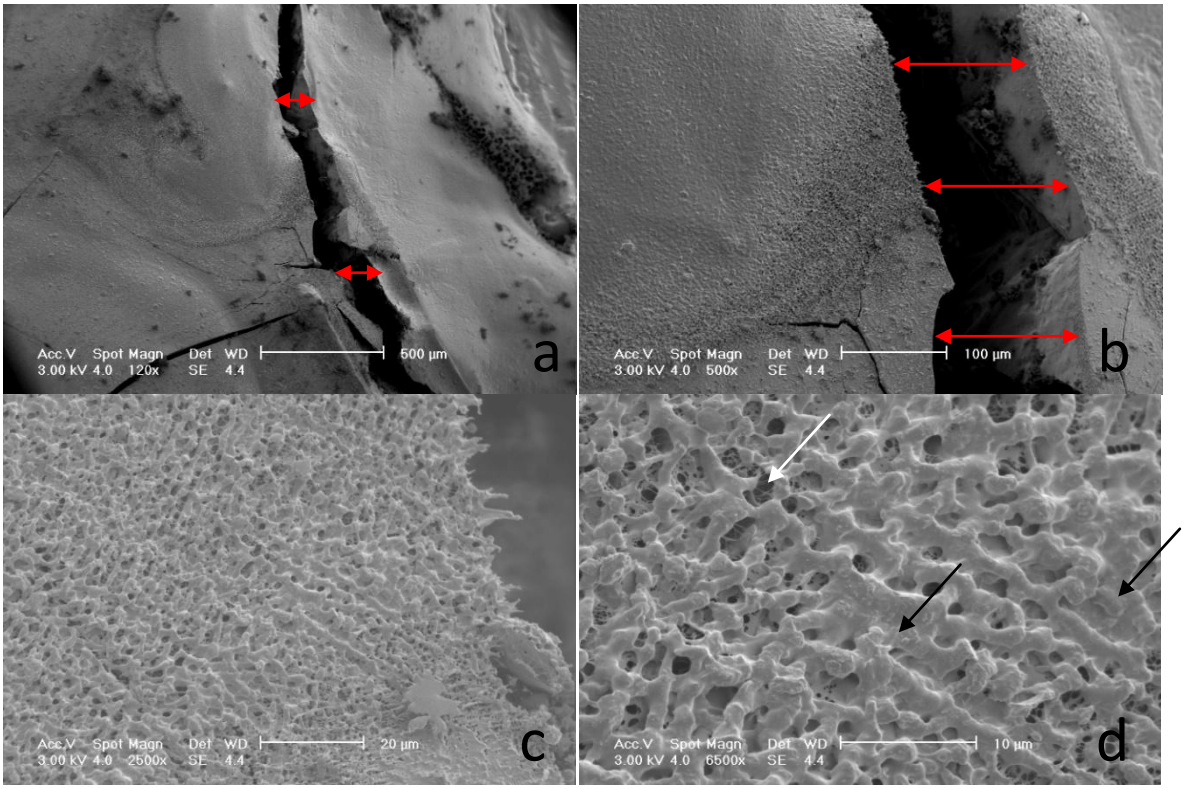

Figure D.1. Shows the major problems of cryo-ESEM. (a) and (b) shows, sudden temperature drop creates microscale fracture on the surface of cartilage. The fractures are around 1 – 120 µm thick. (c) and (d) shows the ice crystal formation on the surface, due to excess water availability and insufficient sublimation effects in the sputter chamber. In 30.D, the black arrow shows the ice blanket and white arrow shows the native cartilage surface region.

The major problem of cryogenic ESEM analysis are cracking and ice-blanket formation. The working temperature of the e-beam was used here around -173^{0}C. As we can see in figure D.1.a and b, that the surface is fractured with a range of 1 to 100 µm. These fractures on the surface are inescapable since the gradient of temperature drop down is extremely high within a short lapse. Although, we can overcome the ice-blanket problem, the micro-fractures represent a problem for measuring surface roughness. A thin ice blanket on the surface was formed due to excess water presence of the immersed solution (figure D.1.c-d). This problem can be avoided by subliming the ice inside the sputter chamber before entering into the working chamber and also ramping up the substrate temperature for a shorter time.

APPENDIX E: SPUTTERING PRINCIPLE

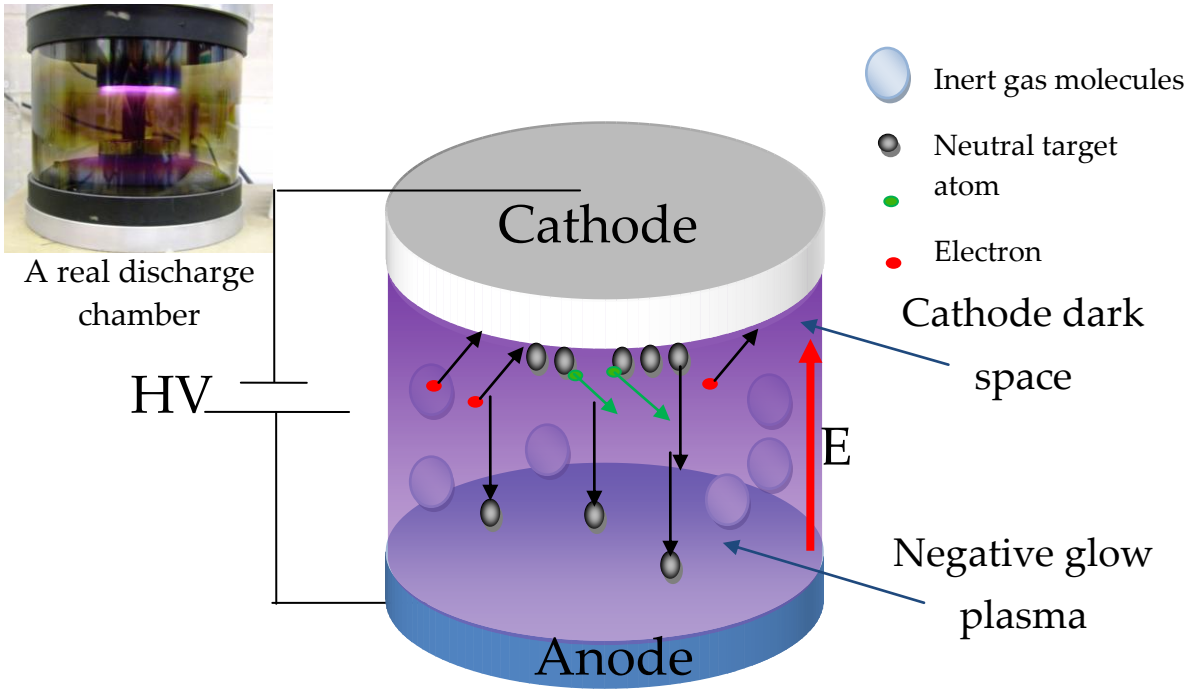

Figure E.1. Graphical representation of sputtering principle [the figure is not to scale].

Instrument category: Plasma glow discharge

Application: Thin film coating for micro-/nanofabrication and electron imaging

Detail working principle:

It is a physical vapor deposition process. Here the target is the source of depositing material which is placed as the cathode. Substrate or onto which the material will be deposited is always considered as the anode. Atoms get ejected from the cathode or the target always hold a wide energy distribution. A vacuum chamber filled with Argon is the prerequisite of sputter deposition. Applying high potential between cathode and anode leads to plasma state of argon. The ionized molecules of argon impact with high energy onto cathode and ultimately lead to etching of target by removing each single atom. The target atom get attracted towards to substrate due to charge distribution and leading to thin film deposition on substrate.

APPENDIX F: ISSUES AND ROUGHNESS ANALYSIS WITH MEX

As I have mentioned in the chapter II (background) regarding the noise problem of stereoscopic reconstruction, the images presented in figure F.1 holds some of the noises which should be avoided.

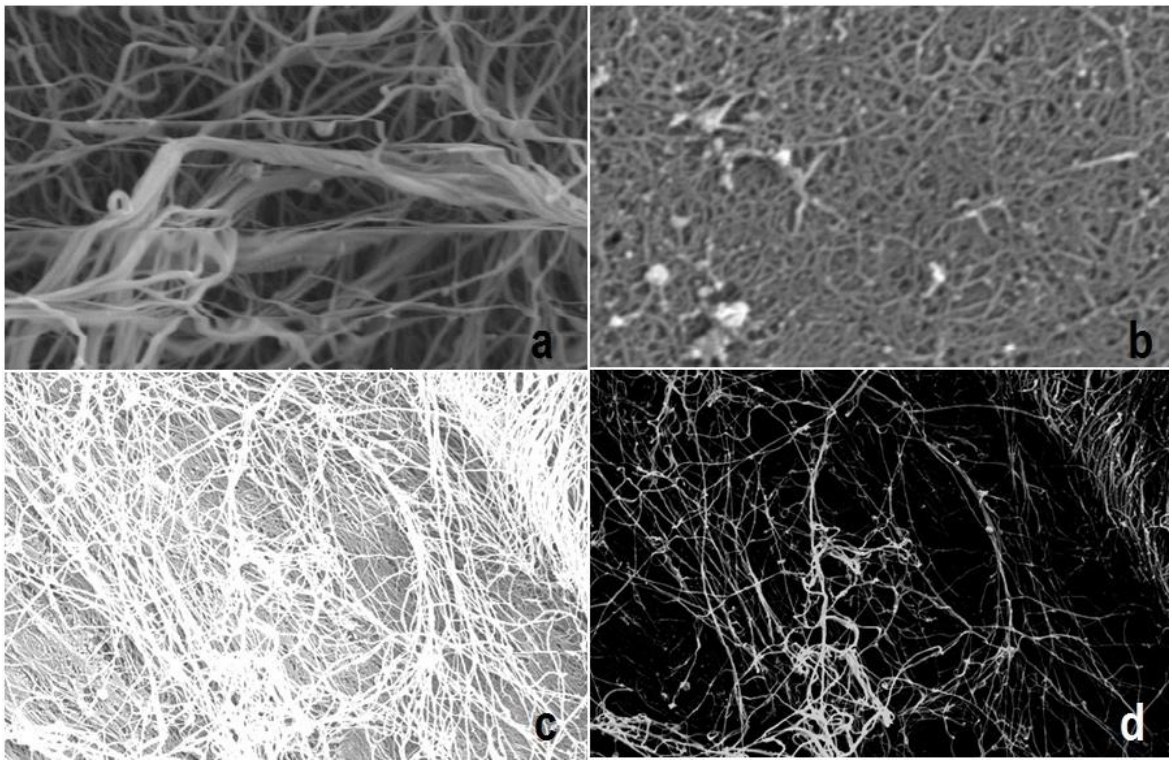

Figure F.1. (a) shows a distortion due to surface charging and slow scanning. (b) Sharpness of the image is very low due to improper focusing. In the images (c) and (d) brightness and contrast variation is not properly distributed, this kind of image is hard to reconstruct because the algorithm will be considering a same surface as two different surfaces at the step of correspondence problem.

If we have any SEM images with distortion (figure F.1.a), and the surface is charging, then the we need to reduce the accelerating voltage of the e-beam and simultaneously increase the scanning rate. These solve the distortion problem. The focusing problem (figure F.1.b) is very frequent in any SEM imaging. If a eucentric point is fixed but still at a certain angular rotation, focusing is not clear, then stigmatism and focusing at high magnification should be checked. The brightness and contrast automatically changes when we give an angular displacement. If we

see a large difference of intensities (figure F.1.c-d), then it is hard to reconstruct. This kind of variation generally occurs at high angular displacements of over 30°. Brightness and contrast should be distributed in such a way that the images can be considered as captured from a same region.

Process flow of roughness analysis with MeX after 3D reconstruction is as following [MeX, 2008]:

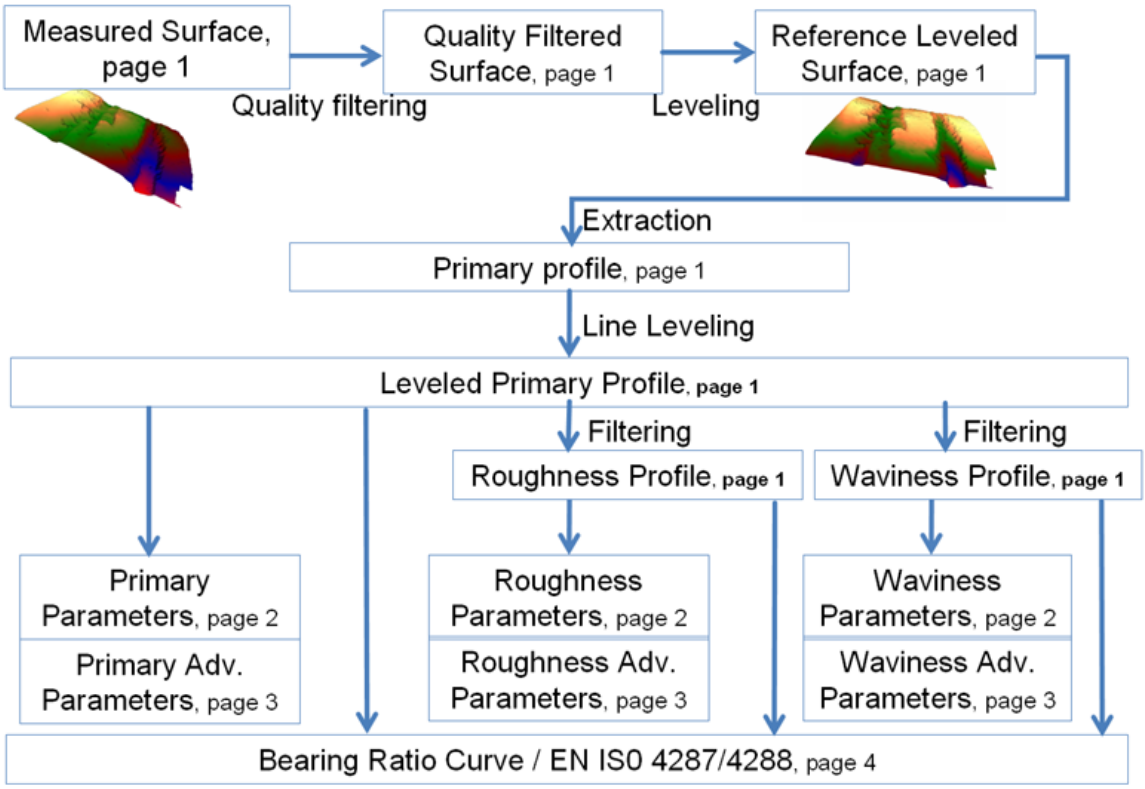

Figure F.2. Roughness analysis with MeX 5.1. [The image has taken from Mex 5.1 2008 software manual, this license was purchased by University of Birmingham]

APPENDIX G: EXAMPLES OF 3D RECONSTRUCTION

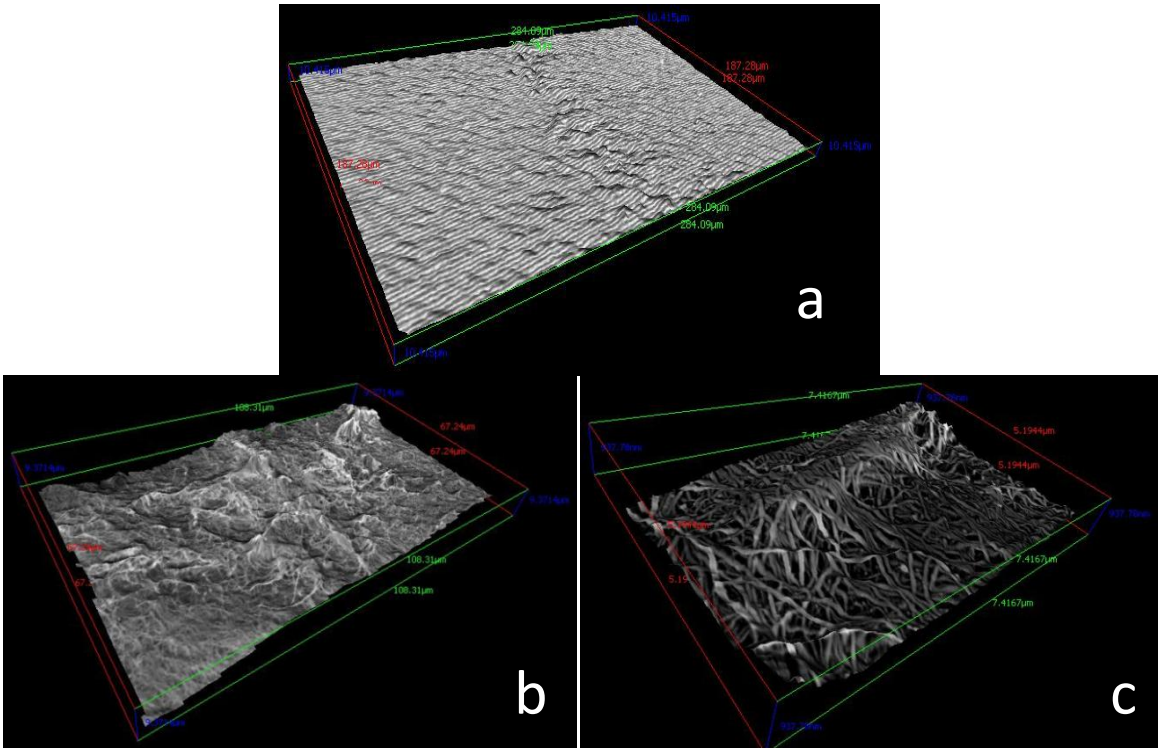

Figure G.1. (a) 3D electron-topography of PDMS surface at low magnification and superficial layer of articular cartilage; (b) where collagen fibers are loosely packed and (c) where collagen fibers are compact.

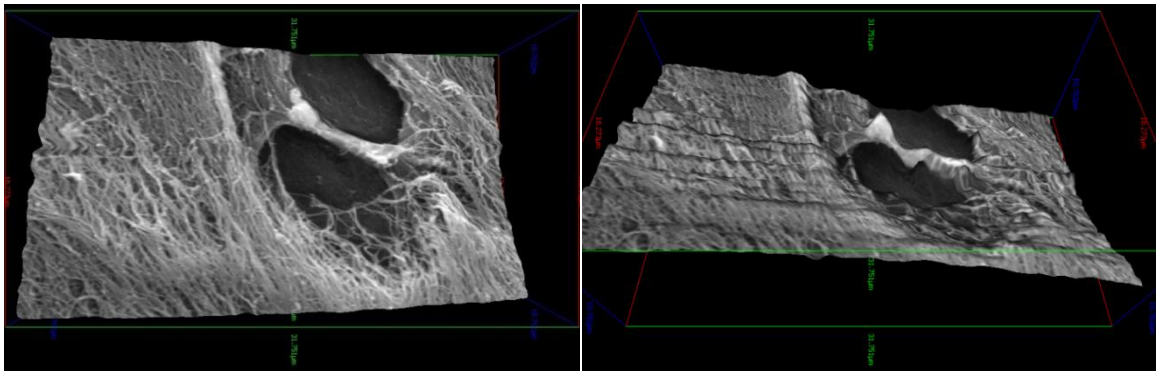

Figure G.2. 3-D topography of the holes found on the surface shows two angular views of the same holes.

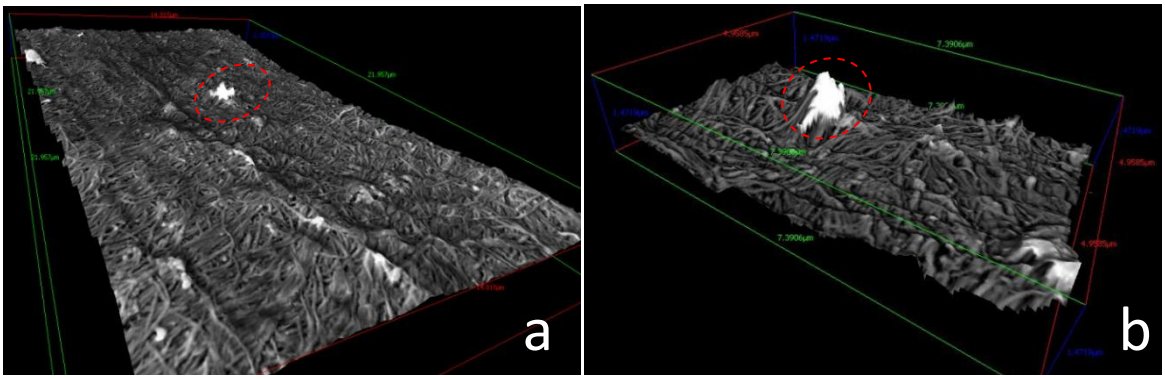

Figure G.3. A lower (a) and higher (b) magnification images of a close packed cartilage surface with a debris. The red encircled doted region is the target debris, which ultimately leads a dominant increment in surface roughness.

APPENDIX H: NORMAL DISTRIBUTION OF SAMPLE POPULATION

Two datasets are analysed for normality testing or Quantile-Quantlite (Q-Q) distribution analysis. [The quantile-quantile (q-q) analysis is a normality testing where quantile's of two datasets are analysed together to determine whether they have come from same population with a common distribution or not. It is an assessment to find the data sets normal distribution.]

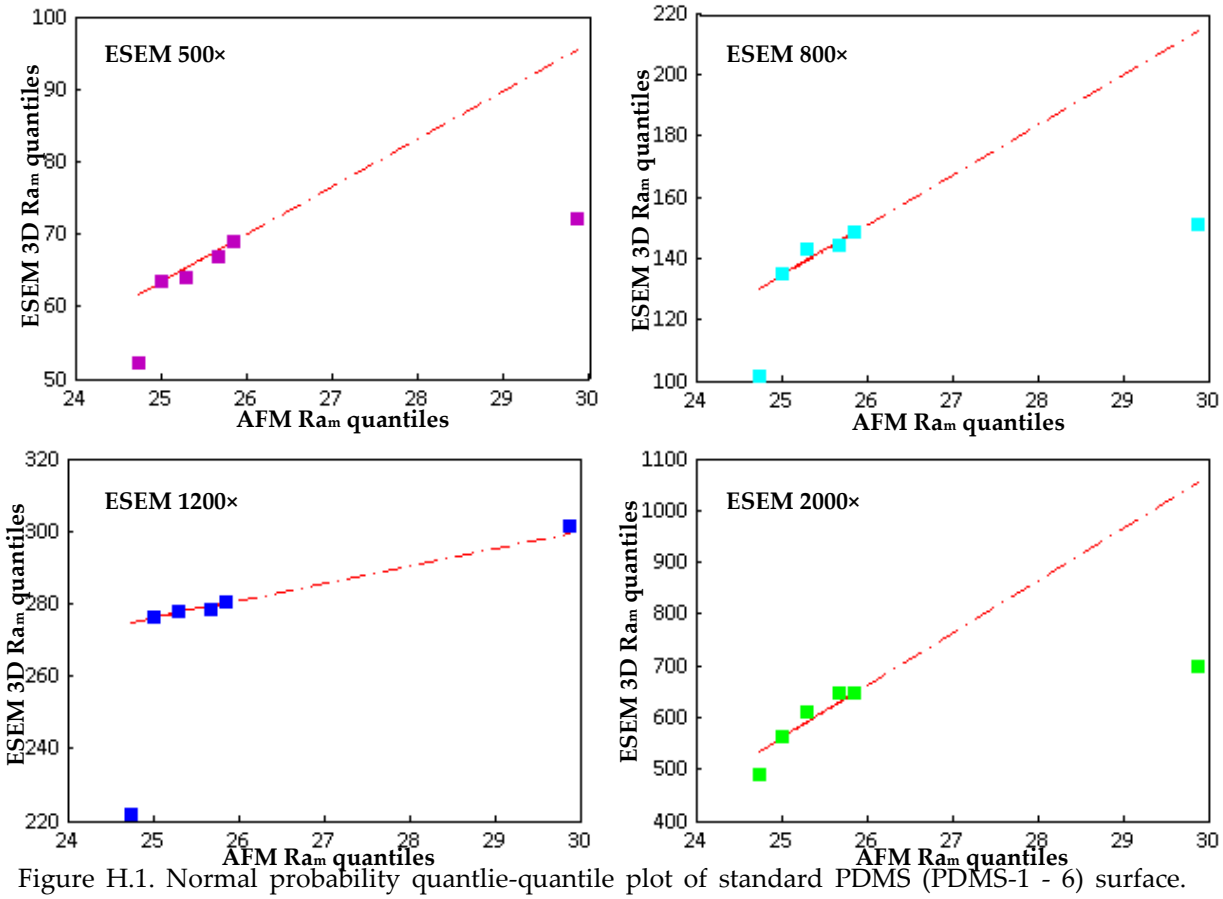

Figure H.1. Normal probability quantlie-quantile plot of standard PDMS (PDMS-1 - 6) surface. Quantiles of mean profile roughness of six samples (N = 6) obtained from electron microscopy topography and atomic force microscopy have plotted together, with respect to their magnification factor. Observed that most of the data are well fitted to their normal quantile functions.

In case of PDMS the datasets are always close to normal. In figure H.1, from 500× to 2000× all of them are close-to-normal distribution, which should be the case for any sample since they are from a same sample. Even at 2000× most of the quantile data points are fitted with normal function. So, it clearly infers the

method used is providing always normally distributed and statistically significant values.

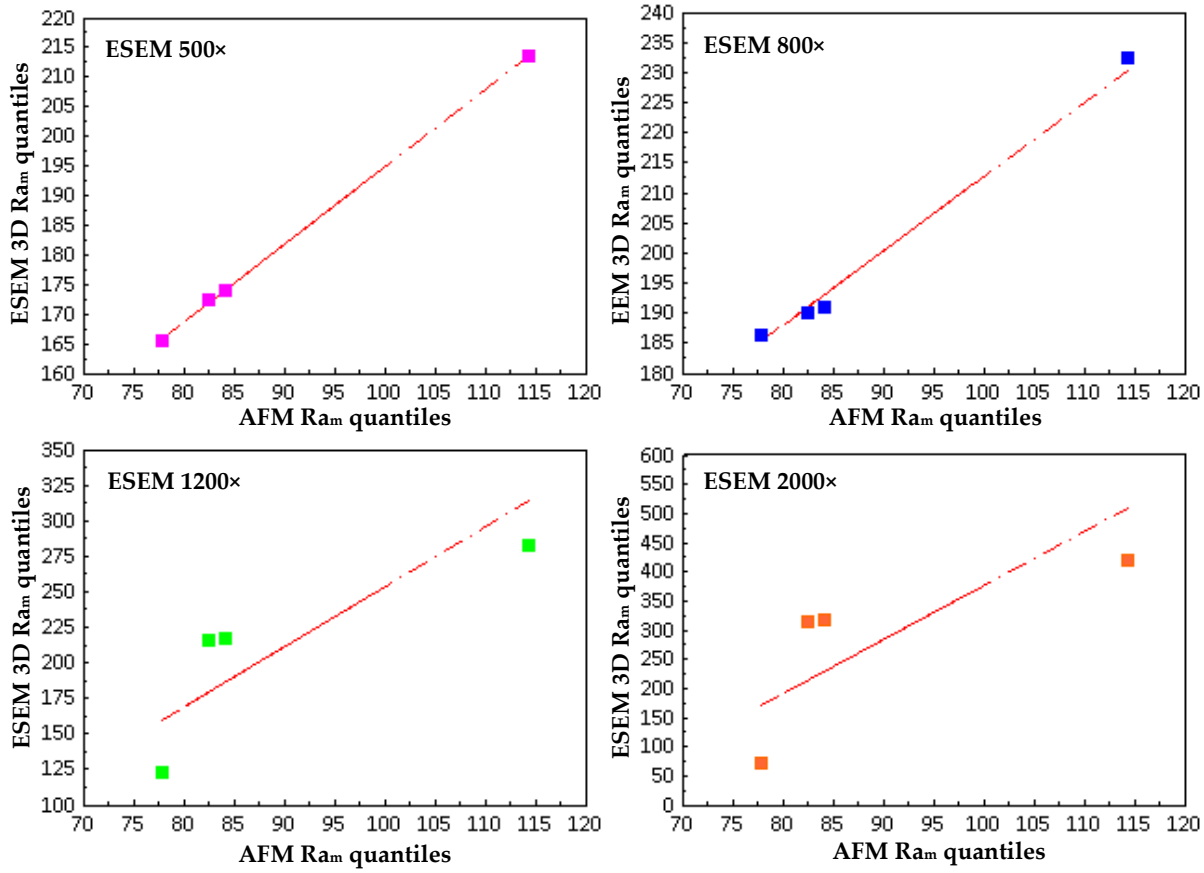

Figure H.2. Q-Q plot of articular cartilage (BHLC-1 - 4). Quantiles of mean profile roughness of four samples (N = 4) obtained from electron microscopy topography and atomic force microscopy has plotted together, with respect to their magnification factor. Observed that 500× and 800× is well fitted to the normal quantile function.

Figure H.2, contains Q-Q plots of two quantile datasets of profile roughness obtained from AFM and 3D electron-topography of bovine articular cartilage. Since the datasets are coming from same source, it is expected they are close-to-normal distribution. Here, datasets of 500× and 800 × of magnifications are very close-to-normal distribution, but in case of 1200× and 2000× it is not, the reason is BHLC-1. As we have seen earlier in the 3D electron-topography that the roughness variation of BHLC-1 was not following the trend of others. A measurement or experimental error has dominated this sample.